NAZARBAYEV UNIVERSITY

DOCTORAL THESIS

Innovative Design and Analysis of Performance Enhanced WPT/SWIPT Systems for Low-Power Applications

Author:
Kassen DAUTOV

Supervisor:
Dr. Mohammad HASHMI

A thesis submitted in fulfillment of the requirements for the degree of Doctor of Philosophy

in the

Science, Engineering, and Technology
School of Engineering Digital Sciences

September 30, 2022

Declaration

I declare that the research contained in this thesis is the author's original work, except otherwise officially noted within the text. The Thesis has not earlier been submitted to this or any other university for a degree, and it does not incorporate any previously submitted content for a degree.

Signed: Kassen Dautov

Dated: July 2022

Abstract

The wireless power transfer (WPT) technology assists users to rid of inconvenient wires and facilitates powering and charging the devices' batteries. The WPT systems have the potential to bring a complete turnaround in a variety of applications. They have been lately employed in a number of segments such as biomedicine, consumer electronics, low-power deceives, and wireless technologies. WPT can be broadly classified as far- (radiative) and near-field (non-radiative) types. If the former is accomplished using protocols, namely, time-switching and power-splitting relaying techniques, the latter is achieved by following any of coupling-based technique (*i.e.*, capacitive or inductive). In this context, it is worth mentioning that the concept of magnetic resonant coupling also falls under the umbrella of the inductive coupling. This enables the synchronization of the resonance of the transmitter and receiver to enhance the WPT performance.

Over the last decades, there has been an increase in the employment of near-field WPT systems in a variety of evolving applications that demand miniature and robust wireless end modules (*i.e.*, resonating antennas). One such emerging application is found in biomedicine, where WPTs are critical due to their ability to charge implants without the use of inconvenient and unsafe cables. This clearly calls for the design and realization of a small-size WPT capable of coping with the low-power regime. To cater to the requirements of such applications, the exploitation of the slotted ground plane (SGP)-based WPT systems has recently piqued interest.

In general, the SGP method allows reducing the resonator area, resulting in the realization of ultra-compact WPTs. Apparently, the existing multiple challenges of SGP-type WPTs necessitate efficient trade-offs for the best achievable outcome. Furthermore, the available literature includes versatile innovative design methods that attempt to overcome some of the present issues and, subsequently, realize performance-enhanced WPTs. With this in the perspective, this work aims to fully analyze and advance the state-of-the-art SGP-type WPT systems.

The key idea behind the SGP methodology is to create slots on a ground plane to modify the current flow path. The influence of etched slots is multifaceted and, as a result, they can lead to a variety of outcomes. This leads to the premise that selecting a slot type is commonly a dilemma. However, articles often overlook the other parameters that are critical in the WPT design. Thus, systematic analysis to understand the behavior of single-loop polygonal slot-based resonators has been studied where the emphasis has been on an achievable quality factor, a slow-wave effect, and a radiation loss. Consequently, the investigation findings aided in the realization of high-performance yet robust WPT.

Advanced design developments have resulted in the invention of SGP-type multi-band WPTs that can support concurrent data and power transfer protocols. Therefore, miniature SGP-based high-performance dual- and tri-band WPTs have been developed. It is pertinent to mention that communication aspects of near-field multi-band WPTs are investigated for the first time. As a consequence, the obtained bandwidth at the frequencies dedicated to data transfer allowed to facilitate applications requiring high data rates.

Acknowledgments

First and foremost, I praise the Almighty for providing me with the ability and perseverance to pursue research.

My heartfelt gratitude goes to my supervisor - Associate Professor Mohammad Hashmi. I want to thank Professor, for exposing me to advanced research in the RF circuit and antenna design domain and for his guidance, continuous encouragement, and valuable advice during my Ph.D. studies.

Furthermore, my sincere appreciation goes to my co-supervisor - Assistant Professor Galymzhan Nauryzbayev and external supervisor - Dr. Nasimuddin who consistently gave constructive and extremely useful suggestions.

I am incredibly grateful to my parents for their care and sacrifices in educating me. Furthermore, I want to extremely thank my wife *Laura* for her support and patience, and my lovely sons *Yernur* and *Sanzhar*. In addition, I would like to thank my siblings: *Dauren*, *Lyazzat*, *Gulnaz*, and *Kamshat* for their consistent support.

In addition, I thank everyone who directly or indirectly helped me in the research completion.

Contents

List of Figures

List of Tables

List of Abbreviations

AC	Alternating Current
ADS	Advanced Design System
B	Magnetic Flux
BSF	Band-Stop Filter
BP	Band-Pass
BW	-10 dB Fractional Bandwidth
CMT	Coupled Mode Theory
CPT	Capacitive Power Transfer
CST	Computer Simulation Technology
CT	Circuit Theory
DB	Dual-Band
D-BSF	Dual-Band Stop Filter
DC	Direct Current
E	Electric Field
EC	Equivalent Circuit
EM	Electromagnetic
EMF	Electromotive Force
ES	Electrostatic
EV	Electrical Vehicle
FoM	Figure of Merit
FF	Far-Field
H	Magnetic Field
IC	Inductive Coupling
IEEE	Institute of Electrical and Electronics Engineers
IMD	Implantable Medical Device
IPT	Inductive Power Transfer
ISM	Industrial, Scientific, and Medical
LP	Low-Pass
LTE	Long-Term Evolution
MB	Multi-Band
ML	Microstrip Line
MRC	Magnetic Resonant Coupling

MS	Metasurfuce
MTM	Metamaterial
NF	Near-Field
P1	Input Port
P2	Output Port
PBG	Photonic Bandgap Structure
PTD	Power Transfer Distance
PTE	Power Transfer Efficiency
Q	Quality Factor
RB	Resource Block
RF	Radio Frequency
RFID	Radio Frequency Identifier
RL	Radiation Loss
Rx	Receiver
SAR	Specific Absorption Rate
SB	Single-Band
SGP	Slotted Ground Plane
SMA	SubMiniature Version A
SMD	Surface Mount Device
SPS	Solar-Power-Satellite
SWE	Slow-Wave Effect
SWIPT	Simultaneous Wireless Information and Power Transfer
TB	Tri-Band
Tx	Transmitter
UAV	Unmanned Aerial Vehicle
UC	Unit Cell
VNA	Vector Network Analyzer
WBAN	Wireless Body Area Network
W-BSF	Wide-Band Stop Filter
WIT	Wireless Information Transfer
WIPT	Wireless Information and Power Transfer
WPT	Wireless Power Transfer
3GPP	The 3rd Generation Partnership Project

List of Symbols

λ	Wavelength
λ_0	Guided Wavelength
M	Mutual Inductance
L	Inductance
E_{g}	Excitation Gap
k	Coupling Coefficient
I	Current
N	Number of Coil Turns
Δt	Change in Time
$\Delta\Phi$	Change in B
$\mathrm{PTE}_{\mathrm{max}}$	Maximum Achievable Efficiency
P_{out}	Power at Rx
P_{in}	Power at Tx
S	Scattering
Z_{L}	Load Impedance
Z_0	Source Impedance
S_{11}	Reflection Coefficient
S_{21}	Transmission Coefficient (Gain)
R	Resistance
C	Capacitance
ω_0	Angular Resonant Frequency
I_{S}	Source Current
$H(\omega)$	Transfer Function
I_R	Current Flowing through a Resistance
C_{e}	External Capacitor
f_0	Resonant Frequency
V	Voltage
Z_{in}	Input Impedance
f_{c}	-3 dB Cut-off Frequency
f_{e}	Electric Wall
f_{m}	Magnetic Wall

C_{st}	Open-stub Capacitance
ε_{r}	Relative Permittivity
h_{s}	Substrate Height
h_{c}	Copper Thickness
l_{st}	Open-stub Length
β	Wavenumber
θ_i	Incident Angle
θ_r	Reflected Angle
δ	Loss Tangent
$\Delta\theta$	Phase Difference
$\varepsilon_{\mathrm{eff}}$	Effective Permittivity
bw	-3 dB Fractional Bandwidth

This work is dedicated to my Parents

Aueskhan Dautov

and

Sattigul Dautova

Chapter 1

Introduction

1.1 WPT Technology

In recent years, wireless power transfer (WPT) systems has been established as an emerging technology due to their upsurge in progress and application usefulness in a broad variety of areas. Their employment can bring a paradigm shift in different aspects of human life, therefore, can be beneficial economically as well as socially. For example, WPTs are extremely valuable for charging biomedical implants where a physical connection is infeasible. Furthermore, they have the potential to reduce toxicity caused by disposing of billions of batteries utilized in consumer electronics. As a consequence, WPT was ranked among the top ten emerging technologies in 2012 and 2013 by the World Economic Forum whereas it was found as a breakthrough innovation in 2016 according to the Technology Review [1–3]. It is anticipated that the revenue of the WPT technology will increase from 1.3 billion in 2015 to 17.9 billion in 2024 [4].

1.2 Motivation

The advancements in high-frequency circuits and components focus on multiple figures of merit, including the power saving mechanism, optimal power utilization, and miniaturization. In this context, the most recent key emphasis has been on the WPT systems. This technological innovation, once mature and deployed, has the potential to bring a significant change in the way electronic circuits behave and operate. Hence, it is pertinent to note that there is a need for substantial research that aids in the advance of WPTs.

Recently the antenna miniaturization using the slotted ground plane (SGP) technique has gained prominence. It is imperative to note that this approach although very promising but lacks a systematic design procedure. In this regard, it is worthwhile to mention that there are multiple challenges in the development of such systems because of trade-offs among design specifications such as a circuit size, power transfer distance (PTD), and power transfer efficiency (PTE). Furthermore, there is no extensive and precise information available about the optimal trade-off and design. As a consequence, the principal

motivation of this work is to offer a comprehensive resource including the new analysis and innovative design approaches that help construct the performance-enhanced SGP-type WPT systems and resolve some of the existing issues in this field.

A literature survey reveals that the development of SGP-based WPT systems entails the use of a slot shape in a ground plane to optimize their performance. This leads to the premise that selecting a slot type is commonly a dilemma; however, it should be noted that the reported works often overlook the other critical parameters such as quality factor (Q), slow-wave effect (SWE), and radiation loss (RL) that are equally critical in the design of WPTs. Therefore, another motivation of this work is to first conceptualize various SGP-based WPT architectures in terms of the three above-mentioned parameters. Subsequently, to develop a mechanism for the identification of a slot shape in a ground plane that can provide superior performance in terms of these three parameters. It is anticipated that the reported comprehensive analysis and subsequent contributions of this work may give a new direction to the design techniques for the SGP-based WPT systems.

Simultaneous wireless information and power transfer (SWIPT) is emerging as a new technological idea that has a potential to play a key role in the upcoming advances in wireless communications. In turn, the WPT systems are likely to make a significant contribution to the implementation of the SWIPT technology. As a result, this necessitates the advancement of novel WPT schemes that accommodate both improved PTE and increased data rate. In this instance, it is pertinent to note that near-field (NF) WPTs are getting popular due to their wide range of applications, which include but are not limited to low-power sensors and implantable medical devices (IMDs) used in wireless body area networks (WBANs). Particularly, the SWIPT-enabled WBAN infrastructure has an ability to improve human health monitoring systems by means of concurrent power and data transfer. These systems commonly require extremely high data rates that can reach 100 Mbps with respect to a given application. Therefore, it is envisaged the realization of multi-band WPTs with increased bandwidth for data transmission will be in high demand. In addition, SWIPT for health infrastructure needs to operate reliably at the radio frequencies that comply with various standards such as WBAN and industrial, scientific, and medical (ISM) bands.

1.3 Key Contributions

A brief summary of this thesis' major contributions is given below:

- This work provides *an extensive resource on the design challenges and the latest progress in the realm of SGP-based WPT systems*. In particular, the systematic design procedure of SGP-type WPTs is presented. Furthermore, the experimental

measurement challenges and the subsequent developed WPT system validation are elaborated in detail.

- The realized single-band (SB) SGP-based WPT systems demonstrate superior performance as compared to the other earlier reported works, thereby, advancing the present state-of-the-art in this domain. Specifically, different type slots such as *plus* and *Archimedean coils* were aptly utilized to enhance the overall WPT performance. In addition, both developed WPTs were experimentally validated and, thus, *showed great potential for practical applications in a low-power regime*.

- A miniature dual-band (DB) WPT, that can support wireless information and power transfer (WIPT) protocols, working at ISM bands has been developed. Experimental PTE of 71% and 81% at the respective 433 MHz and 900 MHz frequencies exhibited remarkable performance of realized WIPT. For the first time, compact SGP-based WPT *takes into consideration the communication aspects of NF SWIPT*. In particular, the implemented multi-band (MB) WPT system *accomplishes* 3 *MHz bandwidth at the communication bands enabling the system to support various applications requiring high data rates.*

- Furthermore, the usefulness of incorporating digital metasurfaces (MSs) and SWIPT to enhance the operation of low-power sensors used in WBAN has been demonstrated. To be more specific, the beam control and multi-beam creation functions of developed MS, which were achieved through distinct coding sequences, were aptly utilized. As a consequence, these interesting features, which were experimentally validated, *have revealed their immense effectiveness in facilitating the operation of the WBAN infrastructure*.

- Finally, a thorough analysis of single-loop polygonal shape SGP-based resonators used in the coupling-type WPT systems has been reported. *For the first time, some new findings that relate the resonator and WPT performance metrics to the slot shape, Q, SWE, and RL are presented in a very comprehensive manner*. It has been identified that the slot shape has no impact on the performance of resonators and, hence, the developed WPT system. Instead, the performance is hugely dependent on Q of resonators regulated by the chosen slot area. These findings allow the conceptualization of systematic WPT analysis and the development of design schemes that are readily realizable, and they also enable significant improvement in PTE. The developed prototypes conforming to ISM frequency bands showed *an enhancement in PTE to the extent of* 11% *during the measurements*.

1.4 List of Publications

The key contributions and outcomes of this work resulted in the below-given publications:

Published and Accepted Papers

Journal Papers

- **K. Dautov**, M. Hashmi, N. Nasimuddin, M. A. Chaudhary, and G. Nauryzbayev, "Quantifying the Impact of Slow-Wave Factor on Closed-Loop Defect-Based WPT Systems," *IEEE Transactions on Instrumentation and Measurement*, vol. 71, Art no. 8004310, pp. 1-10, Jun. 2022.

- **K. Dautov**, M. Hashmi, G. Nauryzbayev, N. Nasimuddin, and M. A. Chaudhary, "Compact Multi-Frequency System Design for SWIPT Applications," *International Journal of RF and Microwave Computer-Aided Engineering*, vol. 31, no. 6, pp. 1-12, Jun. 2021.

- **K. Dautov**, M. Hashmi, G. Nauryzbayev, and N. Nasimuddin, "Recent Advancements in Defected Ground Structure-Based Near-Field Wireless Power Transfer Systems," *IEEE Access*, vol. 8, pp. 81298-81309, Apr. 2020.

Conference Papers

- **K. Dautov**, Z. Kudaibergenova, M. Hashmi, G. Nauryzbayev, and M. A. Chaudhary, "Analysis and Experimental Validation of Circularly Slotted Near-Field WPT Systems," *IEEE International Midwest Symposium on Circuits and Systems (MWSCAS)*, Lansing, Michigan, USA, Aug. 2021, pp. 263-266.
  Best Paper Student Contest: *Honorable Mention Award*

- **K. Dautov**, G. Nauryzbayev, M. Hashmi, and N. Nasimuddin, "Assessment of Compact Digital Metasurface with Beam Control for WBAN Applications," *European Microwave Conference (EuMC)*, London, UK, Apr. 2022, pp. 151-154.

- **K. Dautov**, G. Nauryzbayev, and M. Hashmi, "Wireless Information and Power Transfer Systems in Biomedicine: A New Perspective on High-Speed Applications," *IEEE International Symposium on Antennas and Propagation and North American Radio Science Meeting*, Denver, USA, Jul. 2022, pp. 1-2.

- **K. Dautov**, M. Hashmi, and G. Nauryzbayev, "Novel Approach Improving Quality Factor of Miniature Slotted Resonators in Near-Field WPTs," *IEEE International Symposium on Antennas and Propagation and North American Radio Science Meeting*, Denver, USA, Jul. 2022, pp. 1-2.

- **K. Dautov**, R. Gupta, and M. Hashmi, "A Performance Enhanced Dual-band Wireless Power Transfer System for Practical ISM Bands," *IEEE Asia-Pacific Microwave Conference (APMC),* Singapore, Dec. 2019, pp. 1259-1261.

- **K. Dautov**, M. Hashmi, S. Verma, and R. Gupta "Highly-efficient Compact Size DGS-based Wireless Power Transfer for Low-Power Sensor Nodes," *IEEE MTT-S International Microwave and RF Conference (IMaRC),* Mumbai, India, Dec. 2019, pp.1-4.

- **K. Dautov**, K. Abdugapbar, M. Hashmi, and G. Nauryzbayev "Robust Wide-Angle Metamaterial-based Absorber Design for Powering IoT Devices," accepted at *International Conference on Information and Communication Technology Convergence (ICTC)*, Jeju, Korea, Oct. 2022, pp. 1-3.

- Z. Kudaibergenova, A. Toibekkyzy, **K. Dautov**, M. A. Chaudhary, and M. Hashmi, "Employment of Planar Coil and DGS based Resonators for Hybrid WPT System Realization," *IEEE International Midwest Symposium on Circuits and Systems (MWSCAS)*, Fukuoka, Japan, Aug. 2022, pp. 1-4.

- Z. Kudaibergenova, **K. Dautov**, M. Hashmi, and M. A. Chaudhary, "Utilization of Meander Line Slots for Enhancing the WPT Efficiency and Transmission Range," *IEEE Asia-Pacific Microwave Conference (APMC)*, Brisbane, Australia, Nov. 2021, pp. 452-454.

- Z. Iman, **K. Dautov**, M. Hashmi, and M. A. Chaudhary, "Symmetrically Slotted Ground Defected UWB Antenna Configurations for Microwave Imaging Techniques," *IEEE Asia-Pacific Microwave Conference (APMC)*, Hong Kong, Dec. 2020, pp. 825-827.

- Z. Kudaibergenova, **K. Dautov**, G. Nauryzbayev, M. Hashmi, and M. A. Chaudhary, "Slot-Dependent Wireless Power Transfer System for MBAN Applications," *IEEE International Conference on Consumer Electronics (ICCE-Berlin)*, Berlin, Germany, Nov. 2020, pp. 1-4.

- D. Kupreyev, **K. Dautov**, and M. Hashmi, "Design and Development of Planar Coil Structures for Small-Size WPTs," *IEEE MTT-S International Wireless Symposium (IWS)*, Nanjing, China, May 2021, pp. 1-3.

- Z. Kudaibergenova, **K. Dautov**, G. Nauryzbayev, and M. Hashmi, "Realization of Simple Band-Stop Filters for Wireless Power Transfer Applications," *IEEE Asia-Pacific Conference on Antennas and Propagation (APCAP),* Xiamen, China, Aug. 2020, pp. 1-2.

- D. Kupreyev, **K. Dautov**, M. Hashmi, and S.Verma, "Design of a Compact DGS based Dual-band RF WPT System for Low-Power Applications," *IEEE Asia-Pacific Conference on Antennas and Propagation (APCAP),* Incheon, Korea, Aug. 2019, pp. 1-2.

- D. Kupreyev, **K. Dautov**, M. Hashmi, and M. A. Chaudhary, "High-Performance Planar Hexagonal Coil-Type Wireless Power Transfer System," *IEEE MTT-S Latin America Microwave Conference (LAMC)*, Cali, Colombia, May 2021, pp. 1-3.

- M. Makin, **K. Dautov**, M. Hashmi, and G. Nauryzbayev "Outage Analysis and Realization Challenges of RIS-enabled Underlay CR Networks over Nakagami Fading," accepted at *International Conference on Information and Communication Technology Convergence (ICTC)*, Jeju, Korea, Oct. 2022, pp. 1-7.

- D. Yedres, **K. Dautov**, G. Nauryzbayev, and M. Hashmi, "Ka-Band High-Gain Reflect-Array Metasurface Antenna Design for 1-U CubeSats," accepted at *IEEE Asia-Pacific Microwave Conference (APMC)*, Yokohama, Japan, Nov. 2022, pp. 1-3.

Submitted Papers

Journal Papers

- **K. Dautov**, G. Nauryzbayev, F. Ghannouchi, and M. Hashmi, "A Comprehensive Analysis, Design, and Experimental Evaluation of Single-Loop Polygonal Slotted RF Resonators and WPT Systems," submitted to *IEEE Transactions on Microwave Theory and Techniques*, Dec. 2021.

Conference Papers

- K. Abdugapbar, **K. Dautov**, M. Hashmi, and G. Nauryzbayev, "Design of Performance Enhanced Metamaterial-enabled Absorber for Low-Power IoT Networks," submitted to *EAI International Conference on IoT as a Service*, Manchester, Great Britain, Nov. 2022, pp. 1-10.

- K. Shalpeneyeva, **K. Dautov**, M. Hashmi, and G. Nauryzbayev, "Effective Exploitation of Ambient EM Energy for Driving Emerging IoT Devices: Case Study," submitted to *EAI International Conference on IoT as a Service*, Manchester, Great Britain, Nov. 2022, pp. 1-10.

- A. Aidakhmetov, **K. Dautov**, M. A. Chaudhary, and M. Hashmi, "Development of High Performance Dual-Band Millimeter Wave Elliptic Patch-Based Antenna," submitted to *IEEE Microwave, Antennas, and Propagation (MAPCON)*, Bangalore, India, Dec. 2022, pp. 1-3.

1.5 Thesis Organization

This thesis is divided into seven major sections which are organized as follows:

Chapter 2 presents a thorough overview of the recently published articles in the domain of SGP-based WPT systems. Initially, it touches on the historical evolution of overall WPTs by pointing out some pivotal decades which are associated with noticeable progress. Then, it goes over the current state of SGP-type NF WPTs, including their features and major challenges. Finally, the existing constraints related to the SGP-based WPT systems are discussed in this chapter.

Chapter 3 covers the fundamentals associated with the overall NF WPT systems. It includes the basics of resonating circuits and discusses the main concept of the SGP technique. In particular, the utility of SGP in the development of various filtering schemes is highlighted. Furthermore, it briefly discusses the main types of coupling-based WPT systems. The principles of scattering (S) parameter-based two-port networks and the WPT performance evaluations are also presented.

Chapter 4 includes the development of SB WPT systems that can be used either for wireless power or data transfer. Particularly, the successful realization of two different SB WPTs based on the plus- and Archimedean coil-shaped slots is demonstrated. Moreover, the modeling, simulation, and experimental validation of both designed WPTs are provided. It should be noted that two different impedance matching techniques were employed for each SB WPT design. In addition, the flowchart elaborating the systematic methodology of the SGP-based WPT design is provided in this section.

Chapter 5 presents the development of MB WPT systems that can support the SWIPT regime. It is worth mentioning that this chapter consists of three main parts. Two sections discuss the realized compact-size DB and tri-band (TB) WPT whereas the third one describes the digital MS-integrated practical WBAN application scenario. Furthermore, the developed equivalent circuits for the DB and TB WPT systems are given. Finally, the experimental validations for the carried-out electromagnetic (EM) simulation of WPTs and the MS antenna are provided.

Chapter 6 discusses the performance evaluation of SGP-based WPTs in terms of three main resonator parameters such as Q, RL, and SWE. Besides, systematic analysis to understand the behavior of single-loop polygonal slot-based resonators is reported in this section. It is important to note that all provided analyses are verified by their respective experimental results. Following that, the effective use of the analyzed resonators for the high-performance WPT system development is presented.

Chapter 7 concludes this work and discusses the future research directions that have the potential to advance the existing NF WPT systems.

Chapter 2

Literature Review

This chapter introduces the most recent state-of-the-art in the field of NF SGP-type WPT systems. Particularly, the provided overview includes the early WPT establishment history and its advancements over the years. In addition, the emerging WPT applications, WPT main types, and an appropriate comparison of coil- and SGP-based WPTs are provided in this section. Finally, the latest research findings on SGP-based WPTs along with their potential limitations are also discussed.

2.1 WPT Systems

Recent decades have seen that various electric equipment facilitate human life and, therefore, their role is becoming increasingly important. So far, the powering has been accomplished through the use of cables or metal conductors in any form. It is critical to note, in this regard, that this type (*i.e.*, power transfer via wires) of powering can be unsafe and inconvenient for some applications. For example, the utilized cables are prone to corrosion and wear that eventually can reduce the equipment's life span. Nowadays, it is apparent that numerous advanced consumer electronics are becoming more integrated into human life. In essence, they all work on batteries with limited capacity and naturally require constant charging through cables. On the other hand, it should be also noted that the number of IMDs is constantly increasing all over the world. The embedded batteries of IMDs must be replaced on a regular basis, which may necessitate unpleasant surgeries for patients.

In general, the traditional methods of powering via cables can be hazardous, economically inefficient, or even impossible depending on the application scenario. All these mentioned issues essentially point to the need for a new innovative technology that can aid in the discard of conventional wires. One such innovation that can provide a solution to overcome the aforementioned constraints is the *wireless power transfer* technology. The key concept of WPT is very simple and lies in transferring the electrical energy by means of EM waves, *i.e*, without using physical conductors. As a result, most of the

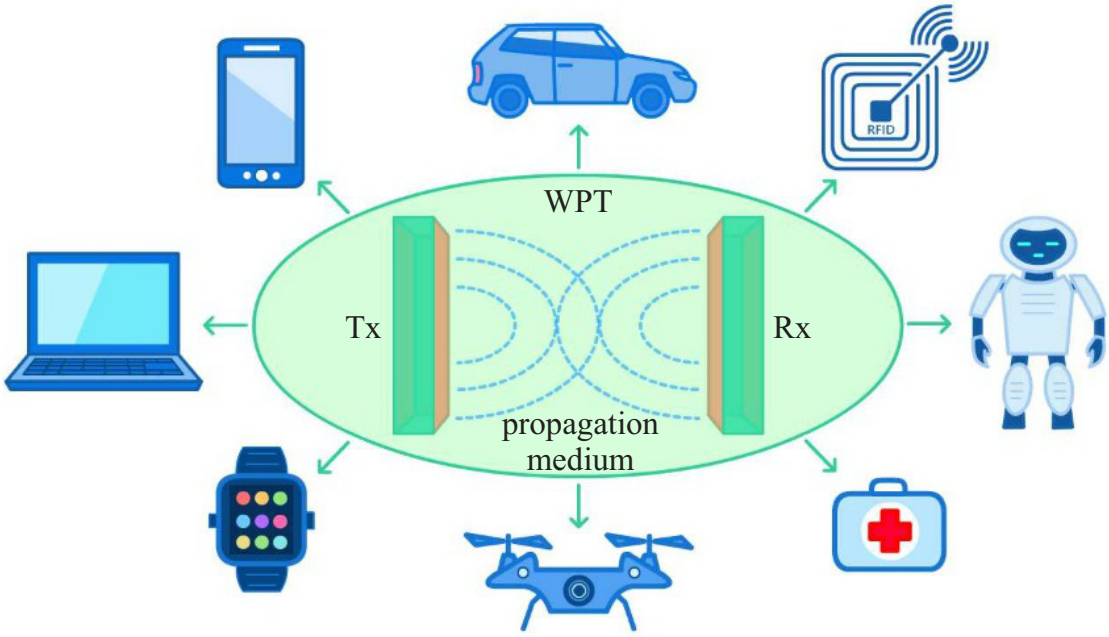

Figure 2.1. The WPT technology application areas.

problems associated with traditional powering can be resolved. The general WPT principle is divided into three stages: i) at the transmitting node, direct current (DC) electrical power is converted into the radio frequency (RF) one; ii) then, the RF power will propagate through a space; iii) finally, at the receiving node, the sent power is collected and converted back into DC.

In a broad sense, WPTs can be classified into two types: far-field (radiative) WPT and near-field (non-radiative) WPT [5, 6]. Depending on the nature of WPTs, the potential application of the WPT system tends to vary, some of which are depicted in Fig. 2.1. For instance, far-field (FF) WPTs are mainly employed in long-distance and vehicular communications, including unmanned aerial vehicles (UAVs), electrical vehicles (EVs) [7], and satellite communications [8–10]. The NF WPT systems, on the other hand, find usefulness in broad application areas such as radio-frequency identifiers (RFIDs) [11], microrobots [12], various consumer electronics [13], low-power sensor nodes [14, 15], and biomedical implants utilized in WBAN [16–18]. In this context, it is worth noting that, due to the versatile application, some WPT standards have been developed that regulate issues related to this field. One such standard is known as Qi from Wireless Power Consortium [19]. According to this standard, the low-, medium-, and high-power applications require the maximum power of about 5 W, 120 W, and 1 kW, respectively.

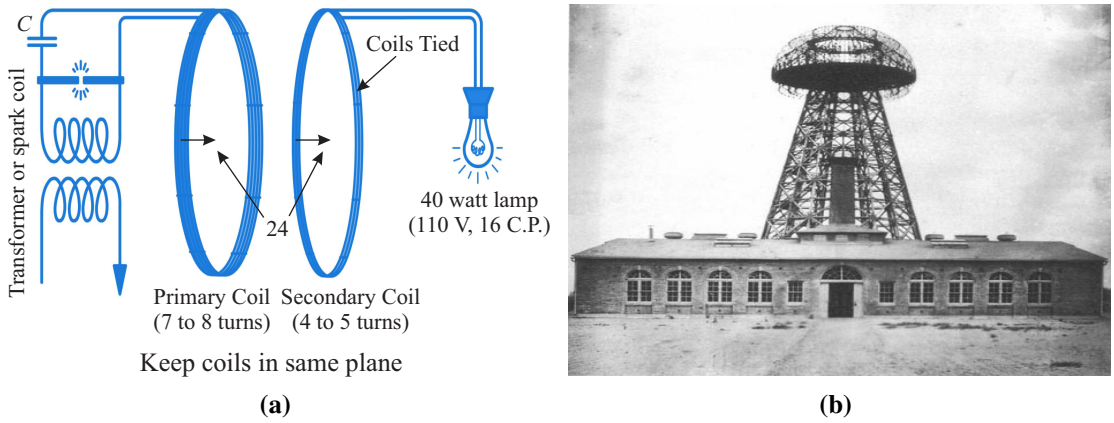

Figure 2.2. Nikola Tesla's experiments in the late 19th-century: (a) circuit diagram; (b) Wardenclyffe Tower.

2.1.1 WPT Evolution

The idea of WPT dates back to 1888 when Heinrich Hertz conducted his first experiments showing the prospect of the EM wave propagation through an atmosphere [20, 21]; however, Nikola Tesla is regarded as the father of the WPT technology since he was the first to document his original work on WPT in the late nineteenth-century [22, 23]. Some of the key moments in the history of the WPT evolution are briefly discussed below:

- 1893 – 1901: This period encompasses Nikola Tesla's initial experiments [22]. He demonstrated his idea of wirelessly powering light bulbs using coupled resonant coils [24]. Besides, during this time span, the famous Wardenclyffe Tower was constructed near Long Island for wireless power transmission and broadcasting purposes (Fig. 2.2) [5, 25]. It is imperative to note that, while the feasibility of the general wireless energy transmission concept was proven, the overall experiment failed mainly because of a lack of advanced technology at the time.

- 1930's: Harrell Vaun Noble successfully transferred about 100 W power at 100 MHz when two identical resonating dipoles were separated by 8 m (25 ft) [21].

- 1968: Peter Glaser pioneered the solar-power-satellite (SPS) concept, which revolved around the relationship between SPS and microwave power transfer [26].

- 1990's: This epoch can be regarded as the modern evolution era of the WPT technology. The Auckland University research group thoroughly investigated the concept of the EM induction, also known as inductive power transfer (IPT) [27, 28].

- 2007: The early concept introduced by Tesla was reinvigorated by scientists at the Massachusetts Institute of Technology [29]. The 60 W bulb was lightened by powering wirelessly from 2 m. During the experiments, the strong resonant coupling

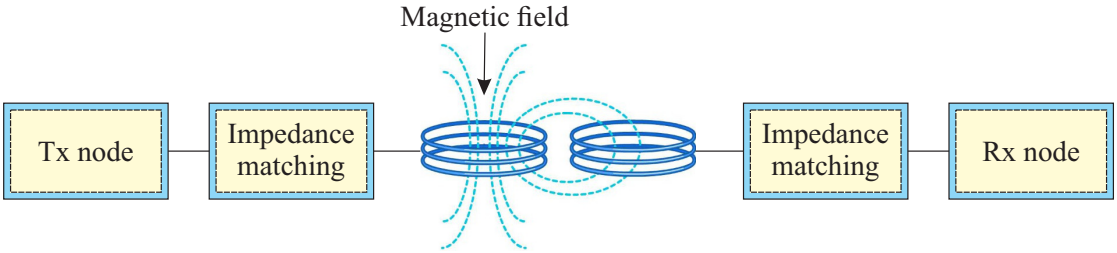

Figure 2.3. The diagram of inductively coupling-based NF WPTs.

technique was implemented using two coils that possess stray capacitance. Moreover, the measurements showed that 40% PTE was obtained at the 10 MHz resonant frequency. As a consequence, these experiments triggered both academia and industry to investigate more extensively which resulted in the general WPT technology advancement and the broadening of its application areas.

2.1.2 Near-Field WPT Systems

In general, the EM radiated WPT systems can be broadly categorized into NF and FF WPTs according to PTD. In essence, the former corresponds to a distance much smaller than the wavelength (λ) whereas the latter conforms to a distance greater than λ. Furthermore, FF WPTs use transmitting equipment that is physically much smaller in contrast to PTD. It should be also noted that, due to the radiative nature, the FF WPT systems can be hazardous to human beings and, subsequently, their applications are limited.

The NF WPT systems, as the name implies, require a smaller power transfer range and are developed using EM induction. The overall diagram of the coupling-based NF WPTs is shown in Fig. 2.3 whose operating principle is as follows. The DC to AC (alternating current) conversion occurs first on the transmitter (Tx) side. This can be obtained using either full-bridge inverters or Class E amplifiers [30–32]. Then, the impedance matching is performed to minimize losses. In turn, this step is carried out using a variety of available matching techniques [33, 34]. Following that, the electrical energy can be received by the coupled receiver (Rx), which performs the opposite operations. In particular, the received AC power is converted back into the DC power on the Rx side by employing rectifiers. As a consequence, the rectified DC power can be utilized for its original purpose, *i.e.*, to charge a connected load.

Three distinct coupling-based methods, such as capacitive [35], inductive [36], and magnetic resonance [29], have been extensively investigated in the context of NF WPTs. The capacitive technique has smaller PTD than the other two methods and, thus, has less potential in practical applications [37]. The inductive and resonant coupling-type WPT systems, on the other hand, are developed using various coil structures and have considerably longer PTD [38]. Recently, these methods have been progressing rapidly due to the

Table 2.1. The SGP- and coil-based NF WPT comparison.

Parameters	SGP	Coils (incl. planar ones)
Operating frequency [13, 40, 43]	high ($>$ 100 MHz)	low ($<$ 100 MHz)
PTE [40, 43–45]	moderate ($60-75\%$)	low ($<50\%$ at low frequencies)
PTD [29, 46]	moderate	high
Implementation [13, 40, 46]	easy	complicated
Equivalent circuit [12, 47]	complicated (quasi-static)	easy
Multi-band operation [43, 45]	+	−
Frequency Splitting [48–51]	+	+
Robustness [29, 46]	+	−
High Q realization [13, 42, 52]	+	+ (for planar types)
Cost [40, 42]	−	+
Compactness [43, 46]	+	−
Ease of Design [11, 52]	+	−
Misalignment sensitivity [44, 53]	+	+

evolution of modern technologies which allow planarizing the conventional coils employing microstrip lines (MLs) [39, 40]. In fact, the key concept of the magnetic resonance coupling (MRC) technique lies in tuning Tx and Rx to the identical resonant frequency. As a consequence, focusing power on the specifically selected carrier frequency becomes feasible which, in turn, results in enhanced PTE as compared to inductive coupling-based WPTs [24, 25]. MRC necessitates the use of a resonator [41] which can be achieved using the SGP method [42]. In this context, it is important to note that MRC-based WPTs are realized following both techniques, *i.e.*, employing coils of any form and SGP. Therefore, the appropriate comparison of the two approaches in terms of main design specifications and considerations is presented in Table 2.1.

A literature review on reported coil-based NF WPTs reveals a number of novel design approaches, analysis techniques, and overall system performance improvement methods [53–58]. For instance, the misalignment between Tx and Rx coils degrades the WPT performance considerably, and a new innovative design scheme was proposed to overcome this constraint [53]. It has been identified that the coupling degree and mutual inductance (M) of designed WPT have a huge effect on the eventual system performance. High-performance WPT can be realized by using a numerical model that can anticipate M prior to the design process [55]. Furthermore, the common issue related to the mutual coupling, between the coupled resonators, was addressed by integrating switchable capacitors into the developed WPT system [54]. It is well known that overcoupling leads to the split in the operating frequency, consequently, the WPT performance degrades [48], and the analytical solution that addresses this phenomenon was presented in [56]. Moreover, it is imperative to note that Q of the utilized resonators, for WPT, can assure high performance. This was effectively shown by the substrate suspended line technology to improve Q of printed inductors and resultant WPT characteristics [59]. Moving forward, printed spiral-type WPTs were application-oriented, *e.g.*, the high-performance WPT systems for

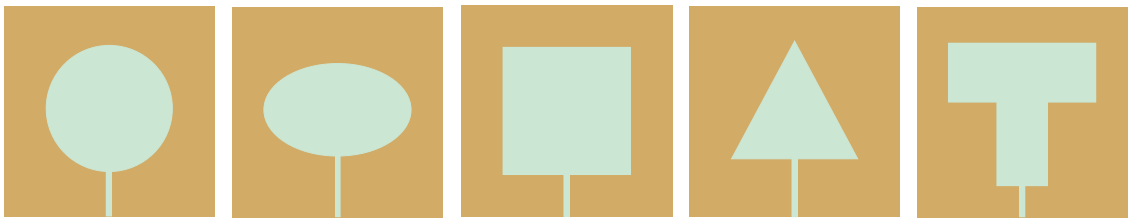

Figure 2.4. Slot geometry examples for the SGP-based WPT design.

biomedical usage by considering different practical frequencies [57, 58]. In general, a brief perusal of coil-based WPTs demonstrates their usefulness in sending power over longer ranges. These systems, however, have two obvious limitations: large circuit area and manufacturing complexity [12, 29, 46]. In addition, these constraints can be resolved by planarizing coils; however, this still does not satisfy the requirements for resonator compactness and simplicity of the design [60–62].

As mentioned above, MRC-based WPTs require two coupled resonators possessing the same resonance that serve as Tx and Rx. Essentially, the most critical parameter of any developed WPT is PTE which is primarily reliant on Q of unloaded resonators and the coupling degree between Tx and Rx [63]. For example, cubic high dielectric [64] and cavity resonators [14] have proven their usefulness in the highly efficient WPT design. Nonlinear resonators, on the other hand, are extremely effective at solving the WPT constraints caused by coupling variations [65]. Furthermore, recently, the engineered artificial structures, known as metamaterials (MTMs), with negative permeability are widely utilized to enhance the WPT performance. In particular, the use of MTMs can ensure uniformly distributed current which may result in the enlarged magnetic field (H) created around resonators, strong coupling, and PTE enhancement.

2.2 SGP-based WPT Systems

In recent years, there has been huge interest in the NF WPT systems that make use of the SGP technique. This phenomenon is associated with the inherent advantages of such an approach over other counterparts, namely, the design ease and circuit size reduction capability [66]. It is pertinent to note that the utilized slot geometry determines the resonator's key characteristics. The literature is replete with reports that discuss methodologies for resolving the WPT challenges by utilizing distinct slots such as plus, rectangle, hexagon, E, U, C, H, *etc.* In addition, some of those frequently employed slots (*i.e.*, circle, square, ellipse, triangle, T) are depicted Fig. 2.4.

Fig. 2.5 illustrates the typical structure of the SGP-based resonator. It consists of three layers, *i.e.*, a single layer of a dielectric material, and two layers of copper. The slots are

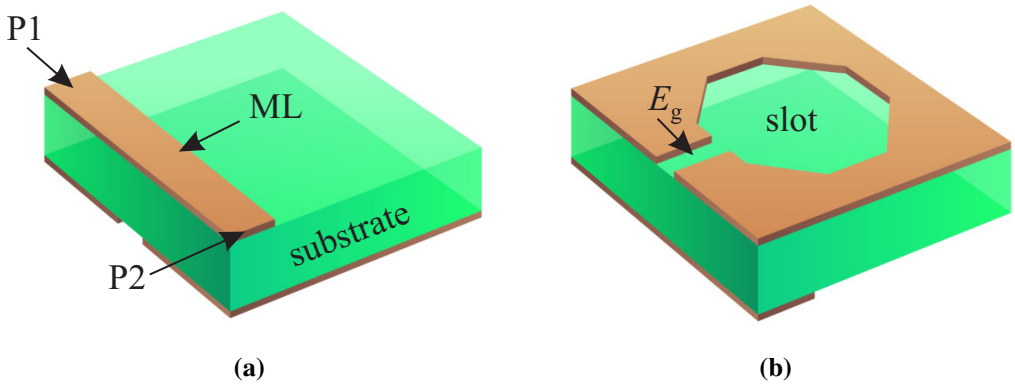

Figure 2.5. The SGP-based resonator structure: (a) top; (b) bottom.

introduced on the bottom side (ground plane) while the top side stays unchanged. The excitation gap (E_g) placed below ML aids in the creation of a resonance. The input (P1) and output (P2) ports are connected to two ends of ML to evaluate its performance. It is worth noting that the analysis, design, and optimization of the SGP-type resonators can be carried out using any available EM and circuit simulation software.

The use of SGP-based resonators in the compact-size NF WPT development has increased over the last decades. In particular, the very first SGP-based WPT design revolved around H-slotted resonators [46]. Following that, different implementation techniques and analyses have been proposed and successfully realized that aim to advance this field. For example, the J-inverter method showed its extreme usefulness in the WPT analysis and extraction of its key element values [43]. Moreover, several works investigated different misalignment issues between receiving and transmitting resonators and proposed novel approaches that helped mitigate some of them [44, 46]. Besides, SGP-type WPTs have further advanced to the MB systems that enable power and information transfer wirelessly [45]. It is pertinent to mention that the well-accepted metric known as the figure-of-merit (FoM), which includes all critical WPT parameters, is employed to benchmark both single- and multi-band WPTs. In addition, Table 2.2 provides an appropriate comparison of the WPT performance that was designed using distinct ground slots.

2.2.1 Power Transfer Efficiency

PTE is one of the key parameters of the WPT systems that is strongly influenced by the inductance (L) of the resonator, with greater L leading to increased efficiency. As a consequence, this occurrence was investigated using various geometrical slots, namely, two-turn square, semi-H, and H [42, 46]. These studies revealed that due to the single current path, the semi-H slot shows higher inductance as compared to the H slot and,

Table 2.2. The comparison of different SGP-based WPTs (*single-, $^{\circ}$dual-, $^{\bullet}$tri-band).

Ref.	Freq. (MHz)	PTE (%)	PTD (mm)	Size (mm×mm)	FoM
[42]*	50	68.5	50	40×40	0.856
[46]*	300	73	25	21×21	0.86
[50]*	435	64.6	44	35.8×20	1.06
[52]*	270	71	11	20×20	0.39
[67]*	150	65	22	25×25	0.572
[68]*	2400	67	10	20×20	0.335
[69]*	300	81	25	30×30	0.675
[70]*	49	62	10	20×20	0.39
[71]*	300	80	17	20×20	0.68
[43]$^{\circ}$	300/700	71/72	16	30×15	0.757/0.772
[49]$^{\circ}$	2400/5800	60/67	3.5	15×10	0.17/0.19
[51]$^{\circ}$	300/675	80/73	17	20×20	0.68/0.62
[72]$^{\circ}$	433/900	60/63	18	20×20	0.54/0.567
[73]$^{\circ}$	405/925	58/74	17.5	34×20	0.55/0.69
[74]$^{\circ}$	90.3/138.8	70/69	40	50×50	0.56/0.55
[75]$^{\circ}$	381/750	60.3/54.3	10	18×18	0.237/0.214
[76]$^{\circ}$	440/918	40.9/49.2	15	11.7×10.2	0.562/0.676
[45]$^{\bullet}$	100.8/140.7/182.2	68/60/65	30	50×50	0.4/0.36/0.39

hence, developed WPT using the former-type resonators demonstrates greater PTE. Furthermore, it was also discovered that the two-turn square slot provides greater L owing to the longer current path, subsequently, improving the system efficiency. On the other hand, it was reported that Q of used resonators also impacts PTE which was shown by analyzing and using dual-E shape slots for the WPT realization. It should be also noted that the propagation medium between two nodes has a significant impact on achievable PTE and, therefore, should be considered during the WPT design. Furthermore, PTE is severely impacted by the misalignment between Tx and Rx, which was analyzed utilizing the semi-elliptic ground slot [44]. Another approach for the PTE improvement can be obtained by developing MB SGP-based WPT systems, which was demonstrated through the use of cascaded circular slots [43].

2.2.2 Power Transfer Distance

PTD is regarded as another extremely vital aspect of coupled WPTs, thus, numerous studies on different SGP-type resonators have been conducted to improve it. It is worthwhile to mention that the coupling coefficient (k) is directly proportional to PTD, *i.e.*, greater k corresponds to increased PTD, and conversely [50]. It has been also revealed that high Q can be achieved using rectangular-shaped SGP-based resonators. Furthermore, some of recently reported WPTs attempted to enhance PTD by examining the plus and hexagonal slot-based resonators [73]. In addition, the meander line slot was thoroughly analyzed to generate larger `H` which resulted in the PTD enlargement [69].

2.2.3 Miniaturization

It is imperative to note that one of the most important aspects of the realization of SGP-based WPTs for low-power biomedical applications is the resonator area miniaturization. There have been some efforts to resolve this necessity. In particular, the overall WPT system volume can be reduced by coupling two different-sized resonators, *i.e.*, the transmitting resonator is bigger than the receiving one; however, in such a system model it should be ensured that both resonators are oscillating at the same frequency. Another report which focuses on the resonator miniaturization aptly utilized the U-shaped slot to develop the DB WPT system that operates at practical ISM bands [49]. Furthermore, several compact dual- and multi-band WPTs, whose main purpose is wireless information and power transfer, have also been developed using the SGP technique [45, 74]. Besides that, it has been demonstrated that the size reduction of DB WPT can be accomplished by incorporating a lumped capacitor [51].

2.2.4 Multi-band WPTs

Recent progress in the design of MB WPTs has shown their huge potential for practical WBAN and real-life applications. Specifically, these systems assist to implement the innovative SWIPT technology which, in turn, tends to advance the state-of-the-art in the field of practical WBAN scenarios. It is important to mention that, during the SWIPT system development, the achievable bandwidth should be taken into consideration as they should provide high data rates that can fulfill the given application requirements. For example, in the biomedical field, the required data rate may reach 100 Mb/s necessitating a high achievable bandwidth [77]. Furthermore, considering the biomedical usage, the safety concerns of used Tx and Rx are of particular importance. The Institute of Electrical and Electronics Engineers (IEEE) standardizes the safety levels for human exposure from 3 kHz to 300 GHz [78]. The IEEE International Committee on Electromagnetic Safety proposed the standard, which was later approved by the IEEE-SA Standards Board. Moreover, the maximum input power should be set to 156 mW and 615 mW for the 1-g and 10-g mass averaging, respectively [79]. In addition, the specific absorption rate (SAR) should be less than 1.6 W/kg and 2 W/kg for the respective 1-g and 10-g cubic tissue [80].

2.3 SGP-based WPT Limitations

Recently published works in the domain of SGP-type WPTs describe the key challenges including PTD, PTE, resonator's size, and achievable Q. For example, the majority of the reports mainly discussed the modeling and analysis process while ignoring the common

challenges faced in the general SGP-based WPT design. Particularly, only a few developed WPTs were provided along with the respective quasi-static equivalent circuit analysis [46]; however, it is pertinent to note that several designs didn't use this approach. As a consequence, a significant difference between the circuit and EM simulations may occur which can be witnessed in some recent reports [42, 52]. This eventually paves the way for further investigations into establishing a standard framework for the equivalent circuit (EC) of the SGP-based WPT systems. Furthermore, as previously stated, the resonators with high Q can assure improved PTD and PTE; however, it should be highlighted, in this regard, that developed WPTs so far exhibited PTE of 85% as a maximum [42, 74]. This creates a new challenge for designers to pursue the design of SGP-based resonators possessing high Q. Furthermore, the potential misalignment between the coupled resonators has a significant negative impact on the WPT performance [44]. Therefore, this aspect should be fully examined and taken into consideration during the design to mitigate its effect. In addition, the overcoupling and subsequent frequency splitting phenomenon also reduces achievable PTE, as can be witnessed in several developed systems [50, 51].

Summary

It is imperative to note that the concept of general WPTs started at the end of the 19-century and went through significant progress up to date. Consequently, nowadays, WPT has been established as an emerging technology that finds usefulness in many application fields. In this regard, it is worthwhile to mention that the SGP technique has shown its ability to realize robust and high-performance NF WPTs. Finally, despite the fact that SGP-based WPTs have made significant improvements in the last decade, this area still requires novel design methods and analyses that help lift this field to a new height.

Chapter 3

Near-Field WPT Fundamentals

This section presents the fundamentals of general WPT systems and resonator concepts. In particular, the main types of NF WPTs such as inductive, capacitive, and magnetic resonant coupling WPTs are briefly discussed. This chapter also touches upon the basic working principles of the SGP technique. Furthermore, the design and relevant discussion of SGP-based different filtering structures are provided to exemplify the capabilities of this approach.

3.1 WPT Fundamentals

In general, any WPT system comprises Tx connected to a power source and Rx that receives, subsequently, distributes the power to a load. It is well accepted that the Tx coil is considered as the primary coil whereas the Rx coil is the secondary one. In the presence of applied power, the current (I) flows through the primary coil, consequently, a magnetic field is formed around it. Moving forward, when Rx is tightly linked to Tx a voltage is produced in the secondary coil allowing current to move that leads to generated $\mathtt{H}$ around the receiving coils. Therefore, the secondary coil's current can be effectively used by any load without a physical link. In addition, WPTs are established on a number of fundamental laws, which are discussed further below.

Ampere's law states that I traveling through a closed-loop conductor leads to the creation of $\mathtt{H}$ around it. It is worthwhile to note that $\mathtt{H}$ produced by I is proportional to its actual size, with a constant of proportionality equivalent to free space permeability. The generic mathematical expression of Ampere's law is given in (3.1). Furthermore, according to Faraday's law, the induced voltage (V), *i.e.*, instant electromotive force (EMF), in a circuit by changing $\mathtt{H}$ is proportional to that magnetic field's change. Its respective expression, on the other hand, is given in (3.2). Here, N represents the number of loops (coil turns), $\Delta\Phi$ is the change in magnetic flux ($\mathtt{B}$) while Δt variation in time. Furthermore, according to Lenz's law, induced EMF produces current, which introduces unique $\mathtt{H}$ that opposes the established magnetic field.

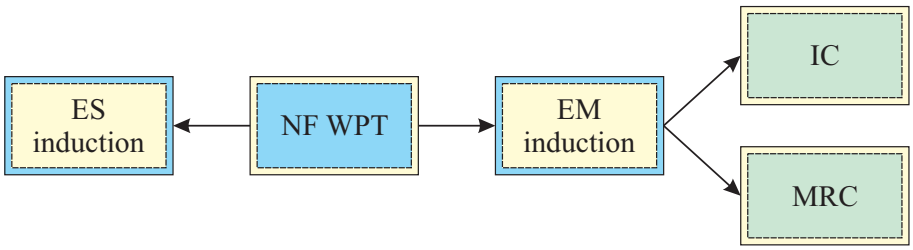

Figure 3.1. The classification of NF WPT systems.

$$I = \int \mathtt{H} \cdot dl, \tag{3.1}$$

$$V = -N\frac{\Delta\Phi}{\Delta t}. \tag{3.2}$$

The WPT systems are commonly classified differently depending on the particular utilized structures. For example, they can be divided into two- and four-coil WPTs premised on the impedance matching structure. On the other hand, the resonant-type WPTs are further categorized into the groups such as series and parallel. It is also worth noting that these structures can result in a variety of combinations, such as series-series, series-parallel, and parallel-parallel. Besides, WPTs can be described using diverse theoretical perspectives such as the coupled-mode theory (CMT) and circuit theory (CT). As the name implies, CMT is the method for characterizing and analyzing coupled resonator-based WPTs [29]. Moreover, CT makes use of Kirchhoff's voltage and current laws and is widely employed owing to its simplicity and effectiveness.

3.2 Coupling-based WPTs

As a concept, the NF WPT systems rely on the coupled resonators in close proximity whose different coupling types are given in Fig. 3.1. The capacitive (also known as the electrostatic (ES) induction) or inductive (EM induction) coupling techniques can be used to develop NF WPT [81]. Furthermore, the latter type can be advanced to the MRC principle, in which transmitting and receiving nodes of the designed system oscillate at the identical resonant frequency (f_0) [82]. This essentially enables focusing the power at a single frequency and, thus, PTE of WPT improves [83].

3.2.1 Capacitive Coupling

The capacitive coupling or capacitive power transfer (CPT) is also called electric induction-based WPTs and employs the electric field ($\mathtt{E}$). In turn, $\mathtt{E}$ can be created by utilizing metal plates on each separate Tx and Rx resonator which subsequently resulted in the wireless

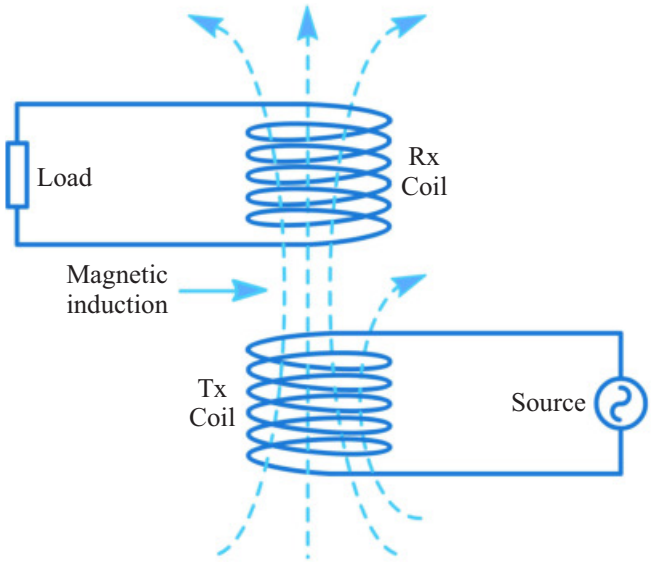

Figure 3.2. The magnetic induction-based WPT system.

power transfer; however, it is imperative to mention that, in this case, the operating frequency is extremely low as compared to the IPT systems [84]. Furthermore, because capacitance is highly reliant on the perfect alignment between Tx and Rx, this type of WPT is very sensitive to any misalignment. Although CPT is no often the preferred method, it is still applied in EV charging, low-power integrated circuits, and a variety of consumer electronics. It is also worth mentioning that this type of coupling is less employed because the significant power transfer requires high voltages, the transmission distance is short, and the $\mathtt{E}$ intensity is hazardous to humans. In addition, the human body shows a stronger response to $\mathtt{E}$ than to $\mathtt{H}$, thus, the amount of the transferred power is significantly reduced, which might also result in tissue heating.

3.2.2 Inductive Coupling

Fig. 3.2 depicts the theoretical principle of magnetic induction-based WPT systems. The inductive coupling (IC) is an NF transmission technique that uses $\mathtt{H}$ to transfer energy between two coils. It is possible to achieve it by placing the primary and secondary coils in the coupled region. In other words, a magnetic link with an air gap between the Tx and Rx sides is used to transfer power wirelessly. When two coils are separated by a short distance, energy is transferred using the principle of mutual induction. Furthermore, when a current passes through the Tx coil, it generates $\mathtt{H}$ over a small range. In turn, bringing the Rx coil to the created $\mathtt{H}$ area leads to the induction of voltage or current in Rx. As a result, the induced voltage has the potential to wirelessly charge any connected load.

IC-based WPTs or IPTs can be considered as a simple technology since its foundation is essentially a transformer with some air gaps in the core. In this type of coupling,

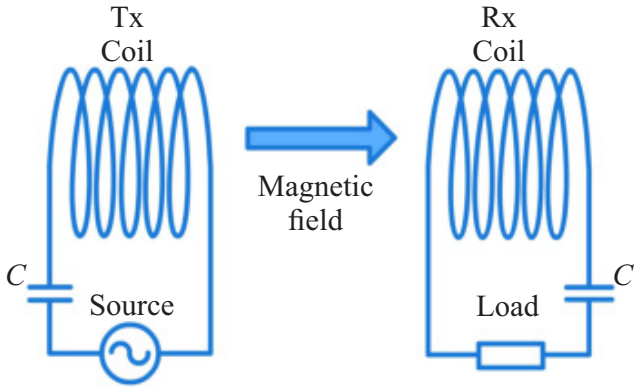

Figure 3.3. The MRC-based WPT scheme.

it is feasible to obtain high PTE; however, the transmission distance is limited to a few millimeters. Furthermore, the IPT-based WPT systems are usually built around a 100 kHz frequency range and are typically bulky as well as heavy due to the use of ferromagnetic cores. It is also important to note that powering multiple devices simultaneously is impossible with this technology.

3.2.3 Magnetic Resonant Coupling

In MRC, the electrical energy is transferred between resonating coils via oscillating H. The general MRC concept is depicted in Fig. 3.3 which is premised on the coupling of the Tx and Rx resonators. As a consequence, high-efficient energy transmission can be obtained due to the strongly coupled resonant coils which resonate at the same frequency. It should be noted that this technique has the potential to be a breakthrough innovation in the evolution of WPTs because of numerous advantages over the other alternatives.

MRC has the ability to transfer power over relatively larger distances and uses the concept of CMT. Moreover, in the case of MRC-based WPT systems, it is possible to power multiple receiving resonators concurrently. In general, its idea is similar to that of IPT but in the former case, the self-inductance and stray or integrated capacitance of the circuit leads to the resonance creation. In this technology, the achieved coil's resonance is regarded as the WPT's working frequency, which normally covers the MHz ranges [84]. This phenomenon is obtained when the frequencies of Tx and Rx harmonize [85]. It should be noted that both IPT and MRC follow the same concept; however, the former uses lumped capacitors for the resonance while it can be achieved by using stray capacitors in the case of MRC-type WPTs. Furthermore, it is feasible to achieve up to 50% PTE over a longer distance, which can be increased from ten to hundred times, by using MRC instead of IPT without reducing the coil size or power consumption. On the other hand, it exists some challenges related to MRC-based WPTs and one of them is keeping the operation at resonance. Also, the created impedance mismatch drastically reduces PTE

in case of the PTD change between Tx and Rx or when different possible misalignment scenarios (lateral or angular) occur [24].

The energy transmission in MRC can be achieved following either loosely or strongly coupled resonators. In this instance, it is worth noting that the strong coupling does not imply high k. Instead, Q of resonators aids in making the coupling strong which can also provide high PTE during the low-coupling regime. It is apparent that the losses such as resistive and radiation degrade the performance; however, they can be eliminated at a rate defined by Q. The followings are critical in determining the developed MRC-type WPT system performance: level of induced power, resonator structure and size, achievable Q, k, and operating frequency of the system [25]. The term efficient MRC-type WPT can be interpreted in two ways: maximum PTE and energy efficiency. It is worthwhile to mention that they have a principal difference. In particular, maximum PTE is the approach that minimizes the losses of primary and secondary resonators by providing perfect impedance matching between them. Furthermore, the energy efficiency takes care of only the losses related to the source (*i.e.*, Tx). Additionally, the WPT systems, that consider only the maximum achievable PTE, are suitable in a wide range of applications requiring only milliwatts range (tens).

3.2.3.1 kQ Product

The coupling phenomenon in the WPT systems can be divided into three distinct categories based on the distance between two resonators: i) undercoupling – the range where resonators are poorly coupled and, as a result, PTE drops abruptly; ii) overcoupling – occurs when two resonators are placed at very close proximity. It leads to the splitting of the working frequency and, subsequently, the highest efficiency is obtained at frequencies other than the initially designed working frequency; iii) critical coupling – this point is considered to be optimal as the maximum energy transfer between Tx and Rx is achieved [65]. For ideal WPTs, k and Q define the maximum achievable efficiency ($\mathrm{PTE}_{\max}$) which can be calculated using (3.3) [86]. Fig. 3.4 shows the effect of k and Q on $\mathrm{PTE}_{\max}$ which highlights their importance. For instance, when $k = 1$, only 68% PTE is obtained for $\mathrm{Q} = 5$; however, it can be improved in accordance with higher Q.

$$\mathrm{PTE}_{\max} = \frac{k^2 \mathrm{Q}_{\mathrm{Tx}} \mathrm{Q}_{\mathrm{Rx}}}{\left(1 + \sqrt{1 + k^2 \mathrm{Q}_{\mathrm{Tx}} \mathrm{Q}_{\mathrm{Rx}}}\right)^2} \times 100. \tag{3.3}$$

It is apparent that variations in the distance between two coupled resonators lead to the change in k. In turn, the k modification can potentially result in the phenomenon known as frequency splitting. Particularly, when PTD is decreased (*i.e.*, overcoupling regime), two peaks occur. The influence of the distance change is presented in Fig. 3.5. It reveals that, when the distance between coupled modifies, the peak of resonant frequency splits

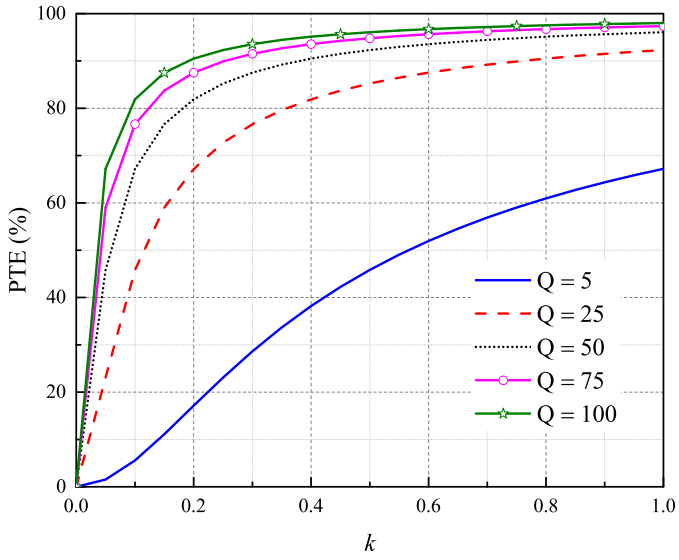

Figure 3.4. Maximum theoretical achievable PTE.

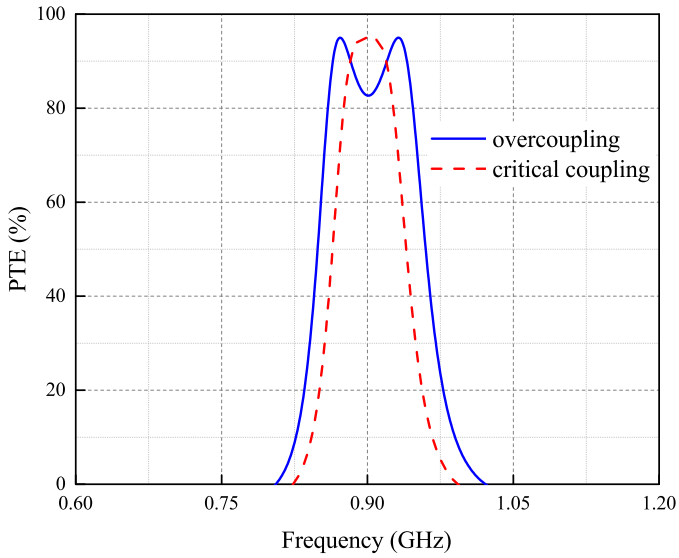

Figure 3.5. The frequency splitting phenomenon.

into two. This means that the maximum electrical quantity of operating frequency (initial resonance) stays under a weak coupling regime, as a result, PTE drops.

3.2.3.2 Performance Evaluation

The amount of delivered energy to the receiver side through a non-physical medium mainly defines the performance of developed WPT which is known as PTE. Therefore, there is a need for this particular parameter increase. In essence, its quantity implicates the ratio of the power at Tx (P_{out}) to the power at Rx (P_{in}), which is given by (3.4).

$$\text{PTE} = \frac{P_{\text{out}}}{P_{\text{in}}}. \tag{3.4}$$

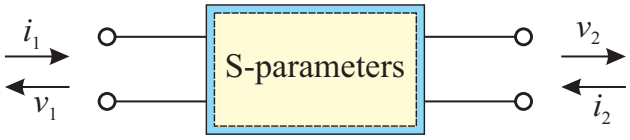

Figure 3.6. The two-port network illustration.

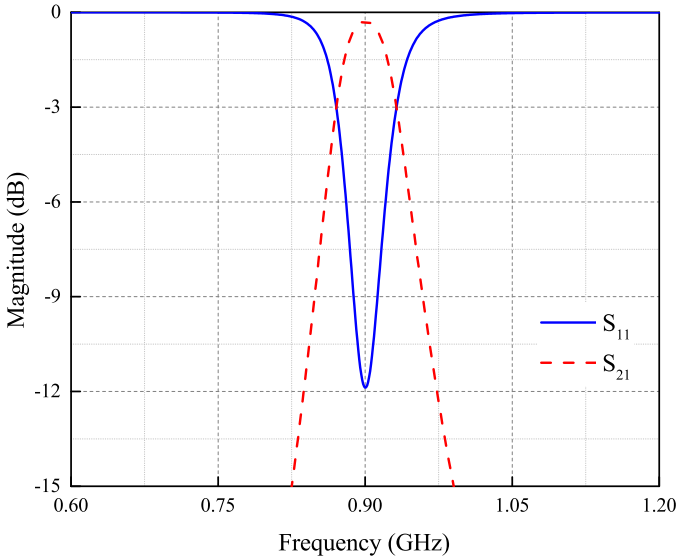

Figure 3.7. The WPT results: S-parameters vs frequency.

In general, any given WPT system can be analyzed using the basic principles of the two-port network as illustrated in Fig. 3.6. This network-based characterization can be provided by using various matrices such as the transfer, impedance, and scattering. It is imperative to note that the latter can be utilized to characterize the WPT circuit. The respective S-matrix of the two-port network is given in (3.5). Given that $i_2 = 0$ and $Z_{\mathrm{L}} = Z_0$ (*i.e.*, load and input impedance), the input reflection coefficient (S_{11}) and transmission gain (S_{21}) can be defined as $\mathrm{S}_{11} = \frac{v_1}{i_1}$ and $\mathrm{S}_{21} = \frac{v_2}{i_1}$, respectively.

$$\begin{bmatrix} v_1 \\ v_2 \end{bmatrix} = \begin{bmatrix} \mathrm{S}_{11} & \mathrm{S}_{12} \\ \mathrm{S}_{21} & \mathrm{S}_{22} \end{bmatrix} \begin{bmatrix} i_1 \\ i_2 \end{bmatrix}. \tag{3.5}$$

Another approach, that determines WPT's PTE, uses the S-parameters. Particularly, the values of S_{11} and S_{21} and the expression (3.6) are employed to define achieved PTE of the designed WPT system. It is important to mention, in this regard, that the minimum allowed value for S_{11} is -10 dB to grant minimum losses at the input port. For instance, the obtained S-parameters of MRC-based WPT are depicted in Fig. 3.7. The given values of $\mathrm{S}_{11} = -11.88$ dB and $\mathrm{S}_{21} = -0.35$ dB show that realized WPT's PTE is equal to 98% at 900 MHz. In addition, another key metric of WPTs is known as FoM which is calculated utilizing (3.7). It effectively considers all pivotal WPT system characteristics such as the resonator size, PTE, and PTD.

$$\text{PTE} = \frac{|\text{S}_{21}|^2}{1 - |\text{S}_{11}|^2}, \tag{3.6}$$

$$\text{FoM} = \text{PTE} \times \frac{\text{PTD}}{\sqrt{\text{avearge size}}}. \tag{3.7}$$

3.3 Resonator

The MRC technique allows high PTE over relatively close proximity by means of proper resonance matching between the Tx and Rx coils. Thus, conventional coils, including planarized ones, have been broadly utilized to develop the WPT end-modules (*i.e.*, resonators). Near the resonance, they can be modeled as a parallel resistance (R), L, and capacitance (C) circuit. In these structures, a proper LC combination generates the angular resonant frequency (ω_0) given by (3.8) [87]. Furthermore, the input impedance of the parallel RLC circuit is calculated using (3.9).

$$\omega_0 = 2\pi f_0 = \frac{1}{\sqrt{LC}}, \tag{3.8}$$

$$Z_{\text{in}} = \left(\frac{1}{R} + \frac{1}{j\omega L} + j\omega C\right)^{-1}. \tag{3.9}$$

In this instance, it should be noted that precise modeling depends on the techniques employed to design resonators. For instance, a current source is utilized to analyze the parallel RLC circuits. In such a scenario, the source's impedance is considered to be completely resistive at the resonant frequency. Furthermore, an open circuit is formed by a parallel combination of L and C. As a result, the total current passes through the resistor at the resonance. Finally, based on the current divider rule and the current flowing through the resistor, as a function of frequency, (3.10) is obtained. Here, I_{S} is a current provided by the source. The transfer function of parallel RLC is expressed by (3.11).

$$I_R = I_{\text{S}} \frac{j\omega L}{(R - \omega^2 LCR) + j\omega L}, \tag{3.10}$$

$$|H(\omega)| = \frac{\omega L}{\sqrt{(R - \omega^2 LCR)^2 + (\omega L)^2}}. \tag{3.11}$$

3.4 SGP Technique

The photonic band-gap structure (PBG) or SGP techniques can achieve stop-band or band-gap effects and are, thus, very useful in microwave circuit design [88, 89]. The number of lattices, lattice spacing, and relative volume fraction influence the rejection of desired frequencies in PBG; however, in SGP, it is mainly defined by the physical dimensions of etched slots [90, 91]. The main SGP concept lies in altering the ground plane's current

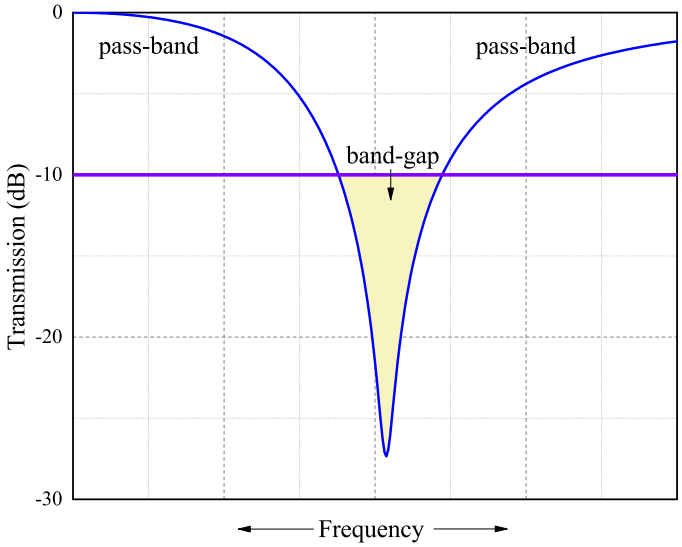

Figure 3.8. The band-gap effect.

distribution by introducing any type of slot on it, consequently, the circuit's L and C change accordingly. The SGP approach has several advantages, including the modeling simplicity, ease of the WPT equivalent circuit development, prototype fabrication, *etc*. Therefore, SGP is favored over the PBG technique in the realization of various filtering structures [89, 92, 93]. The general analysis of the SGP-based resonators is challenging and, hence, the available EM simulators are used to overcome the associated issues [94]. Furthermore, the critical parameters of SGP-type circuits can be retrieved by employing LC resonant EC; however, this approach is unable to describe the geometry of the utilized slot, thus, is unique for any given shape. On the other hand, the parametric extraction of the specific slot necessitates the quasi-static EC construction [47].

The existing literature contains several analyses related to the SGP method from various perspectives. For example, it was demonstrated that the circuit's performance can be enhanced by considering the U and V slots in lieu of the previously utilized conventional dumbbell-shaped SGPs [95]. Furthermore, the bending technique has shown its effectiveness in the further resonator size-reduction [96]. On the other hand, the authors in [97] achieved substantial miniaturization by developing a tunable filter that makes use of varactors. Another ultra-compact tunable band-stop filter (BSF), exhibiting high Q, was realized utilizing the E-shaped slots on the ground plane [89]. Moreover, it was reported that the slots with asymmetric geometries outperform the symmetric shape-based resonators in terms of the circuit miniaturization [98].

The idea of the band-gap effect, based on the transmission coefficient loss, is aptly illustrated in Fig. 3.8. The band-gap region is typically defined as the frequency range corresponding to an attenuation loss of less than -10 dB [99]. The pass-band, on the other hand, is the region where its value is close to 0 dB. In general, the unloaded resonator

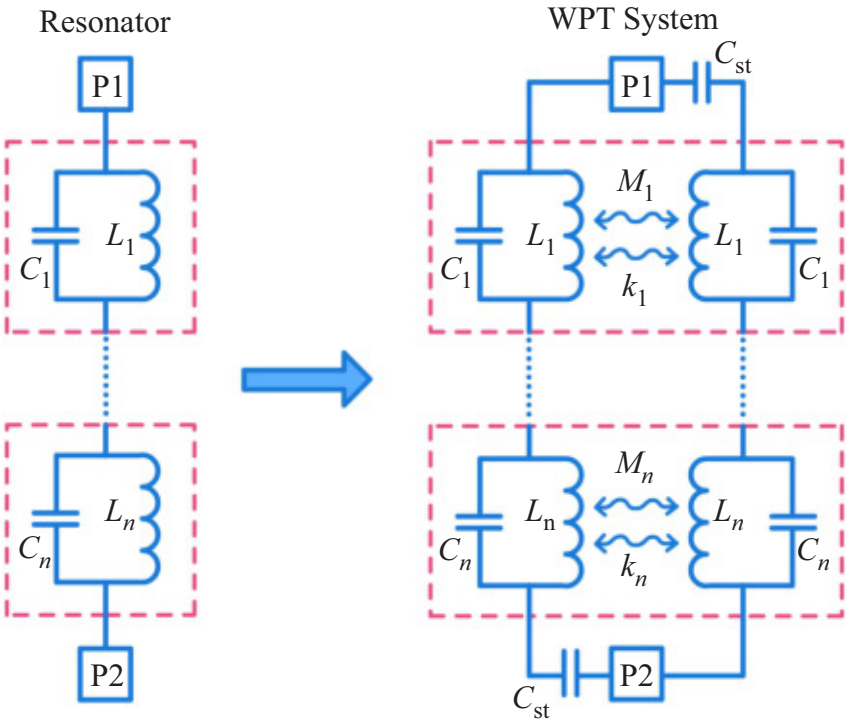

Figure 3.9. The equivalent circuits.

modeling is equivalent to that of parallel RLC due to their resonant circuit nature [89]. The respective values of L, C, and R can be extracted from available EM simulation software and in consonance with (3.12) – (3.14). Here, the term f_c represents the "−3" dB cut-off frequency and the units for L, C, and R are nH, pF, and kΩ, respectively.

$$L = \frac{Z_0(f_0^2 - f_c^2)}{2\pi^2 f_0^2 f_c^2}, \tag{3.12}$$

$$C = \frac{1}{4\pi^2 f_0^2 L}, \tag{3.13}$$

$$R = \frac{2Z_0}{\sqrt{\frac{1}{|S_{11}(2\pi f_0)|^2} - \left(2Z_0\left(2\pi f_0 C - \frac{1}{2\pi f_0 L}\right)\right)^2} - 1}, \tag{3.14}$$

3.4.1 Equivalent Circuit

In general, EC of SGP-type resonators and the corresponding WPT system is very important for the achieved result validation. It is pertinent to mention that the two-step validation gives confidence in the designed WPT system before the eventual fabrication. The most commonly used SGP-based resonator EC is a parallel LC circuit, illustrated in Fig. 3.9, whose values can be defined through appropriate application of Eqs. (3.12) and (3.13). Furthermore, EC can be further used to develop EC of the SGP-based WPT system which is achieved by coupling two LC circuits as shown in Fig. 3.9. Here, M and

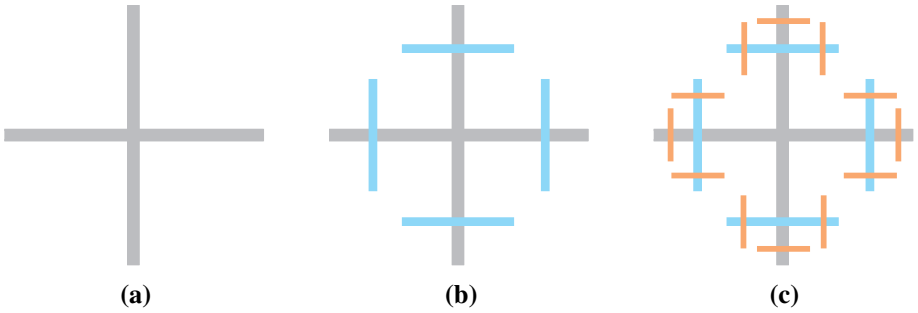

Figure 3.10. The considered fractal iterations: (a) 1st; (b) 2nd; (c) 3rd.

k appear because of the coupled resonators while C_{st} is incorporated for the impedance agreement purposes [46].

3.5 SGP-based Filtering Structures

Different filtering structures are widely used in modern wireless communication, which naturally necessitates the development of new design techniques. In this context, the SGP technique plays a critical role because it allows for the simplification of the miniature filter design process. As a result, a number of filters such as LP (low-pass) [100], BP (band-pass), and BSF have been realized. Furthermore, it has been established that BSFs based on the SGP technique are widely utilized to develop the MRC-type NF WPT systems. Therefore, for the sake of completeness, some design examples of different SGP-based filter structures are provided in this sub-section.

3.5.1 BSF

This subsection presents the design of SGP-based BSF as a demonstrator. In particular, the *plus-shape fractals*, depicted in Fig. 3.10, were employed as a slot-type and introduced on the ground plane. The obtained results of designed BSFs (*i.e.*, occurred resonances) with different fractal iterations are presented in Fig. 3.11. It can be observed that more iteration steps result in the resonance shift toward the lower frequency regime. In addition, it is pertinent to note that f_0 can be moved to any desired one as per the need of the design specifications. This can be achieved by optimizing the slot parameters or by adding an external capacitor (C_{e}), with the appropriate value, to the resonator.

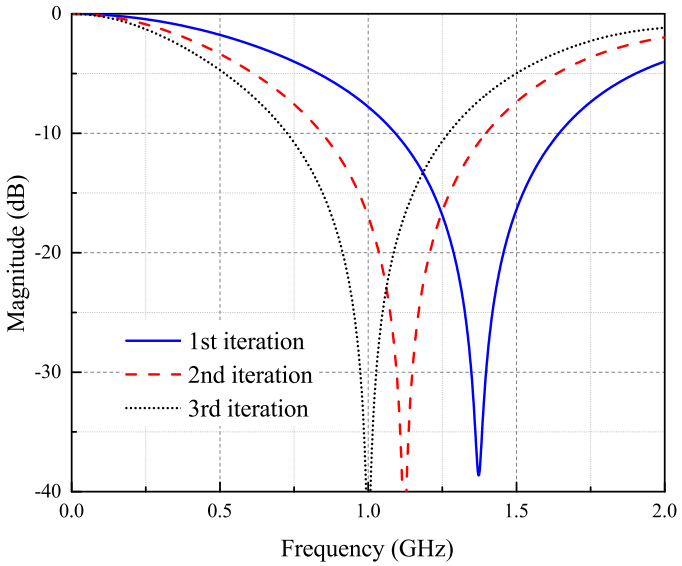

Figure 3.11. Results for BSF with different fractal steps: S_{21} vs f_0.

3.5.2 D-BSF

It is apparent that the MB operation is extremely important taking into consideration MB WPTs. Therefore, the D-BSF (dual-band stop filter) development technique is presented in this subsection. The required dual resonance can be achieved using the cascaded method, *i.e.*, cascading two proposed SGP-type resonators. In particular, the fractal slots (with all three iterations) were cascaded two times. As previously stated, by using two external capacitors, it became possible to shift the initial resonances to the preferred ones. The required values of those placed capacitors can be calculated using (3.14). Furthermore, the obtained EC and EM results of the DB resonator are depicted in Fig. 3.12 which shows two distinct resonances at the practical frequencies of 433 MHz and 900 MHz. It is pertinent to note that there is a perfect match between the two provided results.

3.5.3 W-BSF

Some specific applications may necessitate the design and development of BSFs with broad-band rejection properties. This specific subsection, therefore, briefly discusses the realization of SGP-based W-BSF (wide-band stop filter). To fulfill this goal, at first, the considered fractal slots have been cascaded three times. Then, W-BSF can be optimized by changing the slot parameters to broaden or shrink the -10 dB fractional bandwidth (BW) as per the given need. In turn, the latter can be moved by adding capacitors, with the same values, to the excitation gap. Moreover, Fig. 3.13 presents the obtained results of W-BSFs with and without integrated capacitors. It can be seen that a high capacitor value leads to smaller BW and shift to lower frequencies. It reveals that no C_e, $C_e = 1$ pF, and $C_e = 4$ pF resulted in BW of 1.5 GHz, 0.87 GHz, and 0.34 GHz, respectively.

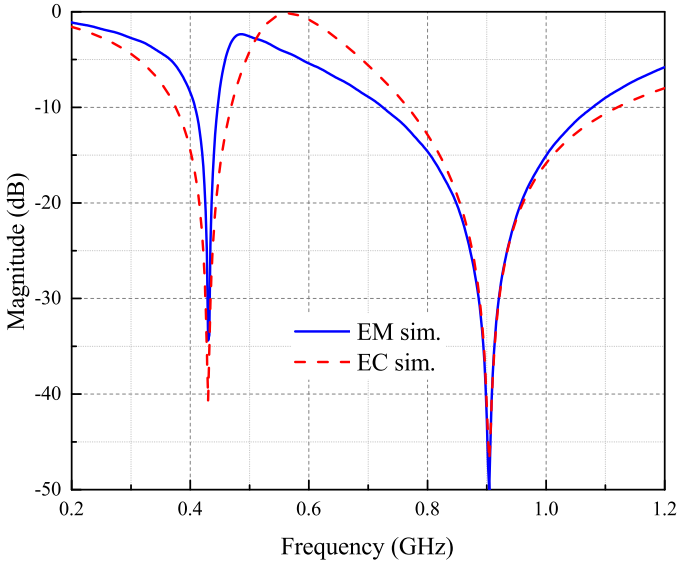

Figure 3.12. The obtained simulation results for D-BSF: S_{21} vs f_0.

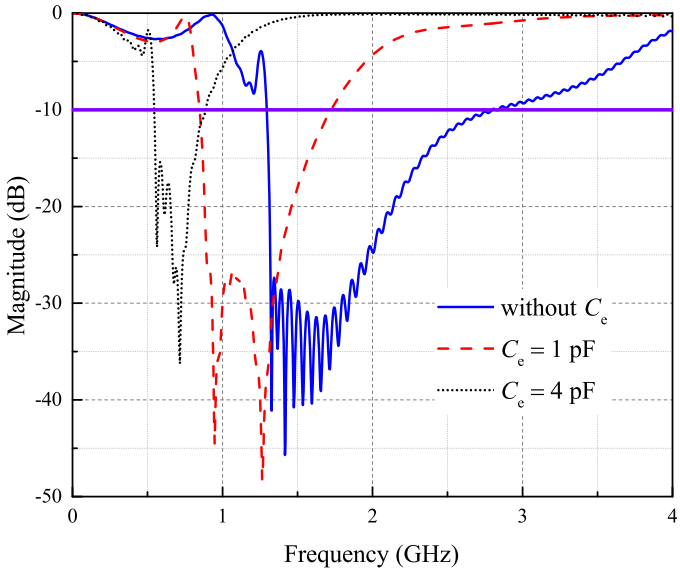

Figure 3.13. The obtained EM simulation results for W-BSF: S_{21} vs f_0.

Summary

It can be briefly concluded that the MRC-based WPT systems show some advantages over IPT and CPT. In particular, the operational frequency of such systems can be at a high MHz region. Furthermore, the MRC-type WPT systems have the ability to send power over relatively long distances and achieve higher PTE. In addition, the SGP technique has demonstrated its ability to design extremely small-size resonators that can be used to develop MRC-type WPTs.

Chapter 4

Single-band WPT Systems

This chapter describes the development of two distinct SB WPT systems that can be employed for the purpose of wireless power or data transfer. In particular, it includes the comprehensive analysis, simulation modeling, and experimental validation of both realized SGP-based WPTs. Furthermore, it is important to note that two different impedance matching techniques were discussed that have been aptly used to design WPTs. Finally, a flowchart is provided that appropriately portrays the generic methodology of the SGP-based WPT development.

4.1 Introduction

As noted previously, the WPT system enables the transmission of electrical energy without cables. In this instance, several SGP-based WPTs have been proposed to overcome some limitations associated with the coil-based WPT systems. For example, the authors in [42] reported PTE of 68.5% when resonators with 40×40 mm^2 area were separated by 50 mm. The design in [50] achieved a considerable size reduction; however, realized PTE demonstrated only 65%.

It is well established that the MRC-type WPT systems can be attained using either various existing coil structures or SGP-based resonators; however, it is common practice to employ the latter in applications requiring small-size and robust end modules. As a consequence, the development of NF SGP-based WPT is becoming increasingly popular nowadays. A brief literature survey reveals that the k change and different misalignment between the coupled resonators degrades obtainable PTE significantly. Therefore, it is extremely vital to develop MRC-based WPTs that are insensitive to misalignment and k variations [63]. For instance, the self-adaptive method has shown its effectiveness in realizing the high-performance WPT system regardless of PTD and k variations [83]. On the other hand, the self-phasing technique, possessing the power focusing capability, has proven its usefulness in improving achievable PTE during the potential misalignment between Tx and Rx [81]. In addition, another robust WPT to the misalignment has been achieved by designing the butterfly-type resonator that can generate greater $\mathtt{H}$ [101].

4.2 Motivation

The critical parameters of any designed WPT system are certainly high PTE, a larger operation range, and comparatively small resonators. Although these parameters are equally important some of them may be more essential depending on the specific application. For example, the resonator size is very critical in biomedical applications whereas in consumer electronics it might be PTE. Apparently, enhancing all these parameters at once is challenging, thus, there is always a significant trade-off among them during the design, which is mainly dictated by a final application. It is also important to note that the WPT performance is highly reliant on the slot shape used to build the necessary resonators.

Keeping the aforementioned in the perspective, the main motivation of this chapter is twofold: i) firstly, advancing the recent progress of SB WPTs (improving the main WPT characteristics) by analyzing and effectively utilizing different slots; ii) secondly, investigating the specific circular slots to fully comprehend their impact on the WPT system performance. As a consequence, the appropriate studies and performed analysis may lead to the realization of performance-enhanced SGP-based WPTs that can be suitable for emerging applications requiring a low-power regime.

4.3 Contribution of the Chapter

The key contributions of this Chapter are listed below:

- The *highly-efficient WPT system* has been developed using the *plus-shaped SGP* structure. To be more specific, the designed resonator oscillated at the practical 400 MHz frequency and possesses the area of 30×30 mm^2. Furthermore, realized WPT exhibited superior performance, with PTE of 86% when PTD $= 35$ mm.

- Three *circular slots* with slightly different geometries were *thoroughly examined* in terms of achievable Q and generated $\mathtt{H}$. As a result, it was observed that the *Archimedean coil-type slot* outperforms the other two shapes under consideration. Therefore, another very compact SB WPT system has been realized that takes the advantage of the Archimedean coil slots, in particular, increased $\mathtt{H}$ and subsequent improved PTD.

- The *systematic design* and *realization methodology* of the generic SGP-based WPT system is elaborated. The presented structured design approach incorporates all key WPT system implementation steps (*i.e.*, analysis, modeling, experimental validation) and aids in the development of small-size high-performance WPTs. Furthermore, the provided methodical WPT realization strategy can be also useful in the design of DB and MB WPT systems.

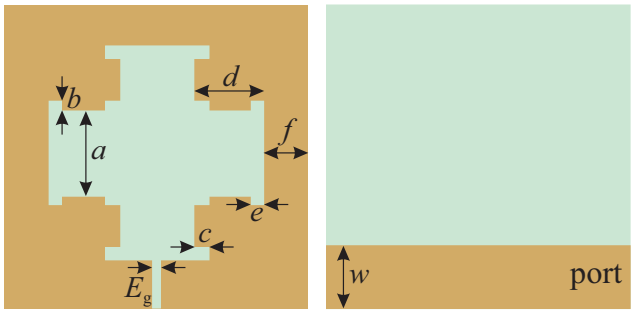

(a) **(b)**

Figure 4.1. The proposed resonator for WPT: (a) bottom; (b) top.

Table 4.1. The optimized dimensions of the slot geometry.

Parameters	a	b	c	d	e	f	E_g	w
Dimensions (mm)	6	0.5	0.5	6	1	6	0.5	1.9

4.4 Plus-shaped SGP-based WPT System

This subsection presents the design and experimental validation of highly-efficient WPT. The SGP-based resonators for the NF WPT development are designed employing the *plus-shaped* slot depicted in Fig. 4.1. It is a common practice to use any available three-layered Rogers' boards to construct the required resonator. Particularly, in this design the RO4350B board, with relative permittivity (ε_r) of 3.48, was utilized. It possesses a single layer of the substrate coated by an annealed copper from bottom and top sides. In addition, the substrate height (h_s) is 1.524 mm, and the copper thickness (h_c) is 0.035 mm. It is worth mentioning that the proposed slot is introduced on the ground plane. The transmission line, which also serves as a feed line, is located on the top side (Fig. 4.1b). Furthermore, because ML is normally matched to the $50\ \Omega$ impedance, its width (w) is dependent on the operating frequency of the designed resonator. In addition, the optimized slot parameters are given in Table 4.1.

At the outset, the designed plus-shaped slot-based resonators were brought to close proximity to fulfill the coupling. This essentially allows for the extraction of the critical WPT parameters such as L, C, k, and M. It is apparent that the resonator's L and C produced by E_g aid in the resonance. In this instance, it is pertinent to mention that the obtained resonance can vary from the initially selected working frequency of the WPT system. Therefore, C_e is incorporated to shift f_0 to the intended WPT frequency of 400 MHz. The required value of C_e can be defined using (3.8) whereas L is computed employing (4.1). Furthermore, the needed value of C_{st} (*i.e.*, open-stub capacitance) is determined

utilizing (4.2), where L_{eq} is defined by (4.3) [93].

$$L = \frac{\text{Im}(\text{Z}_{11})}{2\pi f_0}, \tag{4.1}$$

$$C_{\text{st}} = \frac{25.33}{L_{\text{eq}} f_0^2}, \tag{4.2}$$

$$L_{\text{eq}} = \frac{L}{\left(1 - \left(\frac{f_c}{f_0}\right)^2\right)}. \tag{4.3}$$

In general, the EM simulation results can be verified through appropriately constructed WPT EC. In turn, this task can be completed by extracting the essential WPT EC elements. At the very beginning, the f_0 and f_c values should be retrieved from the performed EM simulations. The obtained simulated results revealed that the operating frequency was split into two peaks. As a result, f_e (electric wall) and f_m (magnetic wall) should be considered during the k value extraction as given in (4.4). Moving forward, occurred M due to the coupled resonators is determined by (4.5). Finally, obtaining the values of all circuit elements enables the construction of WPT EC. As a consequence, the EM and EC results of the designed WPT system can be compared, which is discussed in the following subsection. In addition, the modeled WPT performance can be evaluated in terms of PTE and FoM using (3.6) and (3.7), respectively.

$$k = \frac{f_e^2 - f_m^2}{f_e^2 + f_m^2}, \tag{4.4}$$

$$M = k \times \sqrt{L_{\text{Tx}} L_{\text{Rx}}}. \tag{4.5}$$

4.4.1 Simulation Results and Discussions

It is imperative to note that the designed resonators were coupled at 25 mm. Subsequently, Fig. 4.2 compares the EM and EC simulated results obtained from the Computer Simulation Technology (CST) and Advanced Design System (ADS), respectively. It can be observed that the provided results are in good agreement, which validates constructed SGP-based WPT EC. Calculated PTE that uses the resulted S_{21} and S_{11} values at 400 MHz corresponds to 86%. Furthermore, as noted previously, the distance change between the coupled resonators has a substantial effect on the WPT performance. Therefore, PTE of the developed WPT system was tested under varying PTDs, as shown in Fig. 4.3. In this regard, it is worth noting that the PTD variation results in different k and M, causing f_0 to deviate from the originally designed one; however, the difference is negligible – approximately 10 MHz. The results reveal that the WPT system has about 86% efficiency between 20 mm and 35 mm. This essentially implies that the developed SGP-type WPT system is resilient to the potential PTD changes within that range.

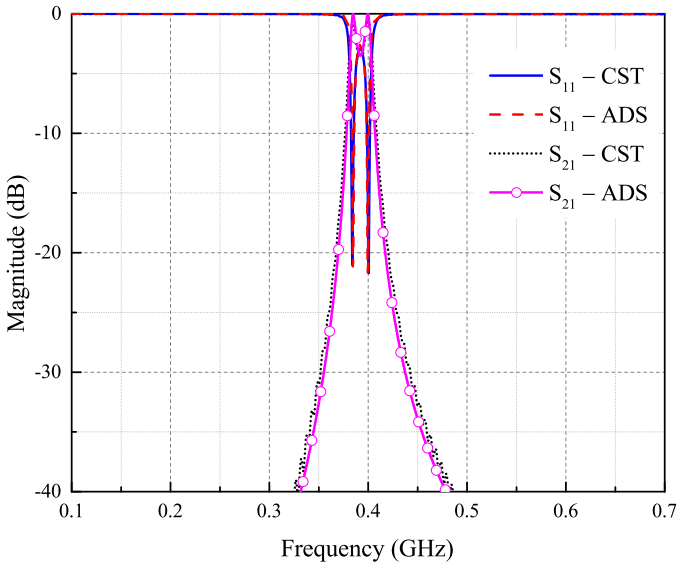

Figure 4.2. The obtained simulation results at 25 mm.

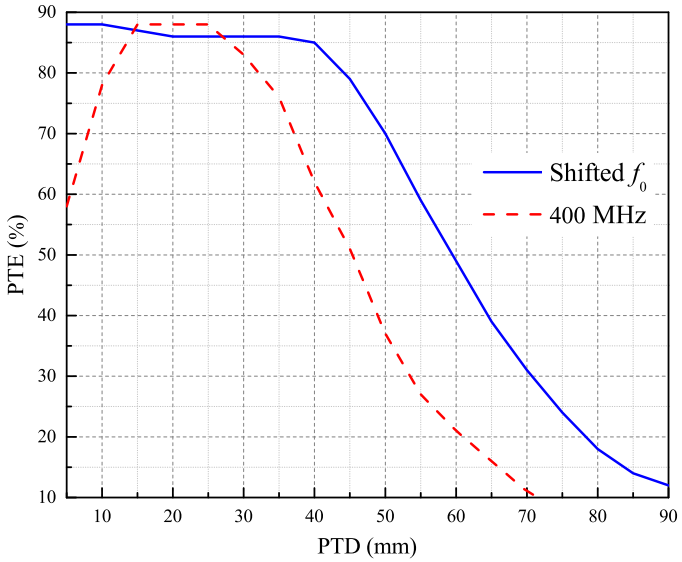

Figure 4.3. The WPT efficiency vs PTD.

4.4.2 Experimental Validation

For the designed WPT system validation purposes, two identical resonators (Figs. 4.4a and 4.4b) were fabricated using the Rogers' RO4350B board. Furthermore, the 5.3 pF SMD-type (surface mount device) capacitors were soldered to both prototypes to ensure $f_0 = 400$ MHz. Then, two realized resonators were coupled at 25 mm to measure the necessary S-parameters, as depicted in Fig 4.4c. As a consequence, this enables the evaluation of the realized SGP-based WPT system. Fig. 4.5 represents obtained S_{21} and S_{11} from the carried-out experimental measurements. In addition, the calculated efficiency is 80% based on the experimental data, which validates both design and particular SGP-type WPT system concepts.

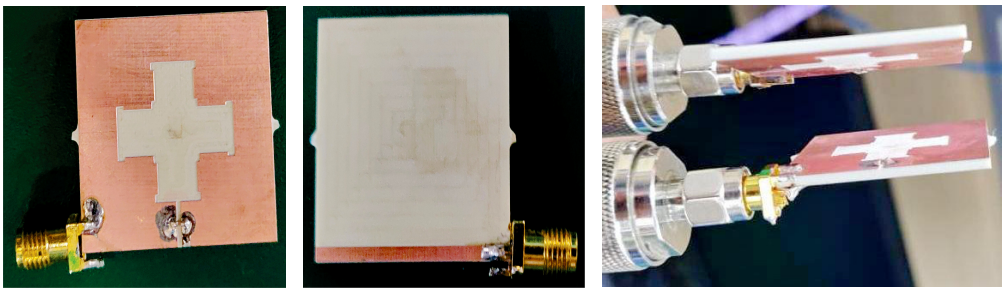

(a) **(b)** **(c)**

Figure 4.4. The realized WPT system and experimental setup: (a) bottom; (b) top; (c) coupled resonators.

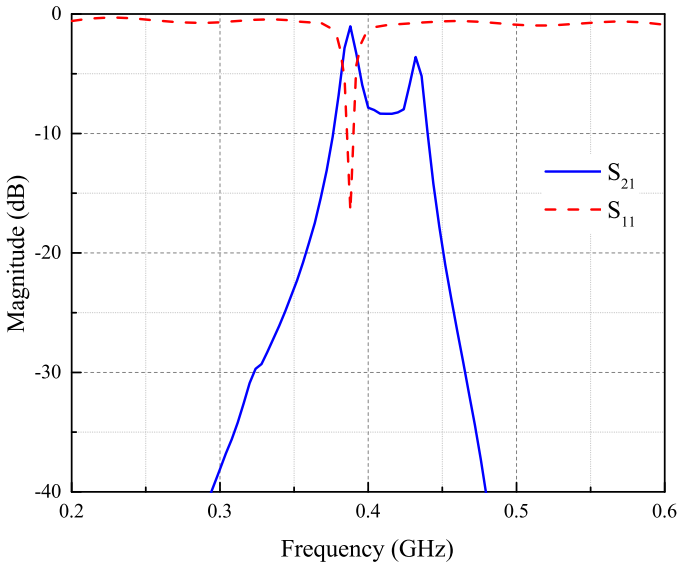

Figure 4.5. The measured results.

4.5 Archimedean Coil-shaped SGP-type WPT

4.5.1 SGP-based Resonator Analysis

Recently, the SGP-type resonators have been broadly utilized in the design of NF WPTs with superior performance. In this regard, it is important to note that the designed resonators mainly predetermine the resultant WPT system performance. Keeping this in the perspective, three circular-type slots with distinct geometries were investigated. In particular, the actual impact of the circular-, ring-, and Archimedean coil-shaped slots on the resonator's main characteristics have been thoroughly examined. Fig. 4.6 depicts the analyzed circular slots etched on the ground plane. Following that, the performed study results enabled the identification of the best circular-type slot, which was then aptly used to develop a high-performance WPT system.

At the outset, all three resonators were developed on the same board area of 20×20

(a) **(b)** **(c)**

Figure 4.6. The compared distinct slots: (a) case 1; (b) case 2; (b) case 3.

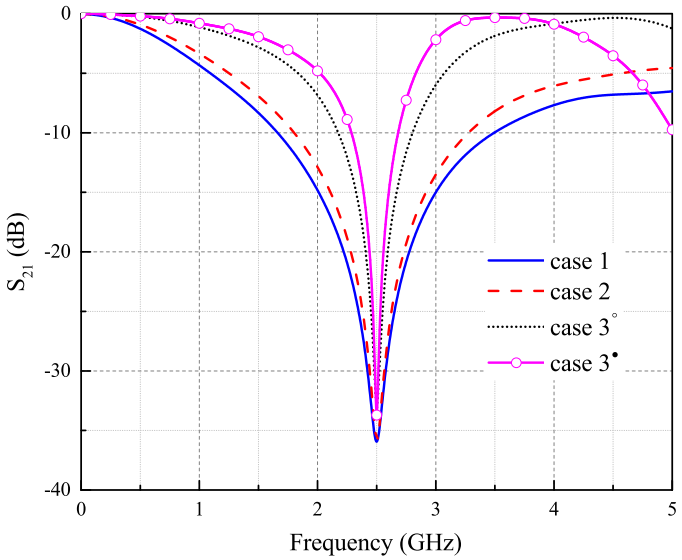

Figure 4.7. The obtained S_{21} values (°1 turn; •2 turns).

mm^2 to ensure accurate and valid comparison. Moreover, irrespective of the utilized slot type, all three designed resonators oscillate at 2.5 GHz. The developed SGP-based resonators are modeled through a parallel RLC circuit whose respective values can be found using Eqs. (3.12)−(3.14). Initially, the SGP-type resonators were analyzed in terms of Q which can be defined by employing (4.6) [89]. The simulation results are presented in Fig. 4.7 while the exact Q and other circuit element values are tabulated in Table 4.2. As can be observed from the results, the circular- and ring-shaped slot-based resonators possess similar Q. This implies that the effect of closed-loop rings, within the circle, on attainable Q is minimal and, hence, can be ignored. Moreover, the resonators using the Archimedean coil-type slot showed greater Q in contrast to the other two options. It was also noticed that increasing coil turns can enhance obtained Q. Particularly, the respective Q values for the Archimedean coils with one and two turns are 29.43 and 44.01. Therefore, taking into account these discoveries, this slot-based resonator was chosen for the SGP-based WPT system design.

$$\mathrm{Q} = 2\pi f_0 CR. \tag{4.6}$$

Table 4.2. The SGP-based resonator comparison.

Slot type	C	L	R	Q
circle	0.23 pF	17.72 nH	3.78 kΩ	13.57
rings	0.28 pF	14.54 nH	3.75 kΩ	16.4
Archimedean coil 3°	0.63 pF	6.46 nH	2.99 kΩ	29.43
Archimedean coil 3•	0.87 pF	4.68 nH	3.23 kΩ	44.01

°1 turn; •2 turns.

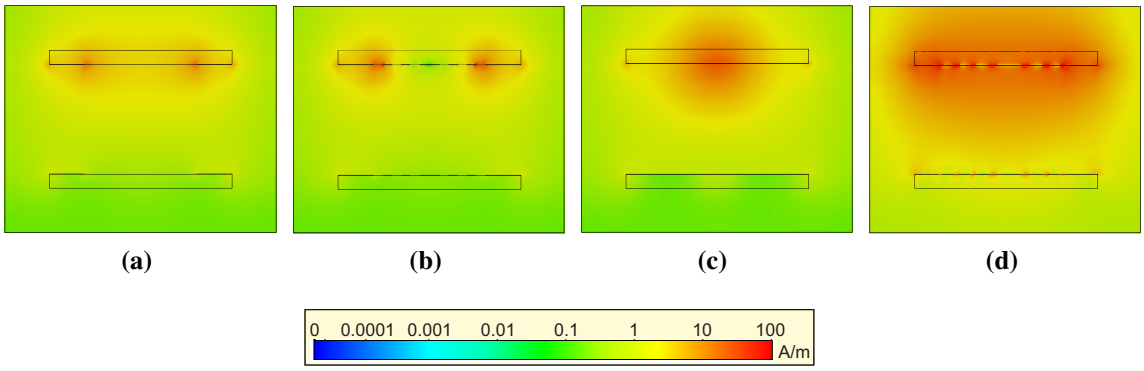

Figure 4.8. H-field between two coupled SGP-type resonators at PTD = 12 mm: (a) 1; (b) 2; (c) 3 (2 turns); (d) 3 (4 turns).

4.5.2 WPT System Development

This subsection presents the development of SGP-based WPT and its respective EC. It is worth noting that the WPT key parameter extraction is carried out using the J-inverter method. Furthermore, the WPT system modeling and EC construction were performed using CST and ADS, respectively. In addition, the key WPT design steps, that make appropriate use of the analyzed SGP-based resonators, are discussed in detail below.

4.5.2.1 Resonator Coupling

The number of Archimedean coil turns has been elevated to four because more turns are capable of providing higher Q. Then, two identical SGP-based resonators were coupled at a distance of 12 mm. This essentially allows examining the amount of generated H around the resonators based on the distinct slots (*i.e.*, three considered cases) which are depicted in Fig. 4.8. Similarly, the four-turn Archimedean coil-shaped slot-type resonator exhibited the greater created H area. In turn, this observation can be explained by the relatively high current concentration on the resonator's ground plane. It is pertinent to note that a larger H area aids in the PTD expansion between Tx and Rx. As a result, the Archimedean coil-shaped slots with four turns, exhibiting greater Q and H, was chosen for further NF WPT system development.

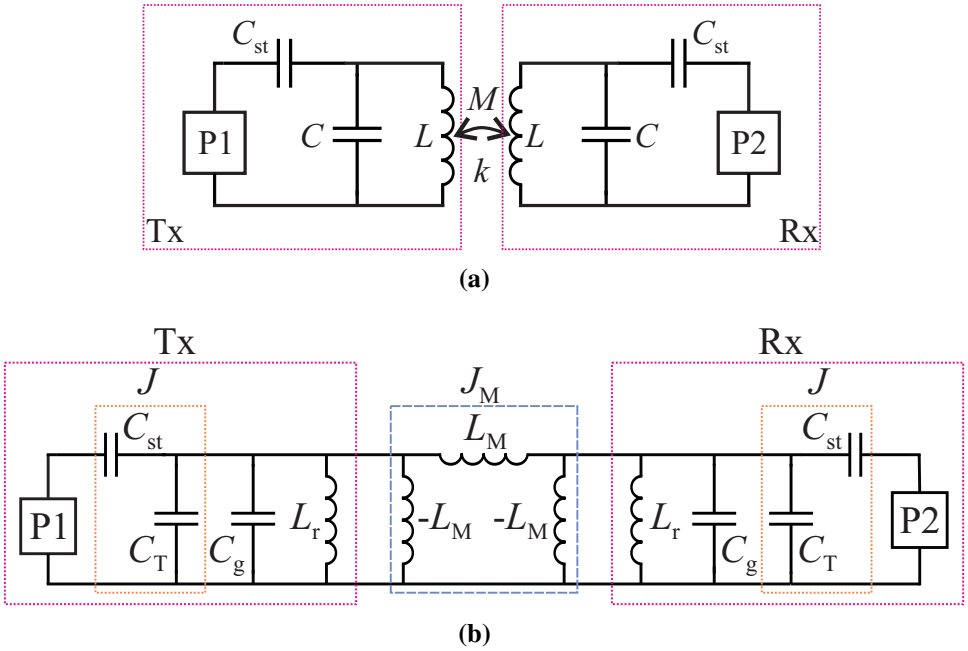

Figure 4.9. (a) WPT EC; (b) J-inverter transform.

Different expressions are used to extract the critical parametric values of coupled-type WPTs. For example, L and C can be defined using (4.1) and (3.13), respectively. On the other hand, (4.7) and (4.8) help calculate the values of R and M, accordingly [102]. The circuit's L and C primarily define f_0; however, integrating a capacitor may be more practical for adjusting it. Furthermore, k of coupled resonators is determined as $k = M/L$, where $L = \sqrt{L_{\mathrm{Tx}} L_{\mathrm{Rx}}}$ [63]. It is imperative to note that maximum PTE can be obtained when two resonators are critically coupled in lieu of the overcoupling regime as it leads to the frequency splitting [83]. The latter case introduces some frequency bifurcation-associated challenges, therefore, the critical coupling is often a viable choice for the high-performance MCR-based WPT design.

$$R = \mathrm{Re}(\mathrm{Z}_{11}), \tag{4.7}$$

$$M = \frac{\mathrm{Im}(\mathrm{Z}_{21})}{2\pi f_0}. \tag{4.8}$$

4.5.2.2 WPT Development

In this design, the J-inverter technique was used to extract the key WPT parameters and perform the required impedance matching. In essence, the J-inverter transform is achieved by slightly modifying generic WPT EC depicted in Fig. 4.9a. The latter is composed of two coupled LC resonators, one of which acts as Tx and the other as Rx. Thus, the critical circuit elements, such as C_{st}, C, and L, have same values. It should be reiterated that C_{st}'s

Table 4.3. The defined parameter values of WPT.

L (nH)	C (pF) calc/opt	M (nH)	k	C_{st} (pF)	l_{st} (mm) calc/opt	w_{st} (mm) calc/opt
43	2.17/2.4	2	0.048	0.85	9/9.1	3.39/3.4

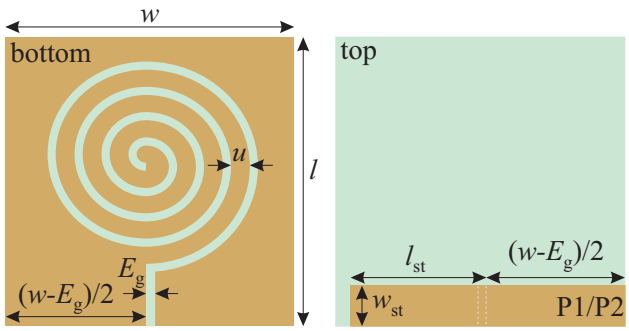

Figure 4.10. The parameters of designed WPT (in mm): $l = 20$; $w = 20$; $u = 1.2$; $E_g = 0.6$.

specific role is to match the resonator impedance to the standard 50-Ω ports. Furthermore, the C_{st} capacitance can be realized using ML as an open-stub.

A newly developed J-transform-based WPT EC is presented in Fig. 4.9b. In this case, M and L help define the k value whereas C can be determined using Eqs. (4.8), (4.1), (3.13). Moreover, Eqs. (4.9)−(4.10) are used to compute the appropriate values of L_M, J_M, L_r, and J while (4.11) aids in the calculation of C_{st} and C_T. It is imperative to note that C_T is expressed as $C_T = C_e - C$. In turn, the value of C_e can be found using (3.13) and considering L_r instead of L. Moving forward, (4.12) helps determine the required length (l_{st}) of open-stub ML, where $\beta = 2\pi/\lambda$ defines the wave number with $\lambda = 300/(f_0\sqrt{\varepsilon_r})$. In this regard, it is worth noting that the f_0 value is used in MHz.

$$L_M = \frac{L^2 - M^2}{M} \text{ and } J_M = \frac{1}{2\pi f_0 L_M}, \tag{4.9}$$

$$L_r = \frac{L^2 - M^2}{L} \text{ and } J = \sqrt{\frac{J_M}{50}}, \tag{4.10}$$

$$C_{st} = \frac{J}{2\pi f_0\sqrt{1-(50J)^2}} \text{ and } C_T = \frac{C_{st}}{1+(100\pi f_0 C_{st})^2}, \tag{4.11}$$

$$C_{st} = \frac{\tan(\beta l_{st})}{2\pi f_0 Z_0}. \tag{4.12}$$

The parameter values, defined using the J-inverter approach, aided in the development of SGP-based WPT. Table 4.3 shows the calculated values that were obtained by properly applying the above-mentioned expressions. It is also worth noting that some of them have been slightly modified to satisfy the initially targeted WPT system specifications. Subsequently, the back side of the resonator was adjusted as shown in Fig. 4.10. Furthermore,

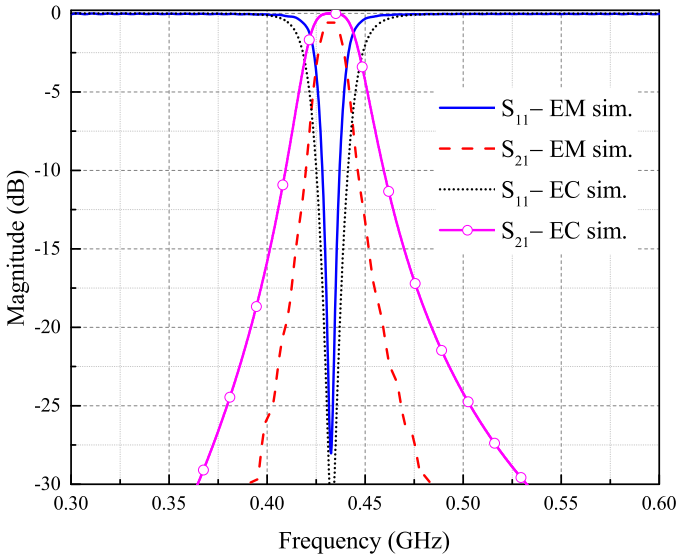

Figure 4.11. Simulated results of the developed WPT system.

a capacitor with 2.4 pF was added to E_{g} on the back side whereas open-stub ML with 9.1 mm length was placed on the top side whose second-end is connected to a port. Consequently, the current flow through ML is achieved by exciting P1 which, in turn, leads to the generation of $\mathtt{H}$ around the resonator. Then, ML of Rx can be excited by moving it to $\mathtt{H}$ produced around the Tx resonator. As a result, P2 will have the capability of receiving the transmitted signal from P1.

In general, the obtained PTE and FoM values assess the performance of the NF SGP-type WPT system. The efficiency can be defined by applying $|\mathrm{S}_{21}|^2$ if the S_{11} value is below -10 dB whereas FoM is calculated using (3.7). The simulation results for the designed WPT system, when Tx and Rx are separated by 20 mm, are shown in Fig. 4.11. In particular, it compares the EM and EC simulations which demonstrate nearly perfect agreement. This appropriately highlights the usefulness of the J-inverter approach in the design of SGP-based WPTs. Furthermore, PTE and FoM of 86% and 0.86 were calculated using the simulation data, respectively.

4.5.3 Experimental Results

The Rogers' RO4350B board possessing ε_{r} of 3.66 was employed for the prototype of the modeled SGP-type resonator. The respective heights of the dielectric material and copper are 1.54 mm and 0.035 mm. It should be noted that for the WPT realization two resonators were fabricated and 2.4 pF SMD-type capacitors were attached to each. Moreover, SMA (SubMiniature version A) connectors were employed to link the SGP-based resonators to the vector network analyzer (VNA). This allows for the required coupling and evaluation of the realized WPT system; however, two resonators should be properly aligned and separated by exactly 20 mm. Furthermore, the depiction of the experimental setup

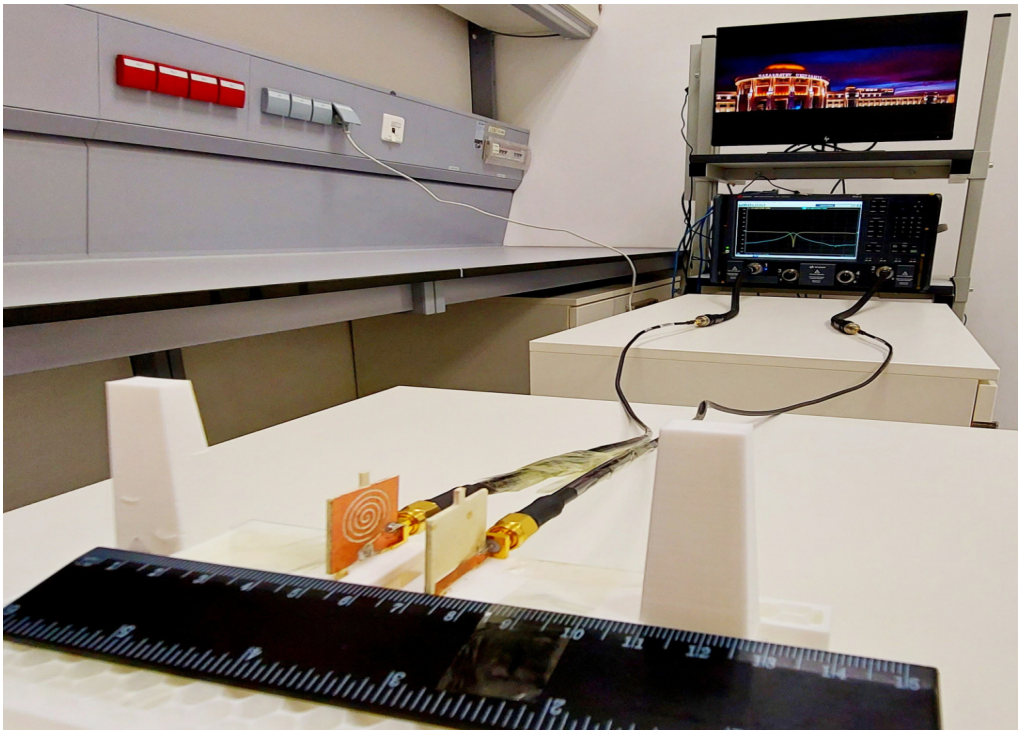

Figure 4.12. The experiment setup.

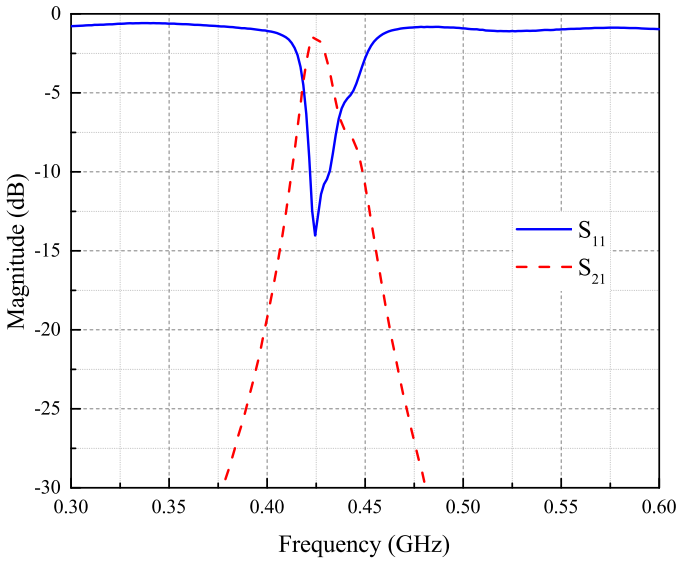

Figure 4.13. Experimental results.

for the measurements is given in Fig. 4.12 while the respective measured S-parameters are presented in Fig. 4.13. In particular, it reveals that $S_{11} < -10$ dB and $S_{21} = -1.41$ dB which demonstrates that the achieved experimental PTE is 72%. In addition, there is a discrepancy between the simulation and experimental results in PTE, which is primarily due to the in-house fabrication, capacitor tolerance, and soldering-related issues. Nevertheless, the obtained measurement results confirm the usefulness of SGP in the compact NF WPT system realization for various low-power applications.

4.6 Systematic SGP-based WPT Development

In general, the design and realization of SGP-based WPTs are challenging, thus, there is a desperate need for the systematic approach that aids in the high-performance WPT system implementation. The realization of SGP-based WPTs includes the following key stages such as resonator design and analysis, EC development, impedance matching to 50-Ω ports, performance evaluation, and experimental validation. In essence, the overall WPT implementation necessitates a significant trade-off among the key parameters including the resonator size, PTD, and PTE. Therefore, many researchers have attempted to propose the optimal design strategy in recent years. Despite the differences in their approaches and techniques, they can still be characterized by a standard systematic procedure. The key premise behind the systemic approach is the development of SB and MB SGP-type WPTs for emerging low-power applications. Fig. 4.14 depicts the systematic SGP-based WPT realization method as a flowchart, with the main steps detailed below:

- To begin, define a slot geometry and choose a substrate for the SGP-based WPT system design.
- At this stage, determine whether the final WPT system is aimed to transfer only power or both. It is worth noting that the former necessitates a single frequency band whereas the latter requires multiple frequency bands. Furthermore, the operating frequency of WPT should be carefully selected so that it conforms to standardized practical frequencies.
- Afterward, define the key WPT parameters, such as the circuit size, PTD, and PTE, based on the prerequisites of the specific application area. For example, some applications may require high PTE whilst in other cases the resonator size is critical.
- Then, design the resonator using the opted slot and taking into account the WPT key characteristics. Define the required value of C_{e} to obtain f_0 at the initially selected frequency. Please note that the SB and MB resonators can be designed employing any available technique.
- After that, construct effective EC for the SGP-based resonator to validate the EM simulation results.
- Following the validation of EM simulations, the designed resonators can be brought to the required proximity to remain within the coupled region. At this stage, ensure that two coupled identical SGP-based resonators are perfectly aligned. This enables the WPT system's EC to be developed, where M and k can be defined using the given expressions in subsection 4.5.2.1.

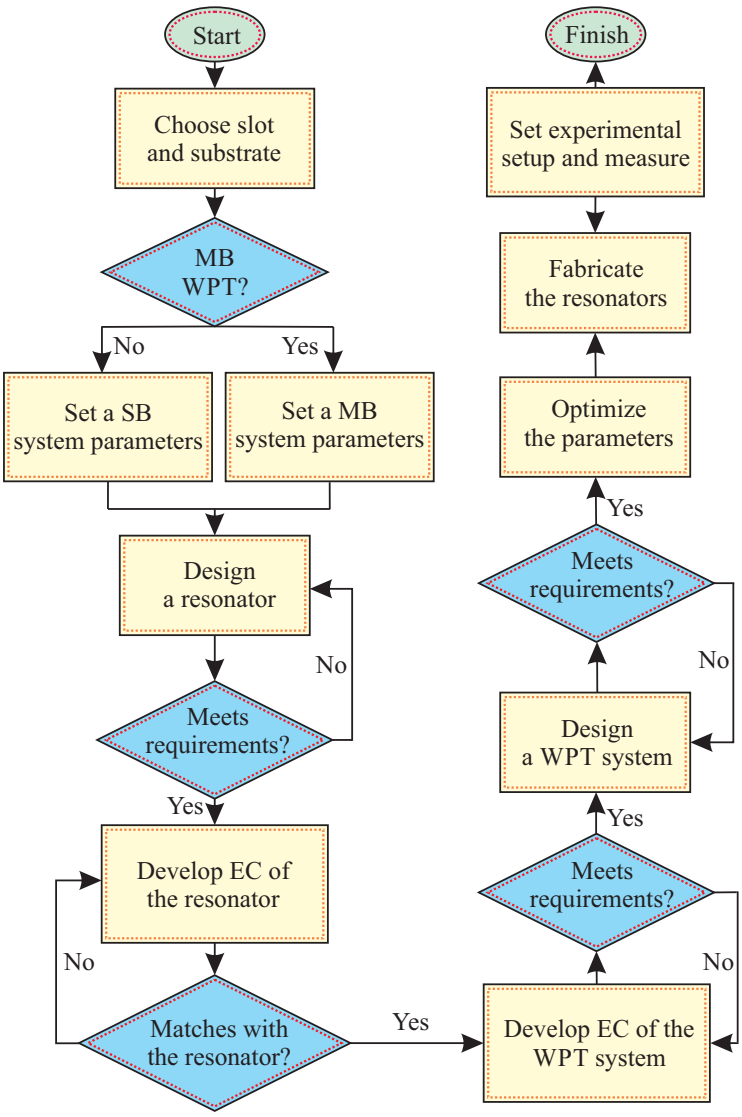

Figure 4.14. The systematic methodology of the SGP-type WPT implementation.

- Match the resonator impedance to $50\ \Omega$, *i.e.*, compute the required value of C_{st}. Then, convert the computed C_{st} value into open-stub ML, subsequently, design the SGP-based WPT system.

- To complete the simulation stage, conduct the critical parameter optimization that aid in achieving the best possible performance.

- After the simulation phase is finished, the designed WPT system can be tested experimentally. To accomplish this, fabricate two resonator prototypes, then solder all necessary circuit elements such as SMD capacitors and SMA connectors.

- Finally, separate and align the fabricated resonators at PTD considered in the simulation environment. Then, connect the resonator's ports to VNA for the implemented WPT evaluation. The performance of the newly developed SGP-based WPT system can be assessed in terms of PTE using the obtained experimental data and (3.6). It is pertinent to mention that the key factors for the successful WPT system design validation are carefully prepared experimental setup and precisely fabricated prototypes.

Summary

This chapter presents the design and experimental validation of two distinct SB SGP-based WPT systems. In particular, one WPT made use of the *plus-shaped* slots whereas another was developed using the *Archimedean coil-type* slots. It is important to note that two different approaches were used to achieve the required impedance matching and parameter extraction. Furthermore, both realized WPT systems possessed an extremely compact board area and demonstrated high-performance PTE and enlarged PTD. This chapter also includes the *systematic* SB and MB WPT system implementation methodology. Finally, developed performance-enhanced WPTs and the provided systematic SGP-based WPT design technique are expected to advance the current state-of-the-art and bring a paradigm shift to this domain.

Chapter 5

Multi-Band WPT Systems

This chapter presents the implementation of ultra-compact SGP-based WPT systems. In particular, dual- and tri-band WPTs have been developed that aid in concurrent power and data transfer. Furthermore, both realized SGP-type WPTs were validated through the carried-out experimental measurements. It is also important to mention that WPTs are designed to operate at practical ISM bands and demonstrate high performance. In addition, a small-size digital metasurface reflector was developed that can help facilitate the emerging SWIPT and WBAN applications.

5.1 Introduction

A brief overview of various WPT system classifications is depicted in Fig. 5.1. The SB system (single-band Tx and Rx) has the capability to operate as *wireless power transfer* or *wireless information transfer* (WIT). On the other hand, the DB system can allocate one band for WPT purposes whereas the other band can be earmarked for simplex WIT, and this essentially makes the system *wireless information and power transfer*. Furthermore, a multi-band (three frequencies or more) system can have the capability to allow both power transfer (one band for power delivery) and duplex information exchange (by dedicating separate bands for uplink and downlink transmissions) between Tx and Rx. In essence, this is also called the *SWIPT* system.

The DB WPT systems, which are used in a wide range of bioengineering, have become remarkably popular in recent decades; however, despite significant developments, these systems have numerous constraints. The first SGP-type DB WPT was achieved using the cascaded technique, particularly, a circular slot was cascaded twice resulting in a dual-operational resonator [43]. Subsequently, the realized system, working at 300 MHz and 700 MHz, exhibited the respective PTE of 71% and 72%. Furthermore, the majority of reported DB WPTs are designed to work at impractical frequency bands and possess large resonator areas [43, 51]. The other developed DB SGP-type WPT systems operate at ISM bands; however, these WPTs demonstrated limited PTD of 3.5 mm [49] and only 58% of achieved PTE [73].

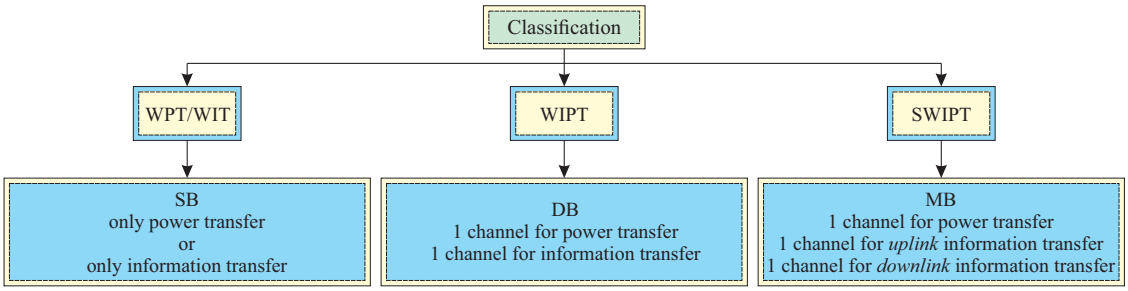

Figure 5.1. Depiction of the generic systems classification.

A review of the available literature on SGP-based WPTs indicates that the current research focuses on the MB WPT systems used in biomedicine. In particular, they can help perform continuous human health monitoring through concurrent power and data transfer. In fact, the practical implementation of these systems necessitates high data rates that are completely application-dependent and can reach 100 Mbps [103]. For instance, the brain-machine devices and capsule-type endoscopes mandate $1-10$ Mbps whereas the ocular implants demand 40 Mbps [77]. Furthermore, within the idea of electronic health, WBAN can be regarded as a backbone for the advanced healthcare infrastructure [104, 105]. Because of the numerous WBAN features and functionalities, the energy efficiency of each independent end module is used to assess its quality. Initially, the battery lifetime-related constraints of utilized sensors in WBAN were solved by employing the WPT system. Initially, SB WPTs were used to overcome the challenges of WBAN devices related to their embedded battery lifetime [106]; however, recent decades have witnessed that SWIPT can also be greatly useful to this field.

Metasurfaces are also extremely helpful in addressing some challenges that exist in the WBAN infrastructure. In this instance, it is worth mentioning that MSs are artificially engineered structures that are not found in nature. Recently, because of their property to describe distinct EM responses as coding elements, digital MSs have shown promise in several application areas [107]. Within the realm of coded MSs, the EM wave control is accomplished through the use of different binary coding techniques with one, two, three, and more bits. As a concept, MSs can ensure the change in the amplitude and phase of a reflected wave at a particular frequency. For example, it is presumed that the respective phase shifts are 180° and 90° when one- and two-bit coding methods are utilized. Consequently, designed MS can demonstrate the capability of beam scanning, beamforming, multi-beam generation, *etc*. It is apparent that these MS properties can be attractive to a wide range of applications including but not limited to holography, WPT, SWIPT, WBAN, different imaging methods, and cloaking systems [108].

5.2 Motivation

By nature, the use of conventional coil-type structures in the design of MB WPTs is challenging because they provide a limited narrow band [109]. In turn, it is directly relevant to the WPT system's achievable data rate, *i.e.*, greater bandwidth equals higher throughput. It is worth noting, in this context, that the SGP technique is capable of catering to the required bandwidth. As a result, there is a need for the implementation of high-performance MB WPTs with increased bandwidth at communication bands. This eventually contributes to the overall WPT domain toward reaching new heights and will be extremely beneficial to a variety of WBAN applications. Furthermore, only a few articles have recently been reported that attempt to use MSs effectively to facilitate WBAN needs [104, 105]. Therefore, another necessity is the development of a framework that aids in the incorporation of MS antennas and SWIPT to advance WBANs.

Keeping the preceding in mind, the primary goal of this chapter is threefold: i) to design high-performance DB SGP-based WPT that works at practical ISM bands; ii) to implement an MB SGP-type WPT system where one power is employed for power transfer whereas two other separate bands are dedicated for the full-duplex data transfer; iii) to develop a novel digital MS reflector that can address some of the constraints associated with the SWIPT-enabled WBAN infrastructure.

5.3 Contribution of the Chapter

The main contributions of this chapter are as follows:

- Performance-enhanced DB WPT, operating at ISM frequencies of 433 MHz and 900 MHz, has been realized. The resonator compactness was achieved through the use of an effective SGP technique which resulted in a small 18×18 mm^2 circuit area. Furthermore, the obtained experimental results demonstrated PTE 71% and 81% at two respective working bands.

- To the authors' best knowledge, ultra-compact tri-band WPT employing a cascade of double-elliptic slot-based resonators has been reported for the first time. Furthermore, during the TB WPT system development, the communication aspects are given full consideration. Moreover, realized TB WPT has the potential of supporting practical applications requiring low and high data rates.

- The effective integration of the coded MS structure and SWIPT system, for two specific practical WBAN scenarios, has been investigated. As a consequence, it has been demonstrated that digital MS features such as a multi-beam creation and beam focusing can be extremely useful for emerging WBAN applications.

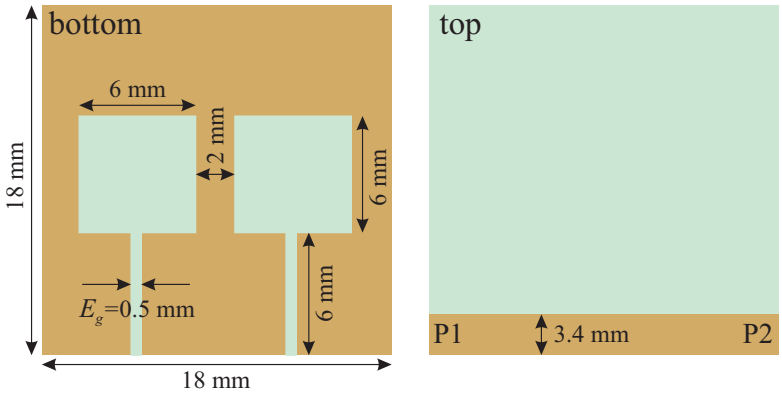

Figure 5.2. The proposed DB resonator.

5.4 Dual-band SGP-type WPT System

5.4.1 DB WPT System Design

5.4.1.1 DB Resonator

Two distinct simultaneous resonances, in general, necessitate the development of two oscillating circuits. Alternatively, it can also be accomplished by cascading and combining two separate SGP-type resonators with different resonant behaviors into one. Therefore, the SGP-based DB resonator using cascades of the square-shaped slots was proposed as depicted in Fig. 5.2. Two C_e capacitors, with appropriate values, were incorporated to attain the resonances at 433 MHz and 900 MHz. It is pertinent to note that the performed EM simulations are carried out using CST. Furthermore, the two square slots were etched on the circuit's ground plane and aided in the creation of two independent current distribution loops. The latter can be observed from Fig. 5.3 which depicts the current flow path of a ground plane. Besides, it reveals that the most current density is concentrated around two square slots and behaves differently at two distinct frequency bands.

EC, discussed in Chapter 3 (Fig. 3.9), was developed considering $n = 2$ for the verification of EM simulated results. Here, the equivalent C and L values of the designed DB resonator can be determined utilizing (3.12) and (3.13), respectively. Furthermore, Keysight ADS was employed to construct the effective EC of the SGP-type DB resonator. Following that, the relevant comparison of two different simulations is presented in Fig. 5.4 which displays a good agreement. In particular, it shows two clear resonances at the desired frequencies of 433 MHz and 900 MHz for both compared results. The modeling verification through EC gives the confidence to use the developed DB resonator in the NF WPT system design which is described in the next subsection.

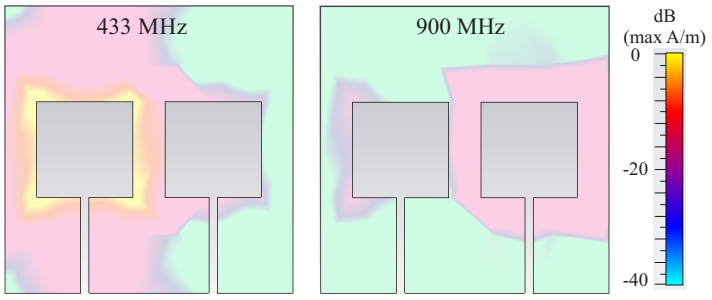

Figure 5.3. Surface current distribution of the DB resonator.

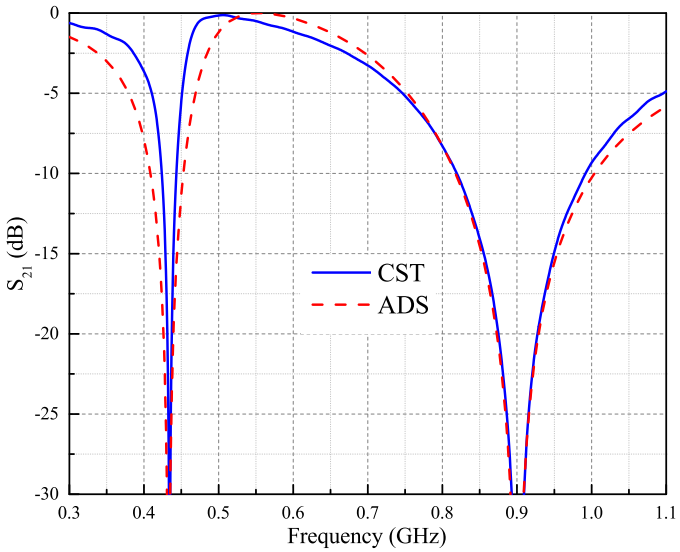

Figure 5.4. DB resonator results: S_{21} vs f_0.

5.4.1.2 DB WPT System

This section presents the development of a DB WPT system using the designed DB resonators. To accomplish this, two identical resonators must be separated by a certain distance while remaining coupled. This leads to the creation of M and k between the coupled resonators whose values can be defined using (4.8) and (4.5), respectively. Furthermore, the determination of all required element values enables the building of the SGP-type DB WPT system. Once again, effective EC of SGP-based DB WPT is similar to the given in Chapter 3 (Fig. 3.9) taking into account that $n = 2$.

In turn, developed EC of DB WPT aids in achieving the required matching, *i.e.*, to match the resonator impedance to 50-Ω ports (P1 and P2). This can be realized by adding C_{st} to the circuit. To be more specific, its defined value is converted to ML with an open-end (*i.e.,* an open-stub acting as a capacitance) whose length can be computed using (4.12). Then, the open stub is added to the top side of a DB SGP-based resonator. In this case, it is worth mentioning that the location of both E_{g} (E_{g1} and E_{g2}) was slightly changed to keep the WPT operating frequencies at the initially selected bands without worsening the overall performance. Essentially, the matching takes place because C_1 and

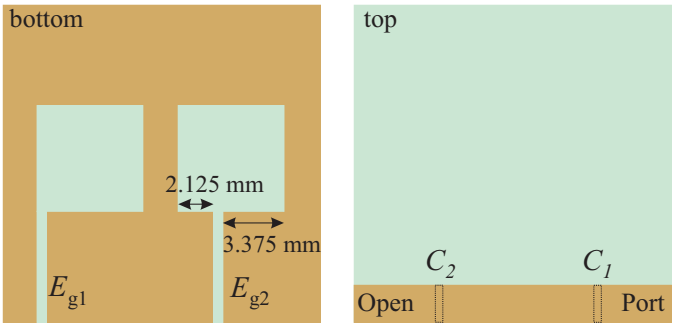

Figure 5.5. Developed DB WPT: the modified resonator.

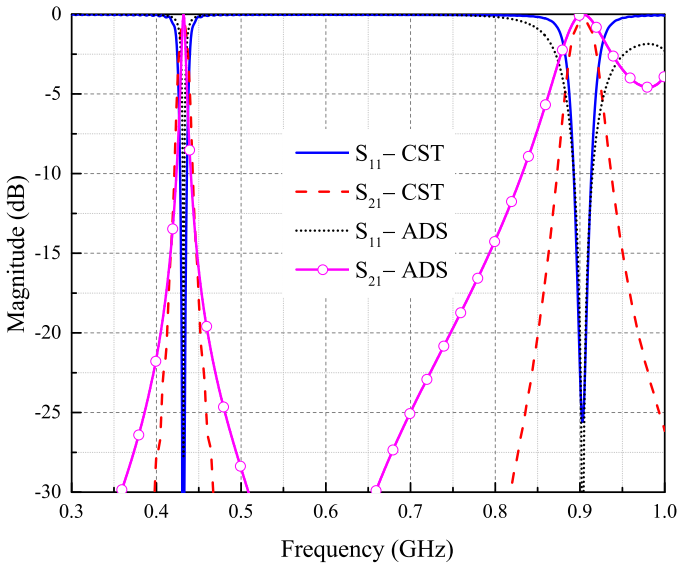

Figure 5.6. Simulation results of DB WPT: S-parameters vs frequency.

C_2 generate resonances by removing the impact of L_1 and L_2 at 433 MHz and 900 MHz, respectively. In addition, the modified SGP-based resonator used for the optimal DB WPT implementation is given in Fig. 5.5.

The results of EM and EC simulations are given Fig. 5.6 in terms of S_{11} and S_{21}, when PTD is 15 mm. The respective achieved S_{11} of -33.2 dB and -25 dB at the operating frequencies of 433 MHz and 900 MHz exhibit the perfect impedance matching. Furthermore, the S_{21} values of -0.43 dB and -0.51 dB confirm the following: $\mathrm{PTE}_{433} = 90\%$ and $\mathrm{PTE}_{900} = 88\%$. Moving forward, calculated PTE results can be used to define FoM of the designed DB WPT system. Finally, computed FoMs using (3.7) are as follows: $\mathrm{FoM}_{433} = 0.96$ and $\mathrm{PTE}_{900} = 0.84$.

5.4.1.3 Performed Experimental Measurements

For the sake of WPT design validation, two identical SGP-type resonators were fabricated using the Rogers' RO4350B three-layered substrate. The properties of the latter are as follows: $\varepsilon_{\mathrm{r}} = 3.48$, $h_{\mathrm{s}} = 1.524$ mm, and $h_{\mathrm{c}} = 0.035$ mm. Furthermore, the SMD-type

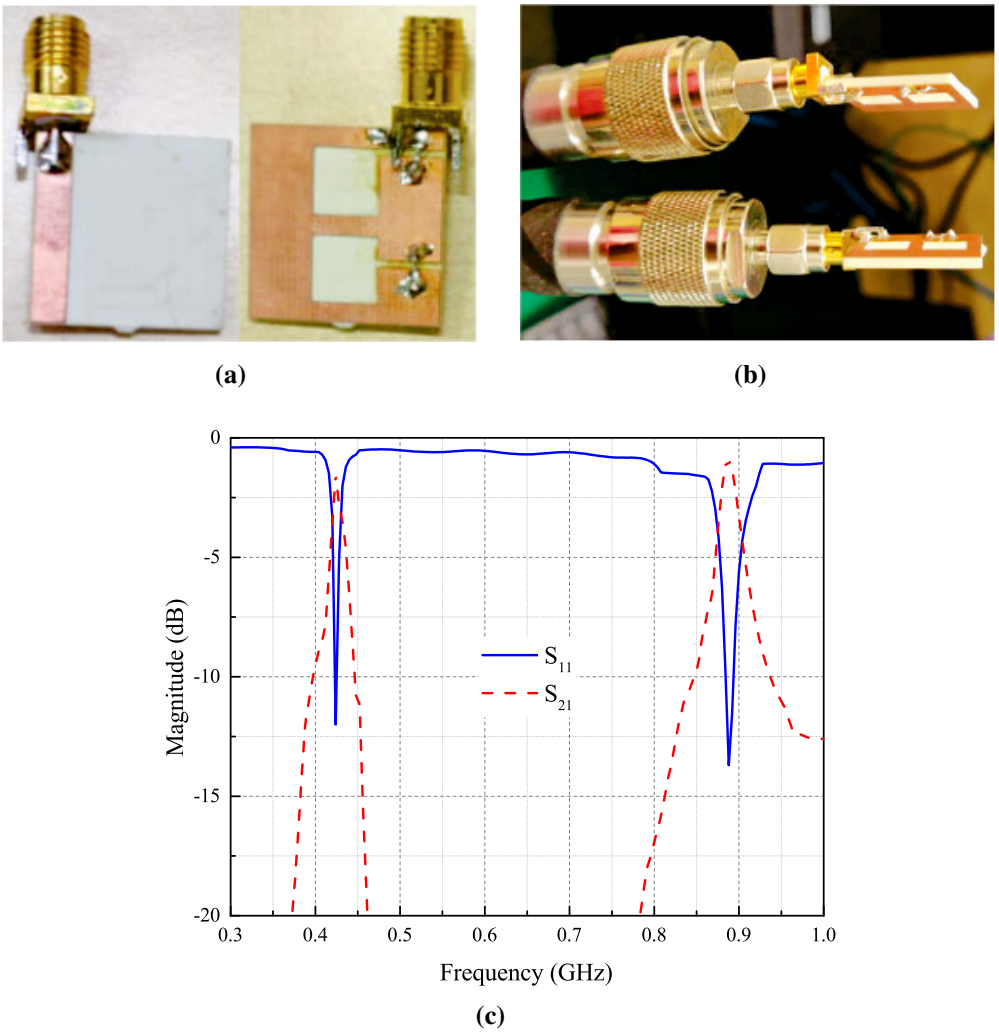

Figure 5.7. SGP-based DB WPT system implementation: (a) fabricated resonators; (b) coupled Tx and Rx; (c) measured results.

capacitors with 11 pF and 2.2 pF were incorporated to attain the resonance at 433 MHz and 900 MHz, respectively. Then, the SMA connectors were soldered to each resonator assisting to connect them to VNA, subsequently, the S-parameters measurement becomes feasible. The fabricated SGP-based DB resonators are given in Fig. 5.7a whereas Fig. 5.7b depicts coupled Tx and Rx at 15 mm. Consequently, the obtained measured S-parameters are presented in Fig. 5.7c which depicts the DB behavior of the realized WPT system. Calculated PTE of DB WPT, using measured S_{11} and S_{21}, were equal to 71% and 81% at 433 MHz and 900 MHz, accordingly. These achieved results can be regarded as an excellent output and, thereby, tend to extremely advance the DB SGP-based WPT system domain.

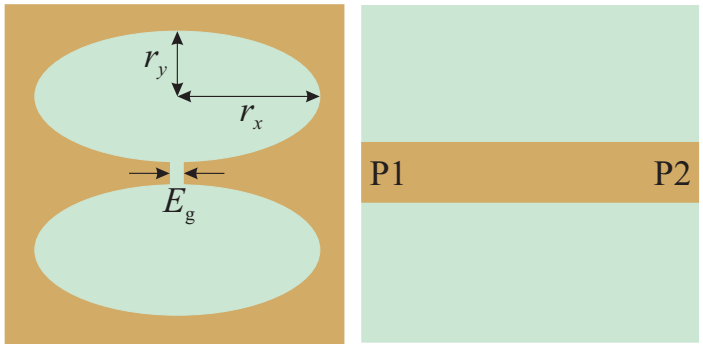

Figure 5.8. The proposed double-elliptic slot-type resonator structure: (a) bottom; (b) top.

5.5 Compact SGP-based SWIPT System

5.5.1 TB SGP-type Resonator Design

It is worth mentioning that the use of WPTs for low-power applications led to advancements in overall SGP-based WPT systems. In particular, the main focus was on the size of the WPT circuit and its performance. On the other hand, MB WPTs were also on demand enabling facilitating the concurrent duplex power and data transfer. Therefore, to fulfill this need, a TB SGP-type WPT system was proposed. Furthermore, designed WPT used 300 MHz for power transfer whereas 500 MHz and 900 MHz were employed for the *uplink* and *downlink* data transfer, respectively [43, 110, 111].

5.5.1.1 Proposed Slot Analysis

A compact SGP-based resonator, with the 13×13 mm^2 circuit area, was proposed which utilizes the double-elliptic slot, as depicted in Fig. 5.8. As was already mentioned in the above sections, using ground planes with different slots results in varied band-stop effects. For example, in the proposed resonating structure, a capacitance (C_g) is generated by the small gap (E_g) which connects two ellipses. Furthermore, the effective combination of the created capacitance and the circuit's inductance causes resonant behavior. In particular, the proposed structure resulted in the resonance of 6.45 GHz; however, the occurred resonant frequency can be adjusted to the required one by inserting C_e (*i.e.*, an additional capacitor). For the sake of completeness, simulated S_{21} are presented in Fig. 5.9 that effectively illustrated this. As a result, the expression, given by $C = C_g + C_e$, can describe the enlarged total resonator capacitance.

On the other hand, a large bandwidth at the operating frequencies is needed to fulfill the needs of high data rate applications. Therefore, the effect of the introduced slot's

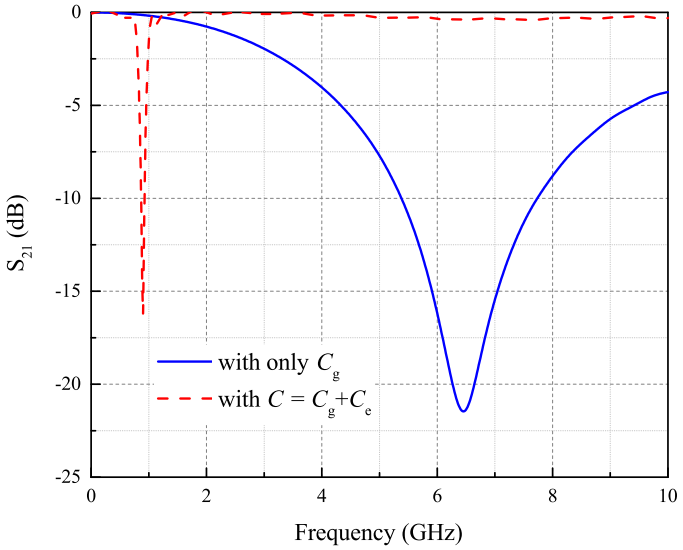

Figure 5.9. EM Simulation results of the proposed resonator.

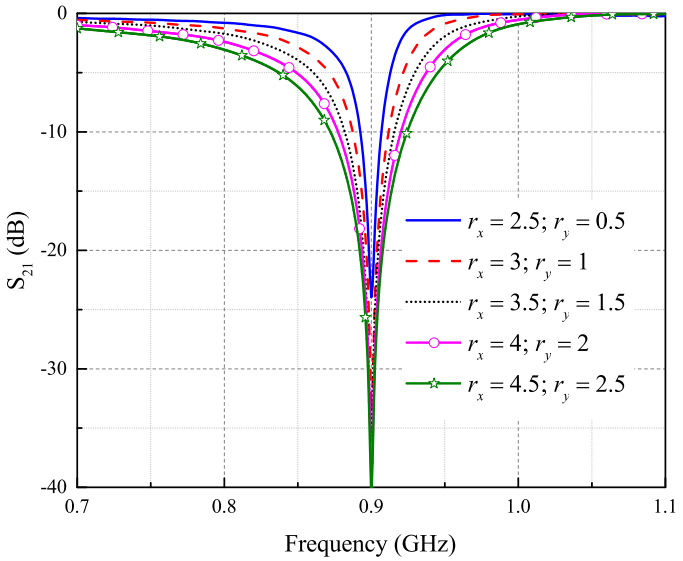

Figure 5.10. Elliptic slot size variation (r_x and r_y are in mm): S_{21} vs f_0.

key parametric variations on the achievable bandwidth was investigated. To be more specific, the radii of r_x and r_y were modified during this analysis whose obtained results are provided in Fig. 5.10. Subsequently, it was explored that the maximum bandwidth of the SGP-type resonator corresponds to the elliptic slot with $r_x = 4.5$ mm and $r_y = 2.5$ mm. Therefore, the double-elliptic slot, employing optimal r_x and r_y, was chosen for the further TB SGP-based resonator design.

5.5.1.2 TB Resonator

This section presents the development of a TB SGP-based resonator. It is pertinent to mention, in this context, that the cascading technique was used for the creation of the

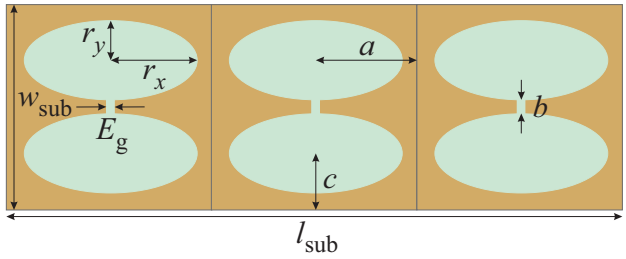

(a)

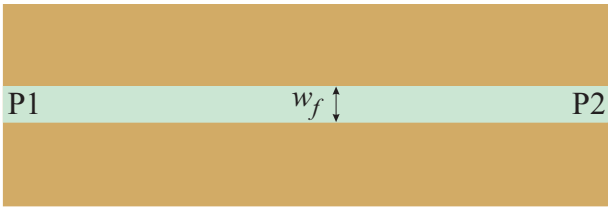

(b)

Figure 5.11. The designed TB resonator with the optimized parameters: (a) bottom; (b) top.

Table 5.1. Used parameters of the TB resonator.

Parameters	w_{sub}	l_{sub}	w_f	E_{g}	r_x	r_y	a	b	c
Dimensions (mm)	13	39	3.4	0.5	4.5	2	6.5	2	6.5

TB resonator. The mentioned approach allows for designing a resonator that can operate within several desired frequency bands. Keeping this advantage in the perspective, the already designed SB resonator was cascaded three times to achieve the TB resonator demonstrating the resonances at 300 MHz, 500 MHz, and 900 MHz. Subsequently, the length (l_{sub}) of the newly developed resonator was modified to 39 mm whereas its width (w_{sub}) remains unchanged (*i.e.*, 13 mm). The TB resonator, depicted in Fig. 5.11, is a three-layered structure and was developed on the Rogers' RO4350B substrate with the following parameters: $h_{\text{s}} = 1.524$ mm, $h_{\text{c}} = 0.035$ mm, and $\varepsilon_{\text{r}} = 3.66$. It is worth noting that the proposed double-elliptic slot was etched on the ground plane (bottom side). Furthermore, ML with the width (w_f) of 3.4 mm is located on the substrate's top-side and connects the ports P1 and P2. In addition, Table 5.1 presents the key parameters of the developed TB SGP-type resonator with optimized dimensions.

It has been demonstrated that the developed SGP-based WPT systems can be verified by their respective ECs. As a consequence, effective EC was constructed by aptly using the generic WPT EC, given in Chapter 3, and taking into account that $n \in \{1, 2, 3\}$. Moreover, developed EC of the designed TB SGP-based resonator is illustrated in Fig. 5.12. It is worthwhile to note that the appropriate combination of L and C helps achieve the resonance at the selected frequency bands whose effective values can be calculated utilizing (3.12) and (3.13). In this case, the respective computed values of are $L_1 = 5.662$

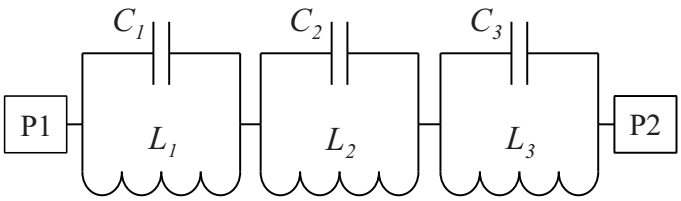

Figure 5.12. Constructed EC of the SGP-based TB resonator.

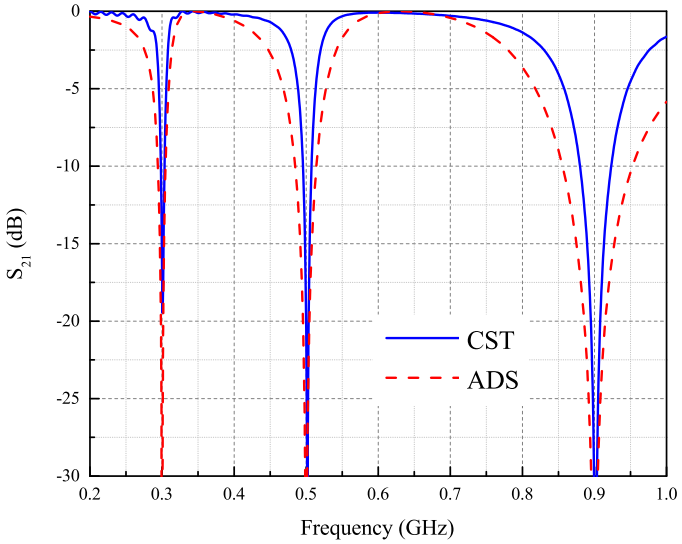

Figure 5.13. Obtained simulation results of the TB resonator.

nH, $L_2 = 5.66$ nH, and $L_3 = 5.717$ nH at the resonances of 300 MHz, 500 MHz, and 900 MHz. Subsequently, these defined L values enable the determination of required C_e for achieving resonances at the selected frequencies. Furthermore, the TB SGP-based resonator model was developed employing CST whilst its respective EC was constructed using ADS. Finally, the obtained EM simulation and EC results are presented in Fig. 5.13 which demonstrates a good match between them. As a consequence, the designed resonator can be used in the TB WPT development, which is described in more detail in the following sub-section.

5.5.2 SWIPT System Development

The design of the SGP-based SWIPT system, which appropriately utilizes the developed TB resonators, is discussed in this section. As a general principle, the WPT system implementation necessitates the followings: i) two coupled resonators oscillating at the same resonant frequency; ii) they must maintain a perfect alignment to ensure high-performance WPT. In addition, it is considered that P1 excites Tx whereas the port of Rx (P2) is connected to a load.

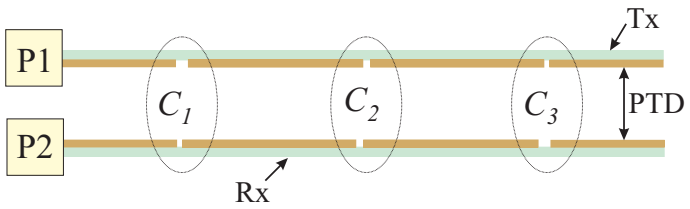

Figure 5.14. Illustration of the coupled TB resonators.

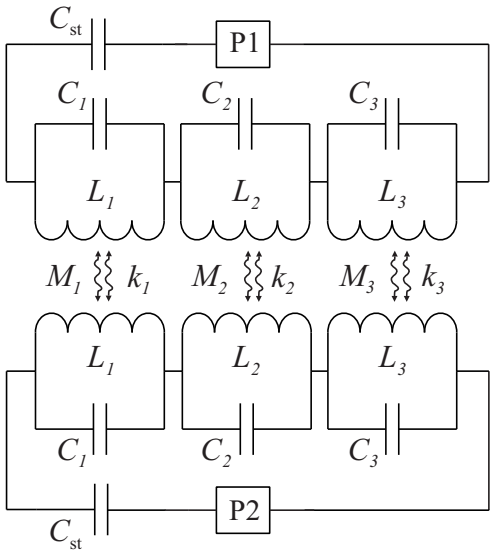

Figure 5.15. EC of the SGP-type TB WPT system.

5.5.2.1 WPT System Realization

In general, the WPT system development starts from coupling two designed same resonators at certain proximity. In this instance, it should be noted that identical C_e of Tx and Rx are placed opposite to each other, as shown in Fig. 5.14. Furthermore, the separation distance between two coupled resonators needs to be precisely regulated to keep them under the required coupling conditions. Moreover, the performed coupling allows for defining the key parameters M and k using the appropriate expressions given in Chapter 4. In turn, their defined values are extremely useful in the EC construction of the TB SGP-based WPT system.

5.5.2.2 EC Development for the TB WPT System

Fig. 5.15 depicts EC of the TB WPT system that is constructed using the developed TB resonator's EC. In this case, C_{st} is connected to the circuit that helps match the resonator impedance to the 50-Ω port. Furthermore, the former can be synthesized as open-stub ML whose parameters are defined using (4.12). In particular, when its length (*i.e.*, l_{st}) is determined for all three operating frequencies, it is necessary to place them on the top side of the resonator. In essence, it helps in canceling L_1 by C_1 at 300 MHz, L_2 by C_2 at 500

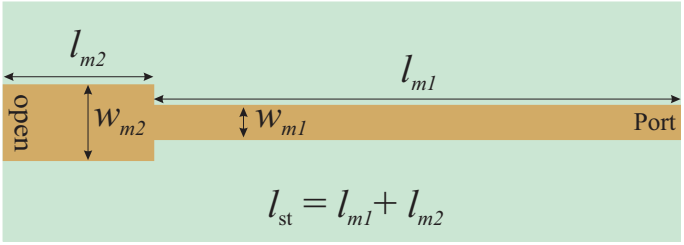

Figure 5.16. The top side of the modified TB resonator.

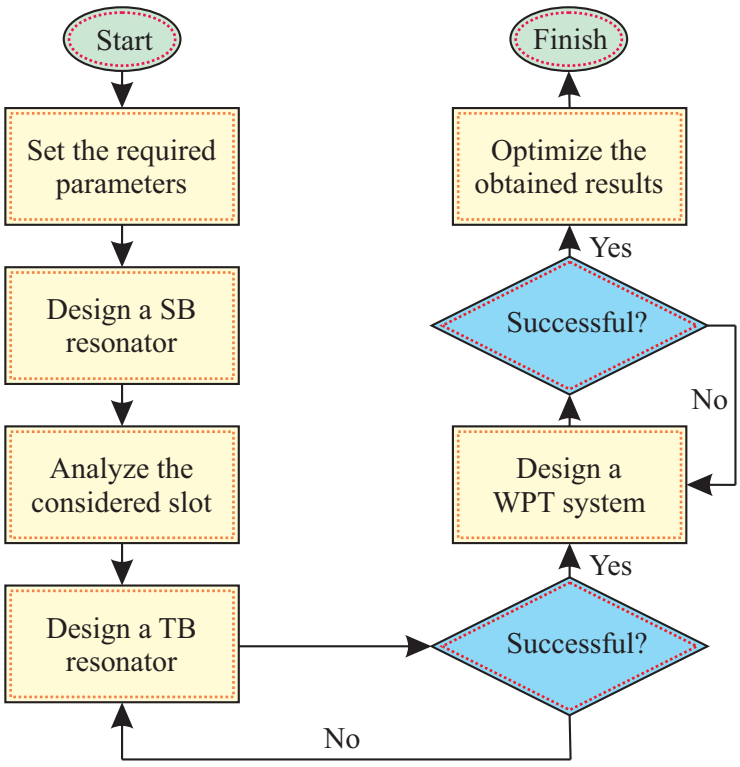

Figure 5.17. TB SGP-based WPT system design methodology.

MHz, and L_3 by C_3 at 900 MHz. In this regard, it is worth mentioning that the sum of l_{m1} and l_{m2} defines the total l_{st} length (Fig. 5.16). Besides, taking into account the finite size of the resonator, the width (w_{m2}) of the inserted stub was slightly altered to enable good matching at the utilized frequency bands. In addition , the final optimized dimensions of added ML that facilitate a perfect impedance matching for all three frequencies are as follows: $l_{m1} = 32.75$ mm, $l_{m2} = 6.25$ mm, $w_{m1} = 3.4$ mm, and $w_{m2} = 4.9$ mm.

5.5.2.3 Systematic Implementation Steps of the SWIPT System

The flow chart in Fig. 5.17 shows a design methodology for the developed SGP-based SWIPT system. Particularly, the key SWIPT design steps are outlined below:

- In the beginning, define the crucial SWIPT parameters, namely, a resonator area, required PTD, operating frequencies, a substrate type, *etc*.

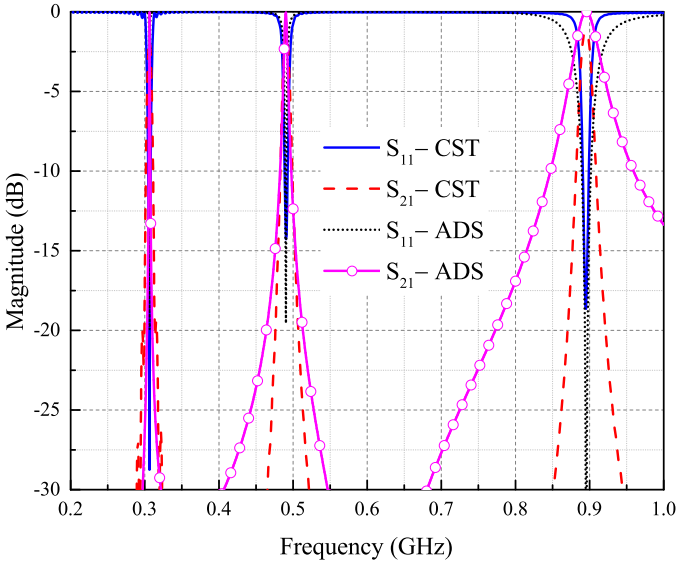

Figure 5.18. TB WPT simulation results.

- After defining the design specifications, develop a double-elliptic slot-based SB resonator. Then, thoroughly investigate the considered slot to obtain the best outcome. Afterward, calculate the required values of C_{e} that aid in the needed resonances at the selected working frequencies.
- Next, follow the cascading approach to obtain a resonator with MB behavior. Furthermore, construct its EC for design verification purposes.
- Perform the coupling of two identical SGP-based MB resonators: i) determine PTD under the critically coupled conditions; ii) define the values of M_n and k_n.
- Then, construct EC of the TB WPT system: calculate required C_{st} and convert it into open-stub ML to perform the impedance matching.
- Finally, carry out the optimization to improve the achieved EM simulation results.

5.5.3 Obtained Results and Discussions

This subsection presents the obtained simulation and experimental results along with their appropriate discussions. The required capacitors to achieve the resonance at the selected frequencies are as follows: $C_{\mathrm{e1}} = 47$ pF, $C_{\mathrm{e2}} = 18$ pF, and $C_{\mathrm{e3}} = 5.3$ pF. Furthermore, the comparison of EM and EC simulated results is depicted in Fig. 5.18. It is worth mentioning that EC was developed to optimize the overall WPT system, and obtaining the perfect match between EM and EC results supports this approach. It is apparent that there are three distinct resonances that occurred at the selected working frequencies of

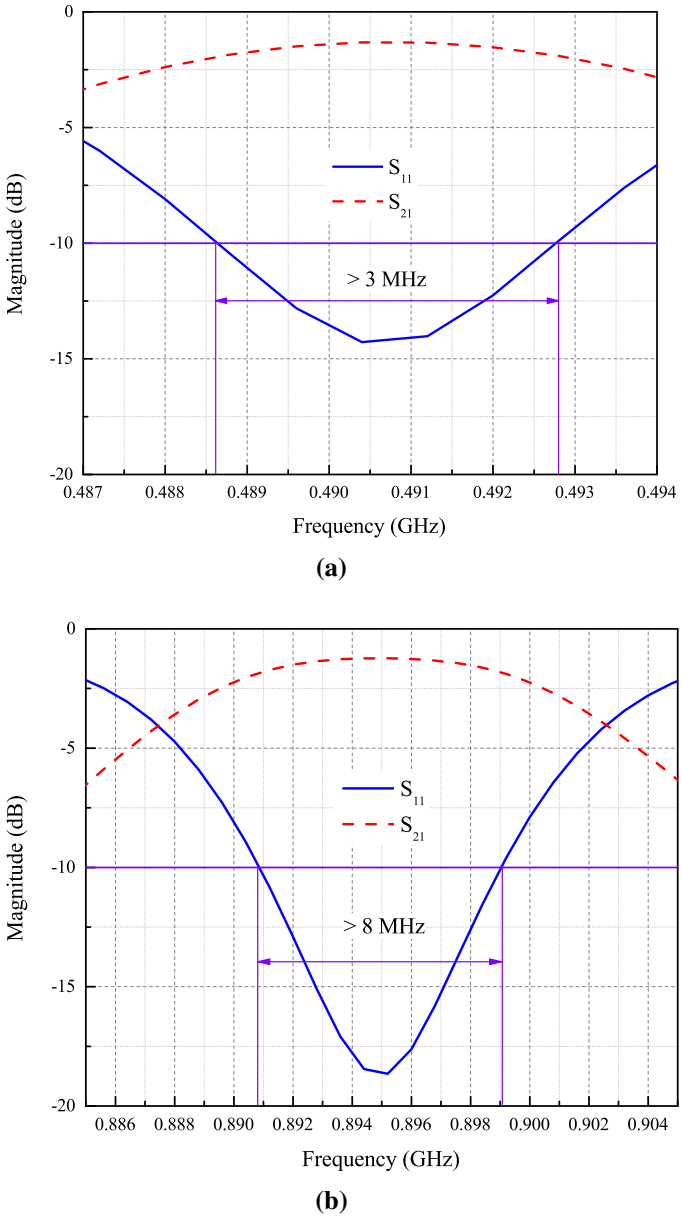

Figure 5.19. Obtained 3 MHz bandwidth: (a) 500 MHz; (b) 900 MHz.

300 MHz, 500 MHz, and 900 MHz. Moreover, the results reveal that achieved S_{21} at those frequencies are -1.81 dB, -1.31 dB, and -1.23 dB, when PTD $= 10$ mm.

In fact, none of the previously reported DB or MB SGP-type WPT systems took the achievable data rate, at communication bands, into account. Therefore, the effect of slot size on the bandwidth was examined. Furthermore, it is pertinent to note that the 3 MHz bandwidth was achieved at the bands, dedicated for data transfer, by optimizing the considered design as shown in Fig. 5.19. It should be noted, in this regard, that a wide bandwidth is required to meet the needs of high-speed applications [77], which may result in the Q reduction. The 3rd Generation Partnership Project (3GPP) Long-Term Evolution (LTE) document allows the use of a 3 MHz channel bandwidth composed of 15 resource

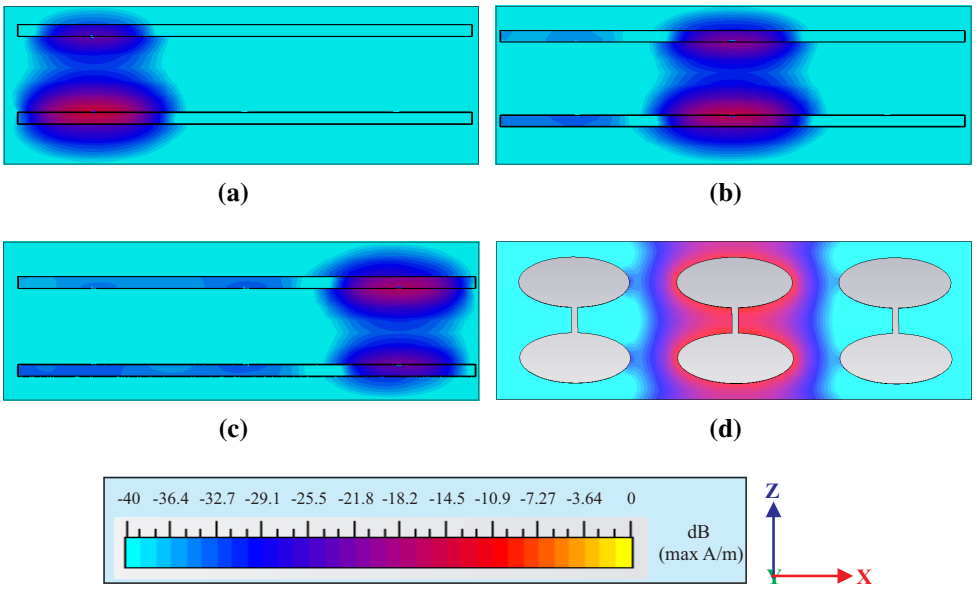

Figure 5.20. Magnetic field distribution: (a) 300 MHz; (b) 500 MHz; (c) 900 MHz; (d) surface current distribution at 500 MHz.

blocks (RBs) [112]. As a result, the designed SGP-based WPT system can support low and high data rates by assigning a different amount of RBs. Allocating more than 15 RBs, on the other hand, necessitates a broader channel capacity, such as 10 MHz, 15 MHz, and 20 MHz. Therefore, it is worthwhile to note that the developed TB WPT system cannot support applications requiring more than 15 RBs. The values of S_{11} for three operating frequencies are below -10 dB, indicating a really good impedance matching. The S_{11} and S_{21} values were then employed to define PTE which led to the following results: $PTE_{300} = 66\%$, $PTE_{500} = 74\%$, and $PTE_{900} = 77\%$. Finally, calculated FoMs of designed SWIPT from the simulation results were 0.5, 0.57, and 0.59 at 300 MHz, 500 MHz, and 900 MHz, respectively.

It has been extensively reported in several studies that the PTD change has a significant impact on the developed WPT system performance. Therefore, a comprehensive analysis is performed in a simulation environment to comprehend and evaluate the effectiveness of designed TB WPT. It was found out that the designed system exhibits its superior result at 10 mm. Furthermore, the coupling of two SGP-based TB resonators is presented in Fig. 5.20. As can be seen, the designed WPT system achieves a good coupling at $PTD = 10$ mm for the frequencies of 300 MHz, 500 MHz, and 900 MHz. Moreover, the impact of the potential vertical and horizontal displacement was studied to assess the WPT performance before the final fabrication. In these investigations, it was hypothesized that one resonator is fixed while the other one is relocated parallel to the vertical or horizontal side. The obtained results are shown in Fig. 5.21, implying that PTE is more sensitive to vertical displacement. For instance, the 3 mm horizontal movement leads to about 10% efficiency

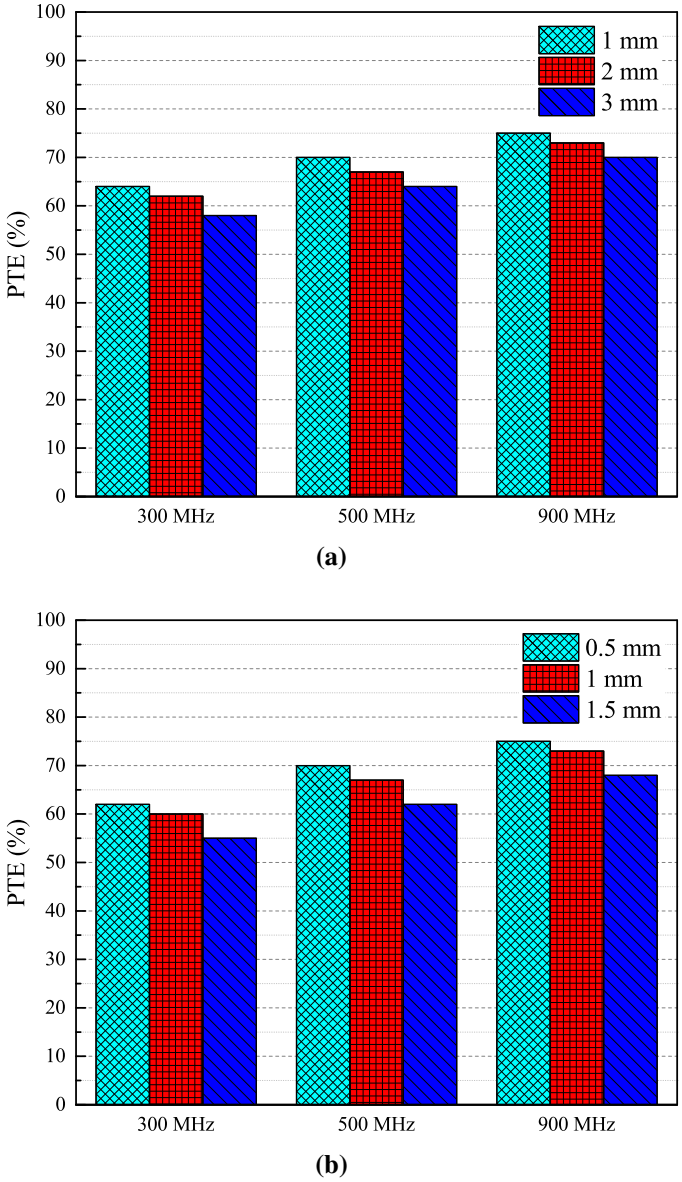

Figure 5.21. Misalignment study results: (a) horizontal; (b) vertical.

decrease whilst the same amount of the PTE drop corresponds to the vertical 1.5 mm shift. This phenomenon can be explained with the help of the current distribution on a ground plane as shown in Fig. 5.20d. It demonstrates that the majority of the current flowing between two ellipses is focused around the etched slot. Furthermore, it reveals that it possesses a bigger area in a horizontal direction. As a consequence, the developed WPT performance has worsened more in the appearance of vertical movement. Besides, it is pertinent to mention that both considered misalignment scenarios have a similar influence on PTE in the case of all three working frequencies. Additionally, it was explored that the lower frequencies are more sensitive to misalignment, in terms of PTE, as compared to the higher frequency bands.

A prototype, shown in Fig. 5.22, was developed on the selected material to validate the

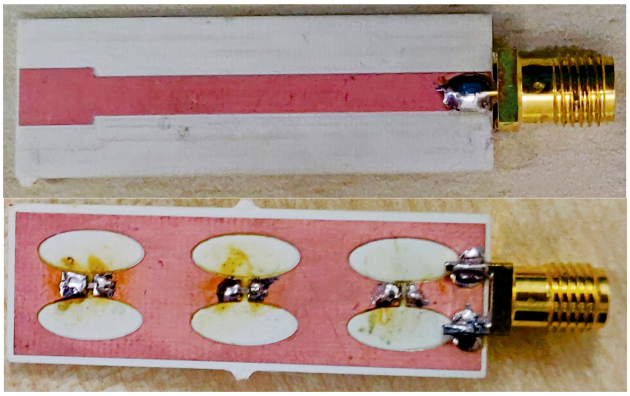

Figure 5.22. The prototype of the TB resonator (top and bottom).

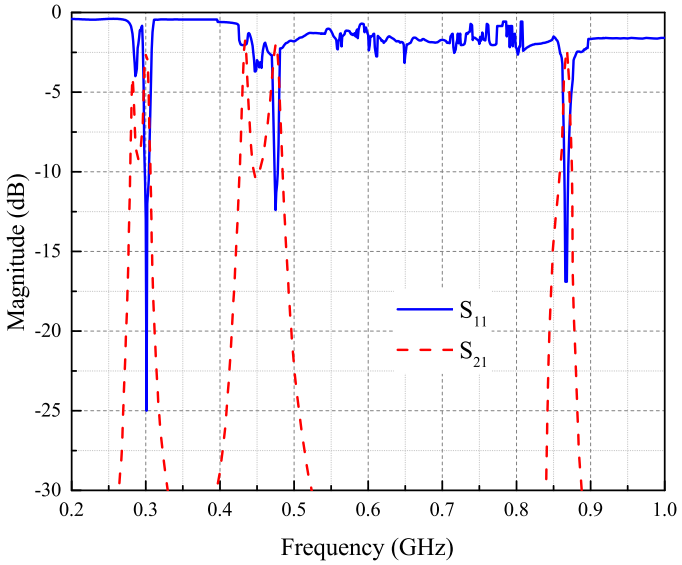

Figure 5.23. TB WPT experimental results.

presented TB WPT design. Furthermore, three SMD capacitors with the defined values were added to the resonator's ground plane. Two SMA connectors were soldered to each separate resonator that assists connect them to VNA. Then, the measured S-parameters, when two resonators are coupled at 10 mm, can be used to assess the developed WPT performance. It is imperative to note that the resonators should be perfectly aligned to avoid any displacement-related issues. The experimental results, given in Fig. 5.23, show good performance at the working frequency bands. Furthermore, one can notice a splitting phenomenon at 300 MHz and 500 MHz that can occur as a result of the sub-optimal experimental setup and potential human errors during the measurements. This can be mitigated by realizing a better matching; however, this requires ML optimization which, in turn, leads to the entire design modification. Computed PTE, using the measured data, is about 60% at 300 MHz while, for the communication bands of 500 MHz and 900 MHz, it is above 65%. Finally, it was shown that the power transfer occurs with 60% efficiency regardless of the splits at 300 MHz and 500 MHz, which was measured utilizing (3.4).

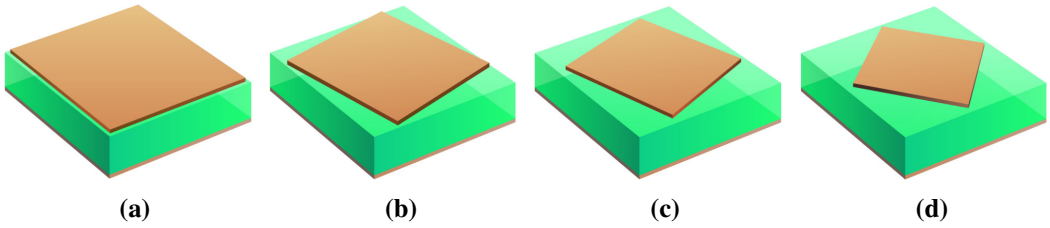

Figure 5.24. Designed different UCs to realize the required coding elements ($\Upsilon = 10$ mm): (a) UC I, '10', $\Psi = 9.6$ mm, $\xi = 0°$; (b) UC II, '01', $\Psi = 7.99$ mm, $\xi = 15°$; (c) UC III, '00', $\Psi = 7.41$ mm, $\xi = 30°$; (d) UC IV, '11', $\Psi = 6.29$ mm, $\xi = 45°$.

5.6 Digital Metasurface for WBAN Applications

5.6.1 Digital MS Modeling

Over the recent years, coded MS has greatly progressed owing to the EM wave control ability. The first step in incorporating coding and EM wave is to encode the wave phases of unit cells (UCs) utilizing '0' and '1'. As a result, MS in a variety of forms can be entirely converted into a digital sequence. In essence, it is important to note that the appropriate design of UCs is vital as they define the overall coded MS performance.

5.6.1.1 Unit Cell Design

The use of generalized Snell's law to manipulate the phase of EM waves has gained prominence. In general, the binary code elements '0' and '1'are used to characterize the EM phase responses that can be accomplished with the appropriate UCs configuration. To meet this requirement, four different UC structures, illustrated in Fig. 5.24, have been proposed. It is important to note that UCs have an area of $\Upsilon \times \Upsilon$ and are built on the Rogers RO3003 substrate. In particular, one layer of a dielectric material ($h_s = 1.52$ mm) and two layers of annealed copper ($h_c = 0.035$ mm) compose designed UC. Furthermore, the bottom side of a substrate is fully covered by copper which acts as a ground plane while square patches, with $\Psi \times \Psi$ area, are located on the top side. The patch size was adjusted to control the EM phase response at the desired operating frequency. In addition, UC types II, III, and IV were rotated by the ξ angle to achieve various phases.

In general, digital MS can assure the modification of the reflected wave's amplitude and phase in a certain frequency band. For example, it is envisaged that the phase difference is π when 1-bit coding is adopted while it becomes $\frac{\pi}{2}$ for the 2-bit configuration. The necessary $90°$ phase shift at the selected frequency was achieved by designing different UCs which can be seen from Fig. 5.25a. Particularly, the respective phase responses for separate 2-bit coding elements of '10', '01', '00', and '11' were obtained by

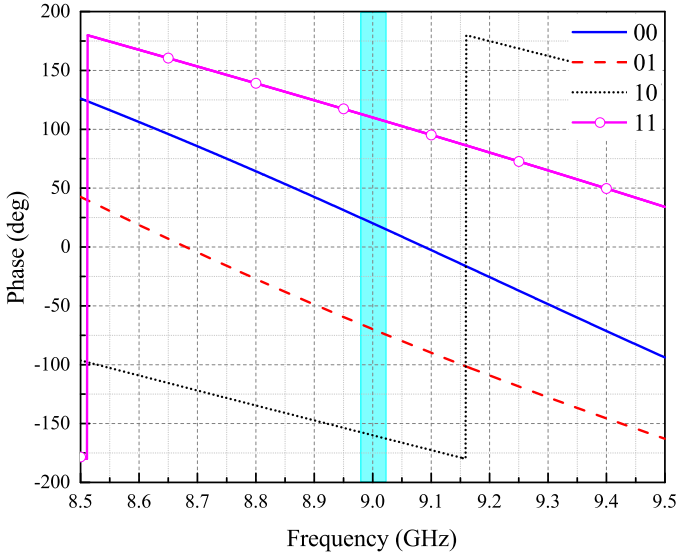

(a)

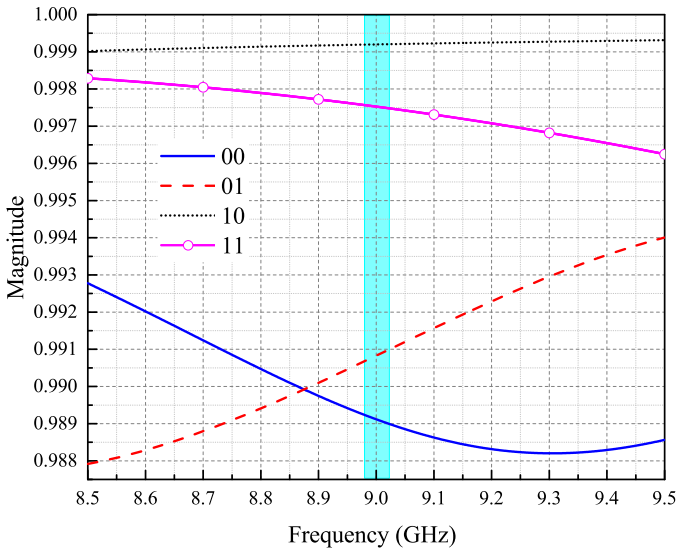

(b)

Figure 5.25. Obtained UC results: (a) phase; (b) amplitude.

designed I, II, III, and IV UC types. Furthermore, it should be noted that digital MS is designed to operate at 9 GHz whose phase responses at each coding element are as follows: '00'= 20.11°, '01'= −69.8°, '10'= −159.96°, and '11'= 110°. In addition, Fig. 5.25b presents the amplitudes for all states that confirm a good reflection with the minimum value of 0.989 corresponding to '00'.

5.6.1.2 Metasurface Development

Designed UCs can be aptly utilized to develop digital MS with various configurations and, subsequently, different behavior. For example, the generalized Snell's rule states that the employed coding pattern determines the scattered reflected EM wave from designed

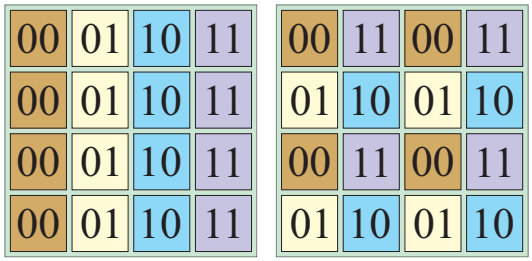

Figure 5.26. Coding configurations: (a) column-wise; (b) chessboard-like.

MS [107]. The generic coded MS pattern, using two distinct approaches, is illustrated in Fig. 5.26. In particular, the use of the column-wise pattern leads to an abnormal reflection whereas the chessboard-like configuration results in the multi-beam generation [107]. Finally, CST was used to perform EM simulations of designed digital MS under the assumption that the incident EM wave to MS is a plane wave.

It is apparent that the potential mutual coupling between neighboring UCs decreases the performance of developed coded MS. Therefore, array-type MS with the $K \times K$ size was formed, with separate array elements comprising of $H \times H$ UCs. As a result, $K \times H \times \Upsilon$ is employed to estimate the overall size of developed array-based digital MS. Furthermore, the generalized Snell's law describing the scattering pattern of MS is given in (5.1) [113]. Here, $\frac{\partial \phi}{\partial x}$ is the phase gradient between air and digital MS; λ stands for the wavelength; θ_i and θ_r represent the incident and reflected angles of the EM wave, accordingly. Furthermore, because of the 2-bit coding configuration, the periodicity of the gradient is expressed as $p = 4H\Upsilon$, therefore, $\frac{2\pi}{p}$ represents the phase gradient. In addition, considering the normal incident EM wave (*i.e.*, $\sin\theta_i = 0$), the reflected wave's direction angle can be defined employing (5.2) [107].

$$\sin(\theta_r) - \sin(\theta_i) = \frac{\lambda}{2\pi}\frac{\partial \phi}{\partial x}, \tag{5.1}$$

$$\theta_r = \begin{cases} \arcsin\left(\frac{\lambda}{4H\Upsilon}\right), & \text{if "colum-wise";} \\ \arcsin\left(\frac{\lambda}{2H\Upsilon}\right), & \text{if "chessboard-like".} \end{cases} \tag{5.2}$$

The reflected EM wave angle from MS is defined by the appropriate values of K, H, and Υ. Consequently, two-bit coded MS with $K = 4$ and $H = 3$ was generated to illustrate the beam steering and multi-beam generation phenomena. Following that, the reflected wave angles of developed digital MS were calculated using (5.2). To be more specific, it was identified that the incident angles are equal to 16.11° and 33.72° for the column-wise and chessboard-like coding configurations, respectively. Moreover, Fig.

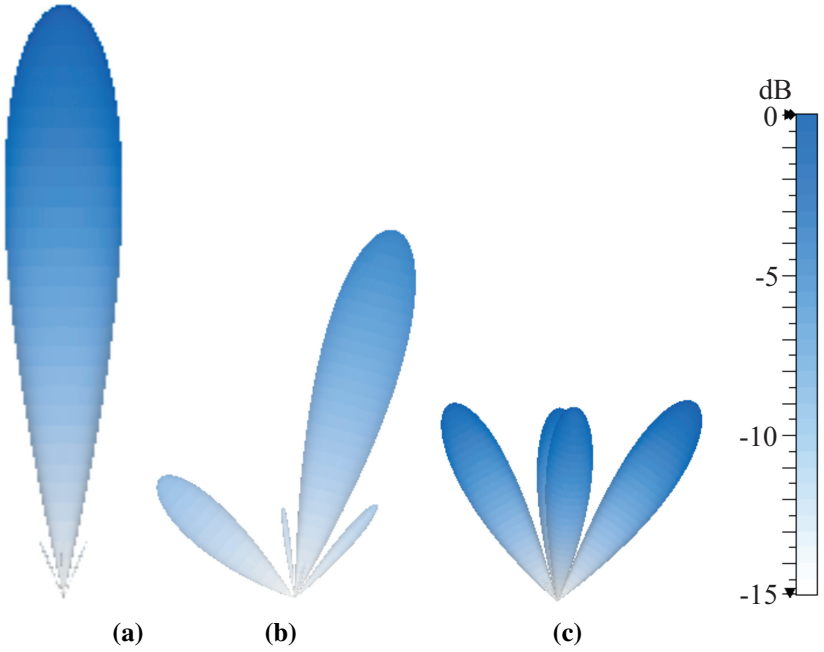

Figure 5.27. Radiation patterns: (a) copper plane; (b) column-wise; (c) chessboard-like.

5.27 presents a three-dimensional illustration of the reflected radiation pattern from full-wave EM simulations. The reflected wave angle is 0° when the top side of MS is coated by copper, as shown in Fig. 5.27a. Additionally, the beam steering is aptly shown in Fig. 5.27b whereas Fig. 5.27c exhibits the multi-beam generation capability of designed MS.

5.7 Considered WBAN Application Scenarios

The introduction of internet access via wireless systems has resulted in a new paradigm in several areas of human life. Over the last few years, there have also been huge advancements in the multitude of disruptive tools and technologies. One such innovation is considered SWIPT which has an ability to completely reshape the emerging WBAN applications. SWIPT (*i.e.*, MB WPTs) can support both power as well full-duplex data transfer between Tx and Rx by means of separately dedicated frequency bands. The reliable functionality and implementation of WBAN are primarily dependent on the communication systems, the foundation of which is SWIPT. Hence, the design and deployment of SWIPT systems may serve as a fillip, reigniting the generic concept of WBAN.

Fig. 5.28 depicts a conceptual representation of the envisaged WBAN application scenarios. It is assumed that a patient is equipped with in- and on-body sensors that detect, sample, and transmit essential information to a processing node. The received data then be processed further by the latter for health condition monitoring, diagnosis, and treatment. In this instance, it is pertinent to mention that IMDs are essentially the

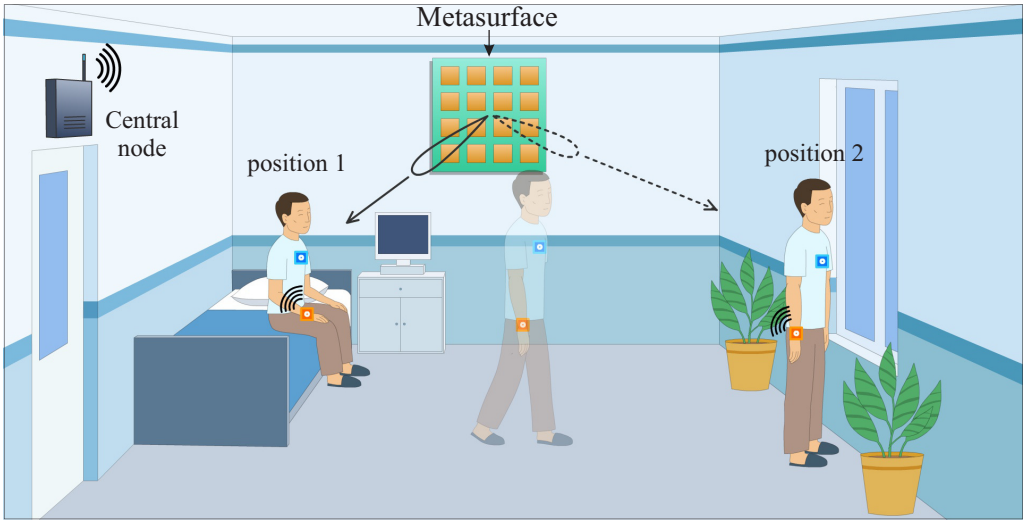

(a)

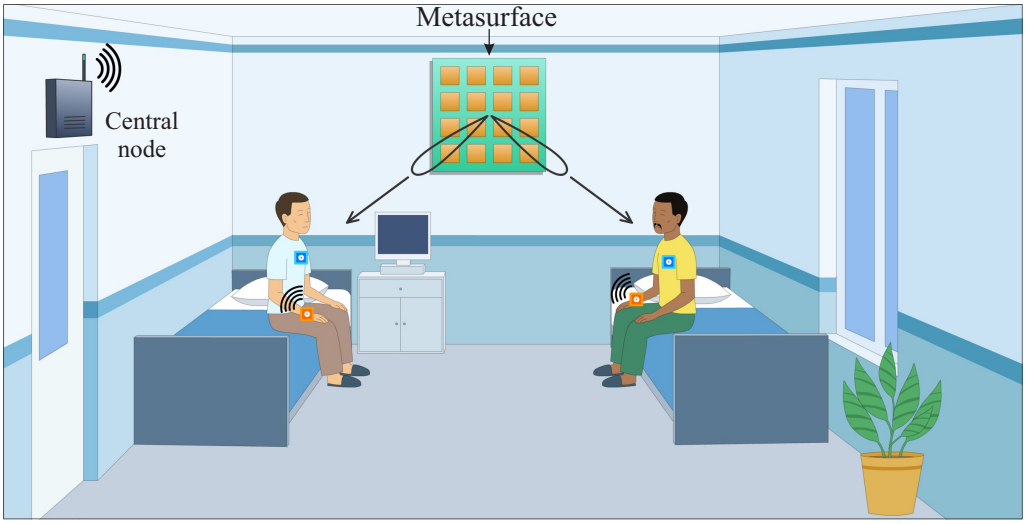

(b)

Figure 5.28. Considered application scenarios: (a) Scenario 1: one moving patient; (b) Scenario 2: concurrent two patients.

SWIPT systems whose embedded batteries can be continuously charged using the unique capabilities of designed digital MS such as a multi-beam generation and beam focusing. Furthermore, the re-configurable feature of developed MS is assumed to be able to follow the patient [107]. In particular, when the person is in the 1st position, the reflected radiation pattern of an EM wave will focus on that location. Moreover, if the patient's position is changed, the main beam's angle will be adjusted immediately. On the other hand, Scenario 2 is considered to take the advantage of the generated multi-beam feature. For instance, the developed multi-beams enable the simultaneous focusing of two or more patients (or devices).

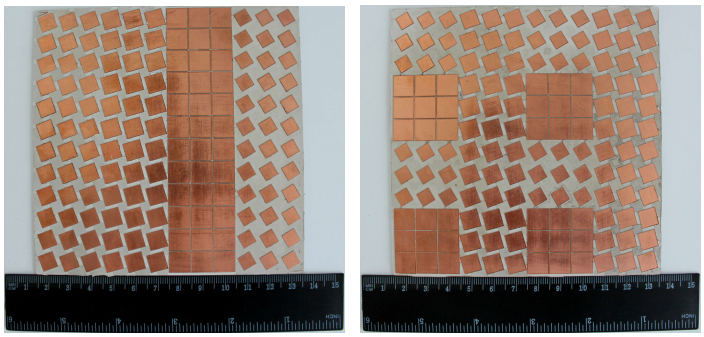

(a) **(b)**

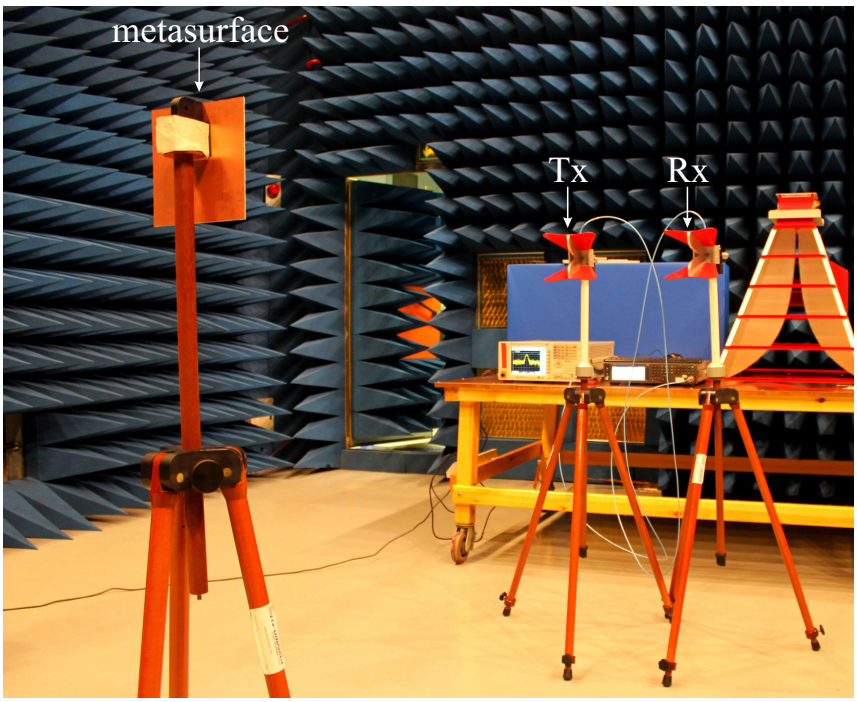

(c)

Figure 5.29. Experimental measurement and fabricated prototypes: (a) column-wise; (b) chessboard-like; (c) experimental setup.

5.7.1 Experimental Results and Discussions

Fig. 5.29 shows the manufactured working prototype of two-bit coding MSs and experimental setup. The UC-based digital MS reflector was built using Rogers RO3003 which has the next characteristics: $h_{\mathrm{s}} = 1.52$ mm; $h_{\mathrm{c}} = 0.035$ mm, $\varepsilon_{\mathrm{r}} = 3$; and loss tangent ($\delta$) of 0.001. Furthermore, developed coded MS is composed of a 4×4 array, each component of which includes constructed 3×3 UCs. Subsequently, this configuration led to a total MS antenna area of 120×120 mm^2. It is also important to note that all necessary measurements were taken in an anechoic chamber. Moreover, two double-ridged waveguide horn antennas (ETS-Lindgren, 3115-PA), acting as Tx and Rx, were used during the experimental tests. In addition, the Tx antenna was placed 2.2 m away from the MS

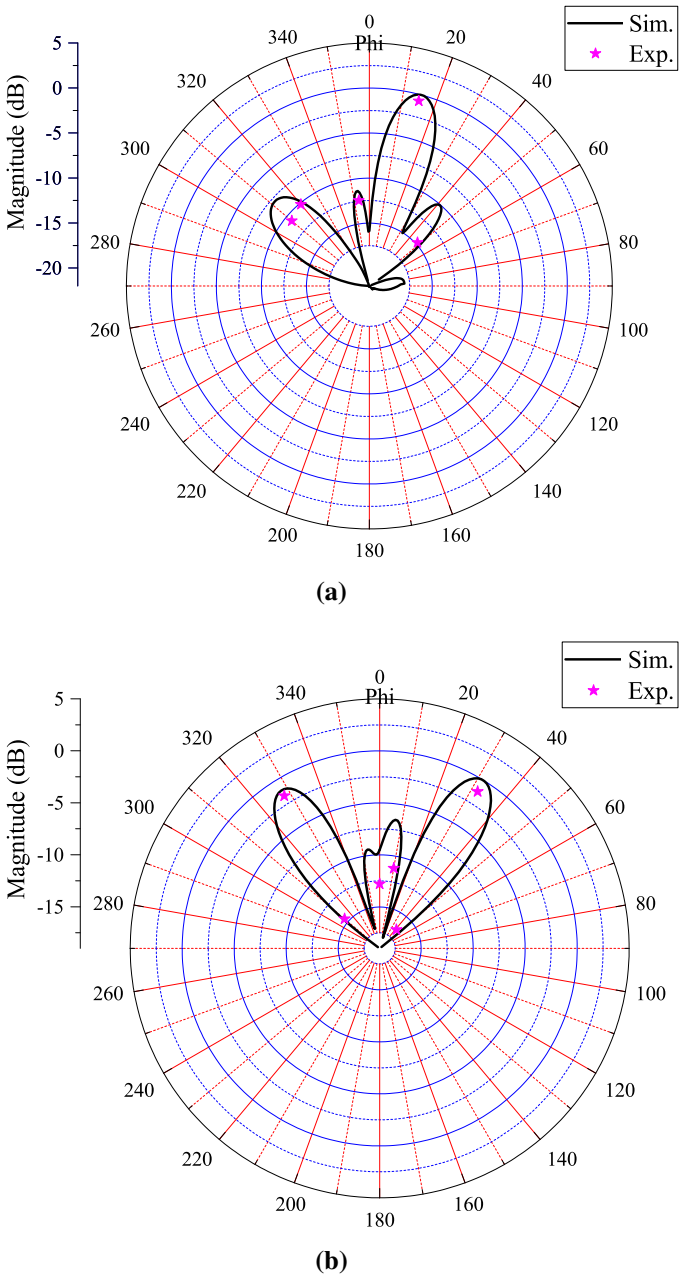

Figure 5.30. Beam patterns of digital MS: (a) column-wise; (b) chessboard-like.

reflector and fed by a signal generator (Keysight Technologies, N5173B).

Fig. 5.30 displays the beam patterns of reflected waves from designed digital MS that uses two different coding patterns. Full-wave simulations performed with CST revealed that the EM wave beam is reflected with $15.1°$, as shown in Fig. 5.30a, when the column-wise method is followed. The chessboard-like arrangement, on the other hand, contributed to the multi-beam reflected waves. Specifically, the created beams had the reflection angle of $32.2°$, as depicted in Fig. 5.30b. It is worth noting that the ideal match between the simulation and experimental results for both considered configurations well

validates the general idea of digital MS. Finally, one can state that demonstrated MS with interesting properties has a huge potential to advance the SWIPT technology in the context of the WBAN infrastructure.

Summary

The practical DB and TB SGP-based WPT systems with concurrent power and data transfer abilities have been presented in this chapter. It is imperative to mention that both realized WPTs make effective use of the SGP technique to miniaturize the overall resonator area. Furthermore, the realized SWIPT system possessed the 3 MHz bandwidth, at the frequencies purposed for data exchange, making the system support high and low data rate applications. Besides, compact digital MS with beam focusing and multi-beam generation features have been realized that can facilitate the SWIPT technology in WBANs. Finally, all the presented design concepts have been validated by the appropriate experimental measurements that eventually give the realized system a practical significance.

Chapter 6

SGP-based WPT Performance Analysis

A thorough analysis of SGP-based resonators designed for WPT applications is reported in this chapter. For the first time, new findings that relate a resonator and WPT performance metrics to the slot shape, Q, SWE, and RL are presented in a very comprehensive manner. As a case study, a single-loop polygonal shape was considered to carry out all analysis and investigations. It has been identified that the slot shape has no impact on the performance of resonators and, hence, the developed WPT system. Instead, the performance is hugely dependent on Q of resonators regulated by the chosen slot area. These findings allow the conceptualization of systematic analysis of WPT systems and the development of design schemes that are readily realizable, and they also enable a significant improvement in PTE. The developed prototypes conforming to the ISM frequency bands show an enhancement in PTE to the extent of 11% during the measurements. The proposed analysis and design approach are very important steps in advancing the state-of-the-art RF WPTs. In essence, this has a potential to reinvigorate stagnated SGP-based WPTs so as to facilitate the requirements of low-power applications.

6.1 Introduction

The WPT systems have the potential to bring a complete turnaround in a variety of emerging applications. They have been lately employed in a number of segments such as biomedicine, consumer electronics, micro-robotics, vehicular, and emerging wireless technologies [114,115]. WPTs can be broadly classified into far- (radiative) and near-field (non-radiative) types [116]. If the former is accomplished using protocols, namely, time-switching and power-splitting relaying methods [117], the latter is achieved by following any of capacitive or inductive techniques [118]. In this context, it is imperative to mention that the concept of MRC also falls under the umbrella of inductive coupling. This essentially enables the synchronization of the resonance of Tx and Rx to enhance the WPT performance. It should be noted that a number of factors, namely, power level, coupling degree, operating frequency, resonator structure, and size, influence the performance of MRC-based WPTs [25]. Tx and Rx in such WPTs are resonators for which a number of

design techniques exist in literature. For example, cubic high dielectric [64] and cavity resonators [14] have proven their usefulness in the highly efficient WPT design. Nonlinear resonators, on the other hand, are extremely effective at solving the WPT constraints caused by coupling variations [65]. The coils with a parallel configuration, as compared to the series ones, are more suitable for obtaining load-independent WPTs [119].

The literature is replete with reports that discuss the methodologies for resolving the WPT challenges by utilizing distinct slots such as ellipse, square, triangle, circle, hexagon, `U`, `C`, `E`, `H`, *etc.* [44]. Furthermore, SGP also enables ready scalability to the MB resonator operation which is considered the backbone for the successful realization of WPT systems that can support SWIPT [120]. Moreover, the high-Q resonators (in any form) increase the energy coupling, which successfully compensates for the efficiency degradation caused by low couplings [25]. Interestingly, the SGP shapes demonstrate their effectiveness in obtaining high Q [89]. As a result, there are some existing reports that made the utilization of high-Q resonators to develop SGP-type WPTs with excellent performance [44].

It is important to mention that different SGP shapes also bring a compactness to the resonators and eventual WPTs. In essence, the role of SWE is paramount in achieving the size reduction [121]. The microstrip designs can be converted into slow-wave structures by incorporating quasi-lumped elements, different stubs, and conducting strips [122]. Furthermore, the effect of SWE can be maximized by increasing the effective permittivity and permeability [123]. In addition, RL also adversely affects various performance metrics of WPTs. It has been shown that the SGP approach has the potential to significantly reduce RL over a wide spectrum of frequency bands and is, thus, considered an excellent candidate for the design of WPTs [96, 124, 125].

6.2 Motivation

A literature survey reveals that the development of SGP-based WPT systems entails the use of a slot shape in the ground plane to optimize their performance. This leads to the premise that selecting a slot type is commonly a dilemma. However, it is imperative to note that these papers often overlook the other critical parameters such as Q, SWE, and RL that are equally critical in the design of WPT systems. Therefore, the motivation is to first conceptualize various SGP-based WPT architectures in terms of the three above-mentioned parameters. Subsequently, to develop a mechanism for identification of the slot shape in the ground plane that can provide superior performance in terms of these three parameters. It is anticipated that the reported comprehensive analysis and subsequent contributions of this paper may give a new direction to the design techniques for the SGP-based WPT systems.

6.3 Contribution of the Chapter

As a case study, generic single-loop polygonal slots in the ground plane are considered to investigate their effect on the performance of the resonator and resultant WPT system. In this case, the slot can be a triangle, a square, an octagon, a hexagon, or a circle when the sides of a polygon are altered. Consequently, this allows simultaneous observation of the impact of multiple slots on resonator key parameters. As a result, the thorough analysis and subsequent findings have led to the below-listed contributions:

- The development of a theoretical postulation that the resonators with a wide variety of slot shapes and slot areas exhibit excellent RL at the frequency range below 1 GHz and the subsequent experimental demonstration.
- The test and validation of the SWE concept in the single-loop polygonal slot-based resonators. Then, the exploration of the finding that the change in slot shapes negligibly affects SWE.
- The investigation and analysis show that the single-loop polygonal slots with different numbers of sides and possessing the same slot areas exhibit nearly same achievable Q.
- The experimental evaluation of the developed theoretical postulations about the impact of slot's shape and area on the performance of resonators and the eventual WPT systems. In particular, the demonstration of using smaller slots (*i.e.*, greater Q) for achieving higher PTE. The exampling prototype achieved an enhancement of 11% in PTE with the reduction in the slot area.
- Finally, it can be assumed that the provided assessment and explorations may be very beneficial in advancing existing SGP-type WPTs.

6.4 Resonator Overview

It is well established that the characteristics of resonators regulate the performance of WPT systems. Therefore, a brief discussion and explanation of the conventional and SGP-based resonator design strategies are included in this section to understand the nuances involved in the designs.

6.4.1 SGP Technique

The last decade has seen an increased interest in the SGP-based design of high-frequency circuits [124]. It provides a number of benefits including the circuit miniaturization. Furthermore, variously shaped SGPs are employed to improve the performance of microstrip technology-based circuits. For example, the use of SGPs can assist in realizing the circular polarization [126], enhanced polarization purity [98], increased bandwidth at *X*- and *Ku*-bands [127], and filtering structures with different characteristics. The key premise behind the SGP methodology is to create slots on a ground plane in order to change the current flow path [128]. The influence of etched slots is multifaceted and, as a result, they can lead to a variety of outcomes. In essence, in the presence of slots in the ground plane, the typical behavior of transmission lines is significantly modified [129]. As a consequence, MLs demonstrate different stop-band features because of the values of effective L and C caused by the slot. Additionally, the circuit's characteristic impedance (Z_{SGP}) can be found using (6.1) [130]. Here, $Z_0 = 50\ \Omega$ and Γ is computed as $|\Gamma| = 40^{|\mathrm{S}_{11}|}$.

$$Z_{\mathrm{SGP}} = Z_0 \sqrt{\frac{1+|\Gamma|}{1-|\Gamma|}}. \tag{6.1}$$

The SGP-based resonators can be modeled as the parallel RLC [89] or LC [131] circuit whose respective values can be extracted from available EM simulation software and in consonance with (3.12)−(3.14). In addition, unloaded Q of the parallel resonant circuit can be expressed by (4.6).

6.5 Performance Evaluation

The properly designed SGP-based resonator architectures are critical components of magnetically coupled WPT systems. It should be noted that these resonators predetermine the eventual WPT performance. Hence, there is a need for a thorough analysis of resonators that can be regarded as the first vital step toward a successful WPT system. Fig. 6.1 illustrates the SGP-based resonator, its typical measurement, and characterization setup. Its structure consists of three layers, *i.e.*, a single layer of a dielectric material and two layers of copper. The slots are introduced on the bottom side (*i.e.*, a ground plane) while the top side stays unchanged. E_{g} placed below ML aids in the creation of a resonance. It is worth noting that the analysis, design, and optimizations are carried out using EM and circuit simulation software such as CST and ADS.

This work examines the *polygonal single-loop* slots presented in Fig. 6.1a. By its feature polygons are closed geometrical figures confined by straight sides. Besides that, the slots under consideration are assumed to be universal as they can change their form

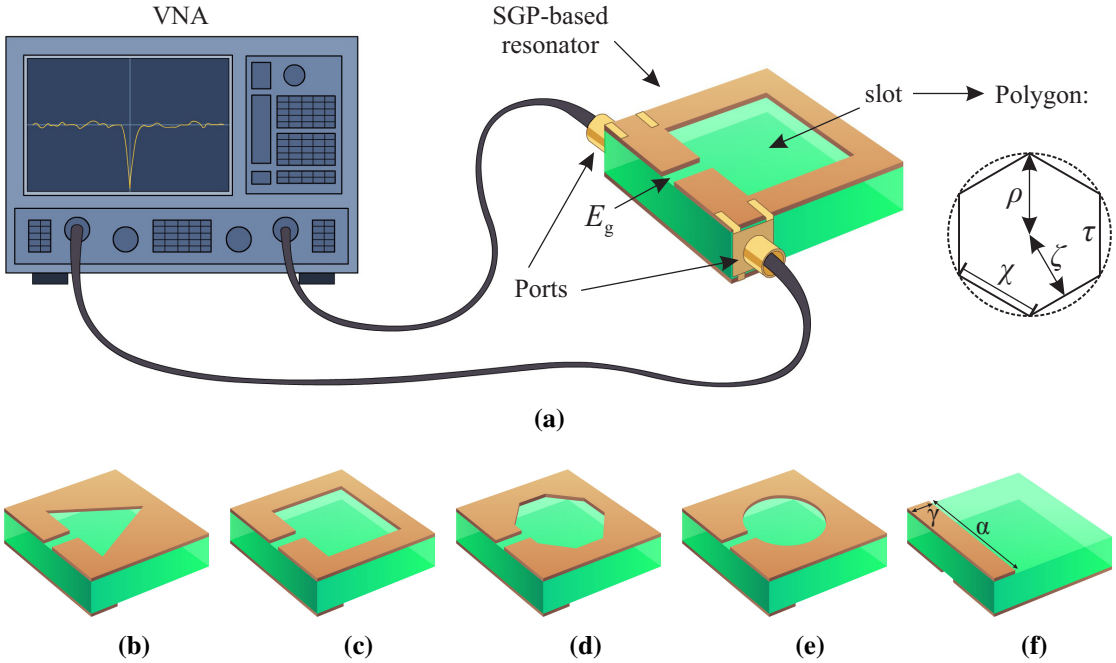

Figure 6.1. The structure of SGP-based resonators (bottom/top) and their measurement: (a) characterization setup; (b) $\tau = 3$; (c) $\tau = 4$; (d) $\tau = 8$; (e) $\tau = 32$; (f) top.

by modifying the number of sides (τ). Thus, the slot geometry can be transformed into various shapes. For example, according to given τ, the slot can be a triangle ($\tau = 3$), a square ($\tau = 4$), a pentagon ($\tau = 5$), a hexagon ($\tau = 6$), a heptagon ($\tau = 7$), an octagon ($\tau = 8$), a nonagon ($\tau = 9$), a decagon ($\tau = 10$), *etc*. Moreover, it is apparent that a large value of τ leads to the circular shape. In these explorations, however, $\tau = 32$ is sufficient to form a circle considering the small area of developed resonators. In addition, the important parameters of the studied slot shapes, such as the in-radius (ζ) and length of sides (χ), can be defined using (6.2) and (6.3), respectively. Here, $\tau \in \{3, 4, \ldots 32\}$ and, apparently, $\uparrow \tau \rightarrow \downarrow \chi$.

$$\zeta = \rho \cos \frac{180^\circ}{\tau}, \tag{6.2}$$

$$\chi = 2\rho \sin \frac{180^\circ}{\tau}. \tag{6.3}$$

All resonators are developed utilizing the Rogers' RO4350B board and have the same area of 25×25 mm^2 for a fair comparison. Furthermore, the selected substrate has h_s of 1.524 mm and h_c of 0.035 mm. Besides, ports of resonators are connected using ML with the 3.4 mm width (γ). In turn, the ports facilitate the connection of resonators to VNA for characterization purposes. It is pertinent to note that polygonal shapes, with different ζ, were considered during the studies for the sake of accuracy and scalability. Particularly, chosen ζ of 6 mm, 12 mm, and 18 mm led to the distinct slot areas. Besides, the τ

value was changed from 3 to 32 to form different slots which, in turn, resulted in various current flow paths on the ground plane. Analyses were performed in terms of three main resonator parameters such as the *radiation loss, slow-wave factor, and quality factor*. The subsequent discoveries of analyses and their experimental validation are discussed in the remaining parts of this chapter.

6.5.1 Radiation Loss

The extensive explorations of RL within the realm of microwave and wireless components are of great interest [132]. The SGPs' EM fields (*i.e.*, electric and magnetic) are distributed in an open space, which can result in a significant EM radiation. Furthermore, this phenomenon may lead to an increase in the insertion loss [133]. Therefore, during the design of the microwave components, the predominant aim is to reduce the RL level [125]. In addition, RL of the developed SGP-type resonators can be computed employing (6.4) [96].

$$\Upsilon = 1 - \left(|\mathrm{S}_{11}|^2 + |\mathrm{S}_{21}|^2\right). \tag{6.4}$$

The RL dependence on τ of polygonal single-loop-based resonators obtained from the EM simulation environment is shown in Fig. 6.2. These results reveal that RL possesses smaller values at lower frequencies, as compared to the higher bands. Although RL does not exceed 40% in any of the cases, the resonators with smaller slots demonstrate lower values. In particular, regardless of the shape variation and change in ζ, RL is less than 5% for the frequency range below 1 GHz. Therefore, it is safe to state that resonators with any shape and slot area can be utilized for the realization of WPT system operating around these frequencies.

6.5.2 Slow-Wave Effect

Low-frequency circuits, in general, necessitate boards with a huge area. As a concept, board size reduction is the process of reducing a circuit's frequency response while leaving all other parameters the same. This necessitates using different innovative solutions to reduce the overall circuit size, and one such approach is related to SWE [121]. The fundamental idea behind SWE is to store the maximum magnetic and electric energy independently. In general, the ML technology-reliant circuits are unable of reducing phase velocity to less than $\frac{1}{\varepsilon_\mathrm{r}}$. Because in such systems the utilized substrate's ε_r define the length of the transmission line [134]. In turn, the reduction of a phase velocity results in a smaller wavelength [135].

The SGP technique shows the SWE features which allow to control of SWF and, in turn, the circuit miniaturization [136]. It essentially shows the rate of interdependence between the ML propagation constant and wave number in free space. As a concept, SWE

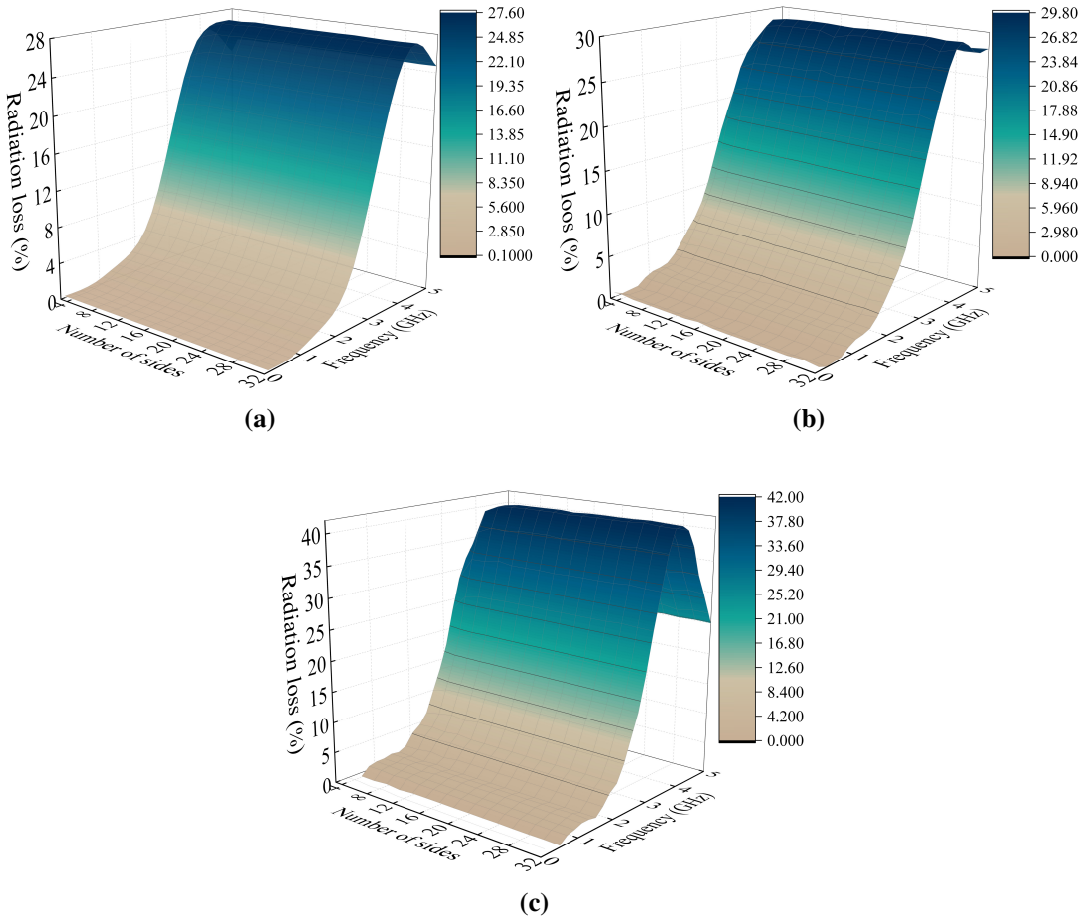

Figure 6.2. Simulated RL of different SGP-based resonators:
(a) $\zeta = 6$ mm; (b) $\zeta = 12$ mm; (c) $\zeta = 18$ mm.

is demonstrated by the shift of resonance towards lower frequencies. Moreover, SWF of the SGP structure is computed using (6.5) [96]. Here, α stands for the ML length; λ_0 represents the guided wavelength; $\Delta\theta$ is a phase difference for ML, either with or without an etched slot. Finally, (6.6) can be utilized to find an average effective permittivity of a circuit.

$$\Phi = \frac{\lambda_0 \Delta\theta}{360\alpha} + \sqrt{\varepsilon_{\text{eff}}}, \tag{6.5}$$

$$\varepsilon_{\text{eff}} = \frac{\varepsilon_{\text{r}} + 1}{2} + \frac{\varepsilon_{\text{r}} - 11}{2}\left(1 + 12\frac{h_{\text{s}}}{\gamma}\right)^{-0.5}. \tag{6.6}$$

6.5.3 Quality Factor

It is important to mention that high-performance coupling-based WPTs rely on high-Q resonators. For example, as the transmission distance between Tx and Rx increases, the coupling weakens, necessitating a rise in Q of resonators in order to improve PTE [86].

Keeping this in the perspective, a number of reports discussed the increase in Q by changing the coil structures or proposing new innovative solutions [137, 138]. Furthermore, the SGP method can also enable achieving high Q by controlling the geometry of given SGP shapes. Two different approaches can be used to determine Q, particularly, using the values of either RLC [89] or LC [95]. It should be noted, at this instance, that there is an extremely small difference between these two approaches. However, in these analyses, Q was defined following the conventional method which uses (6.7). Here, β represents the "-3" dB bandwidth.

$$\mathrm{Q} = \frac{f_0}{\mathrm{bw}}. \tag{6.7}$$

The SGP-based resonator has a resonance behavior, where L comes from ML whereas the constant capacitance is produced by fixed E_g. It is apparent that it results in a resonant frequency that potentially may vary from the desired one. Consequently, there is a need for a solution that helps control the resonance (*i.e.*, the system's operating frequency). Within the concept of SGP-based resonators, it can be achieved by loading C_e in the excitation gap. Subsequently, C_e with the aptly set value aid in the control of resonant frequency. The appropriate values of C_e were incorporated to further investigate the chosen slot shapes and achievable Q at the practical frequencies. It is pertinent to note that the selected frequency was 900 MHz which complies with the ISM bands. Furthermore, τ of the polygonal shape was fixed to four (which is common for all) and only ζ was modified.

6.5.4 Experimental Validation of Resonators

The prototypes depicted in Fig. 6.3, included for investigation purposes, were fabricated using the same substrate (*i.e.*, RO4350B) as utilized during the EM simulations. Furthermore, the experimental evaluations of these prototypes were carried out using the Keysight PNA-X (N5247B)-based setup shown in Fig. 6.3. At the outset, Fig. 6.4 compares the simulation and experimental RL results for resonators with different slots. Apparently, the measurement outcomes are in perfect consonance with the corresponding EM simulation results. There is a slight anomaly and it is evident with a minor effect of τ on RL; however, the resonators with greater ζ exhibit a trend of having higher RL. Particularly, experimental RL of about 7.5%, 20.5%, and 26% were computed for the SGP-based resonators with ζ of 6 mm, 12 mm, and 18 mm, respectively. It is worth mentioning that these values were calculated considering the initial resonance of resonators.

Next, Fig. 6.5 depicts the transmission phase values of the fabricated resonators with and without SGPs. It can be readily inferred that the phase responses of resonators, based on single-loop polygonal slots with different τ, are nearly similar in both simulation and experimental measurements. The utilization of these obtained values and (6.5) enable the SWF calculation. The EM simulated and experimental results of SWF for the designed

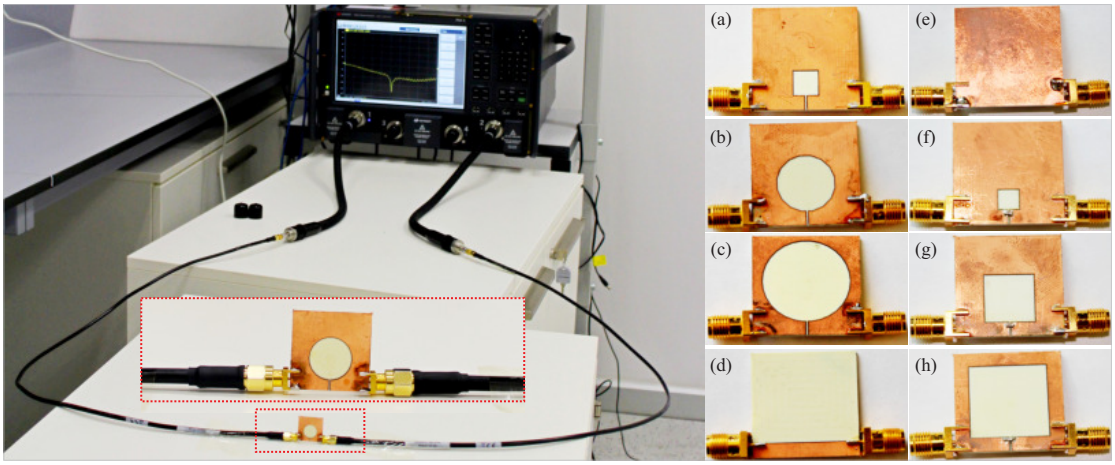

Figure 6.3. The resonator measurement setup and few examples of fabricated prototypes: (a) $\zeta = 6$ mm, $\tau = 4$; (b) $\zeta = 12$ mm, $\tau = 16$; (c) $\zeta = 18$ mm, $\tau = 32$; (d) top; (e) no slot; (f)−(h) resonators with loaded SMD capacitors.

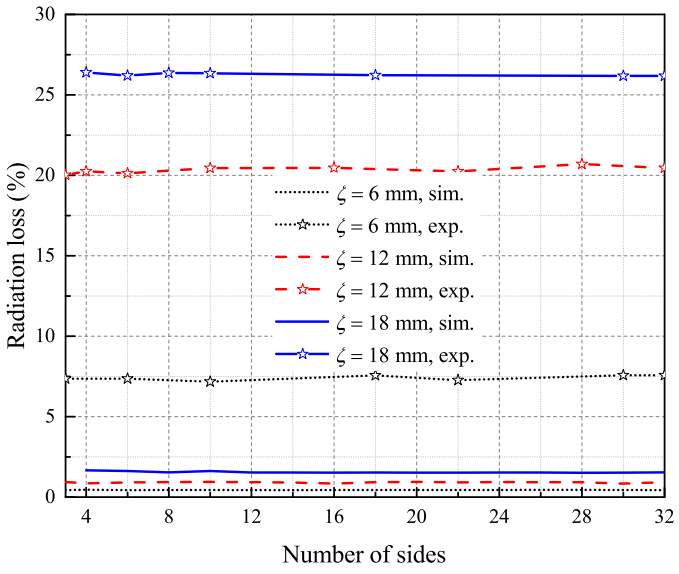

Figure 6.4. Obtained results for RL vs τ.

SGP-based resonators, possessing the proposed slots, with varying τ, can be seen in Fig. 6.6. It is pertinent to note, in this instance, that there is an excellent agreement between both simulated and experimental results. These results allow conveying that *the impact of variations in polygon's τ has a negligible effect on SWF*, whereas it gets significantly impacted with the variation in ζ. It is also obvious that SWF rises to its maximum value around the resonant frequency and then falls suddenly. In this particular case, it is worth mentioning that the resonance of around 3.9 GHz, 2.45 GHz, and 1.75 GHz was obtained, when $\zeta = 6$ mm, $\zeta = 12$ mm, and $\zeta = 18$ mm, respectively.

For the evaluation of Q, one can assess obtained Q for polygonal single-loop SGP-based resonators with different τ shown in Fig. 6.7. It is apparent that, although τ of

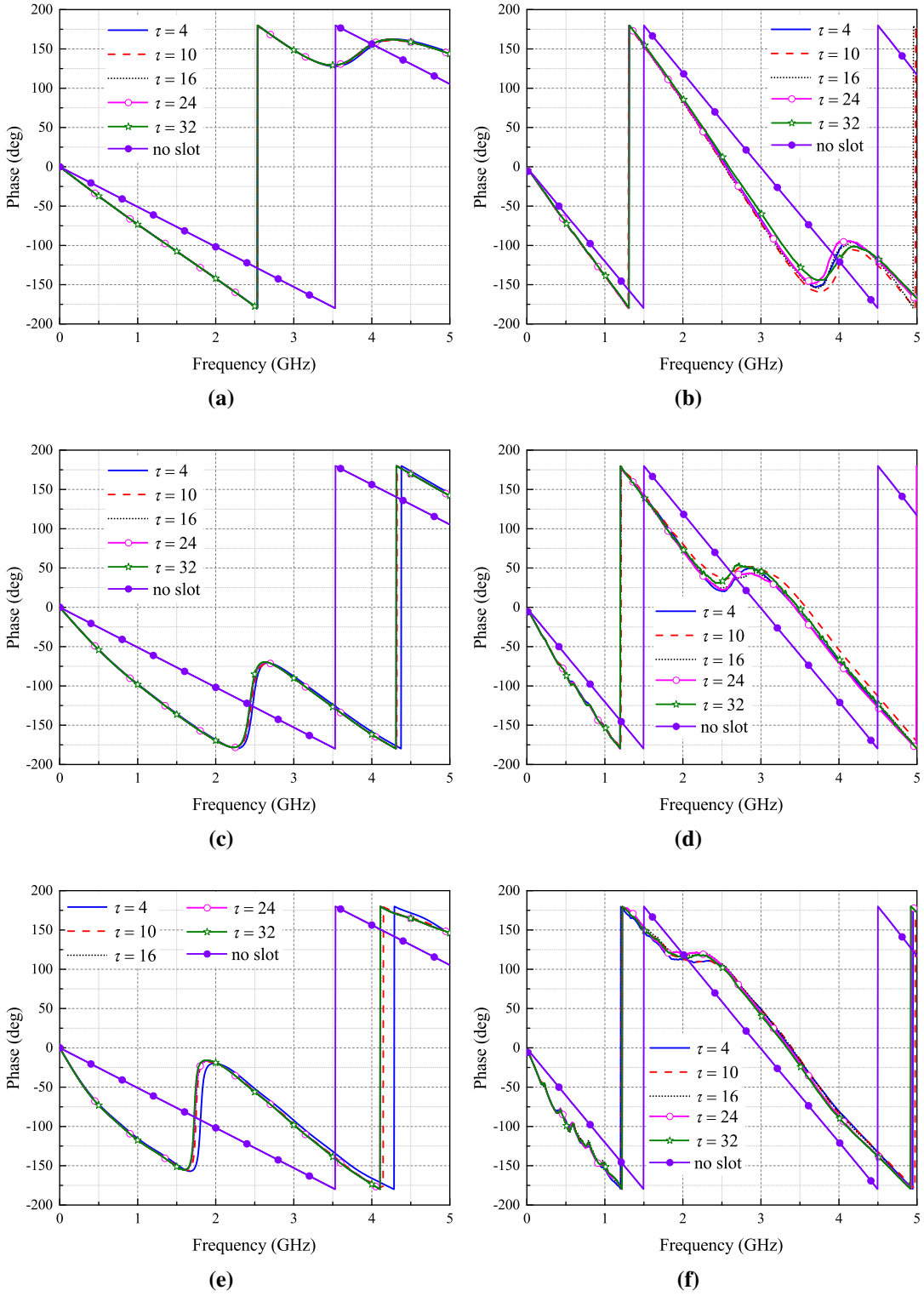

Figure 6.5. Transmission phase vs frequency results for resonators with different ζ and arbitrary τ: (a) $\zeta = 6$ mm, sim.; (b) $\zeta = 6$ mm, exp.; (c) $\zeta = 12$ mm, sim.; (d) $\zeta = 12$ mm, exp.; (e) $\zeta = 18$ mm, sim.; (f) $\zeta = 18$ mm, exp.

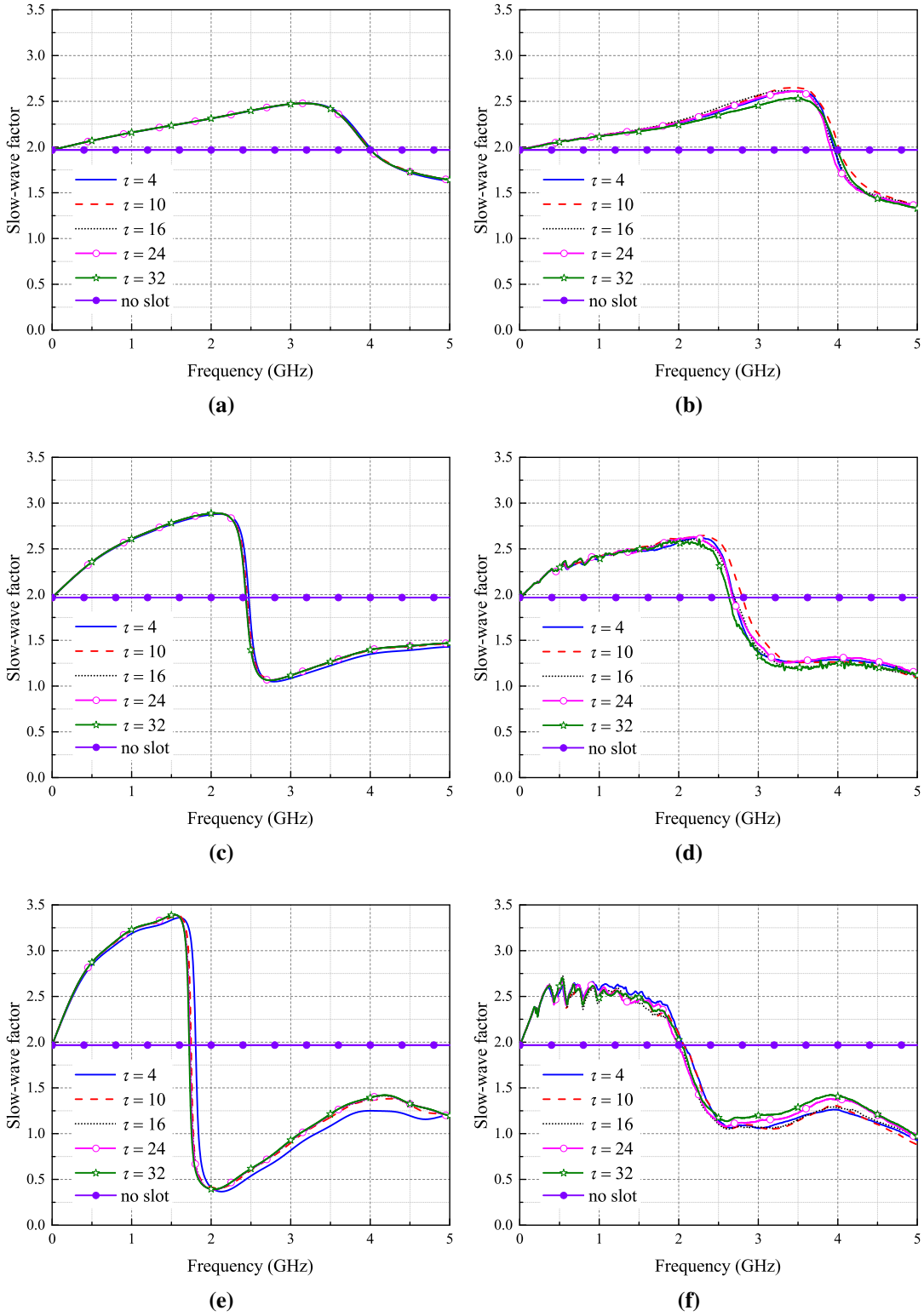

Figure 6.6. SWF vs frequency results for resonators with different ζ and arbitrary τ: (a) $\zeta = 6$ mm, sim; (b) $\zeta = 12$ mm, sim.; (c) $\zeta = 18$ mm, sim.; (d) $\zeta = 6$ mm, exp.; (e) $\zeta = 12$ mm, exp.; (f) $\zeta = 18$ mm, exp.

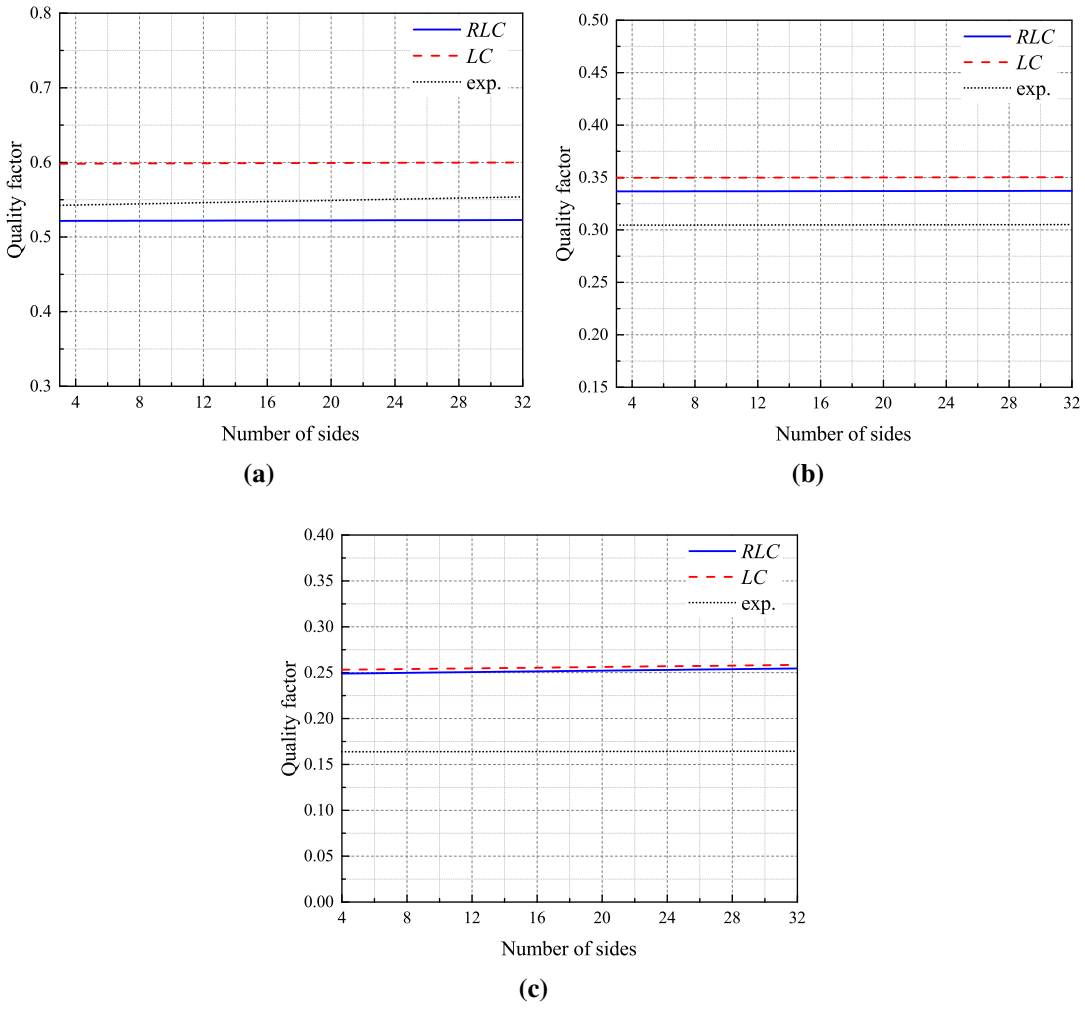

Figure 6.7. Q vs polygonal slots with different τ: (a) $\zeta = 6$ mm; (b) $\zeta = 12$ mm; (c) $\zeta = 18$ mm.

the proposed slot is shape-dependent, all resonators achieve nearly same Q. However, it further reveals that the resonators with smaller slots possess higher Q. This finding leads to the idea that Q is more reliant on the slot area rather than the type of shapes. As a consequence, it is fair to conclude that *the shape does not play a significant role in achieving high Q*. Furthermore, the obtained experimental results in Fig. 6.7 also validate this discovery. The measured Q values of the resonators with $\zeta = 18$ mm slot are almost three times smaller than the ones with $\zeta = 6$ mm slot. In addition, it can be easily gleaned that experimental Q of the resonators with the smallest slots falls between computed Q using the RLC and LC methods. However, for bigger slots, the experimental Q values are smaller as compared to the EM simulated results. This slight anomaly may be attributed to the higher losses associated with bigger slots. Thus, it is safe to convey that both approaches can be only used to approximate realized Q.

On the other hand, Fig. 6.8 presents the EM and circuit simulations along with the

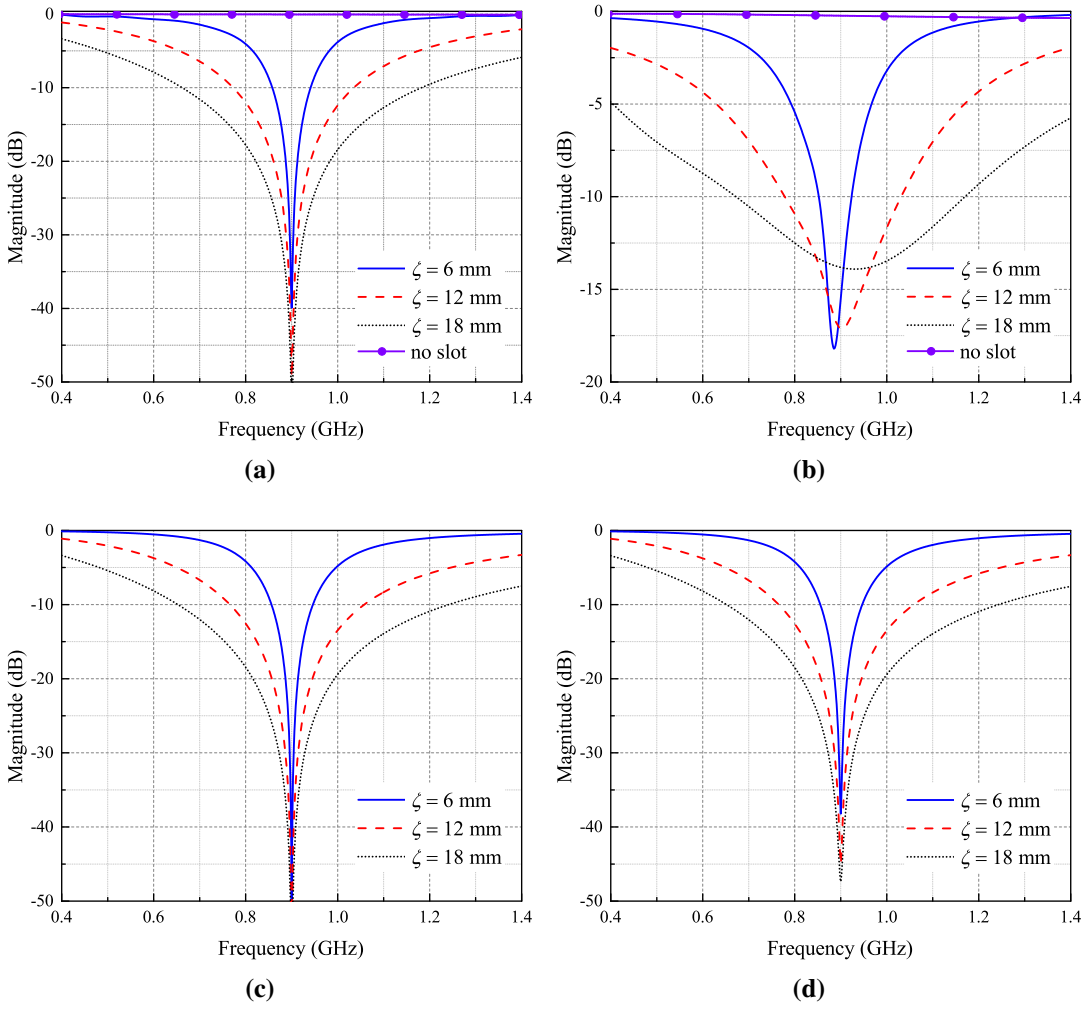

Figure 6.8. S_{21} vs frequency results for resonators with $\tau = 4$ and different ζ: (a) sim.; (b) exp.; (c) LC; (d) RLC.

experimental results of SGP-based resonators. It can be clearly seen that the resonance for all three cases occurs at 900 MHz. It can also be seen that the resonator with a smaller slot area possesses higher Q and it reiterates the earlier findings mentioned above. In particular, using (6.7) gives respective Q of 3.72, 1.22, and 0.67 for $\zeta = 6$ mm, $\zeta = 12$ mm, and $\zeta = 18$ mm.

6.6 WPT Development

The use of the MRC-based technique in the design of near-field WPT systems significantly enhances the overall system performance [139]. Apparently, the successful realization of this method highly depends on the performance of the SGP-based resonators which act as the system's end-modules. In such systems, one resonator acts as Tx whereas another one is Rx. Essentially, the optimized resonators, meeting the WPT specification

Table 6.1. Parameters of fabricated resonators for WPTs.

	C_e (pF)	α (mm)	γ (mm)
$\zeta = 6$ mm	3	16.7	3.4
$\zeta = 12$ mm	0.9	16.4	3.4

requirements, can be coupled at a certain proximity to achieve the power transfer wirelessly. In this instance, it is important to highlight that the coupled resonators should oscillate at the same frequency. The creation of an EM field is successfully achieved when the appropriate coupling is met. Thereby, the power transfer, from Tx to Rx, becomes possible at the selected frequency [120]. It has been well established that PTE of coupling technique-based WPT systems is mainly influenced by two key factors, namely, Q of the unloaded resonators and k between Tx and Rx [86]. It has been reported that k decreases rapidly with the increase in a separation distance between the coupled resonators and this, in turn, leads to reduced PTE [25]. Therefore, the high-Q resonators are used to achieve high PTE from the WPT systems with weak k [140].

As mentioned earlier, the development of WPT systems requires two resonators, one each working as Tx and Rx, which are appropriately designed to meet the WPT specifications. Once these are brought in close proximity, the wireless power transfer starts. However, as the first step, from these coupled resonators working as the sub-optimal WPT systems, some key parameters should be extracted. This enables the impedance matching, *i.e.*, between the resonators and 50-Ω ports (P1 and P2). This makes sure that there are minimal losses at the ports. The required matching was performed aptly using the J-inverter approach which also aided in the retrieval of WPT's important parameters. In addition, once the design phase is over there is a need for the final optimizations to further enhance the obtained outcomes.

As shown in the previous section the ζ change affects the resonator performance more as compared to the τ variation. Therefore, the square slot-based resonator with two different slot areas (*i.e.,* $\zeta = 6$ mm and $\zeta = 12$ mm) were selected to show the influence of this new finding on the WPT system performance. The resonator parameters for the WPT development are given in Table 6.1. Furthermore, the RO4350B board (with $\varepsilon_r = 3.48$) was used for prototyping the designed resonators. Two same SGP-type resonators were fabricated, for both cases, to implement the WPT system. The high-tolerance capacitors (SMD-type) with the required values were soldered to all fabricated resonators. It is worth noting that both WPTs are designed to work at 900 MHz. The developed resonators of WPT systems were perfectly aligned and separated by 25 mm during the experimental measurements. Fig. 6.9 depicts the general WPT experimental measurement and realized two WPTs. Moreover, SMA-type connectors were used to connect Tx and Rx to the

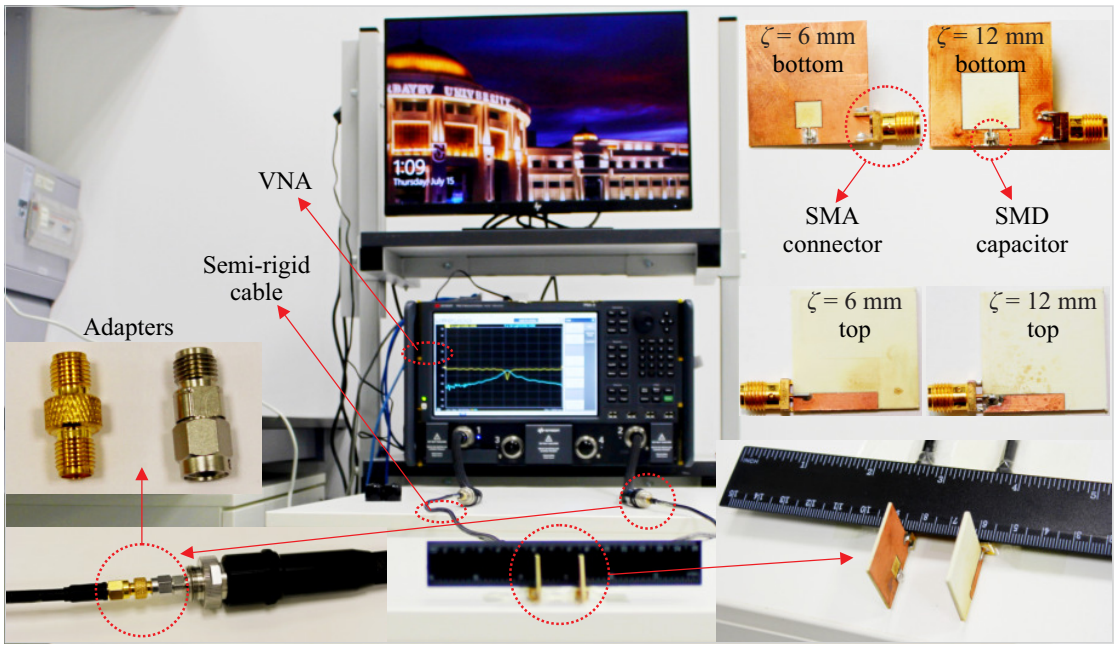

Figure 6.9. WPT measurement setup and fabricated resonator prototypes.

semi-rigid cables. In turn, they were connected to the probes of employed VNA (PNA-X, N5247B) by means of two adapters. Consequently, this allows the measurement of S-parameters of WPT, which can then be utilized to compute PTE.

The simulation and measurement results, depicted in Fig. 6.10, show a very good agreement for both example prototypes. The values of S_{11} convey that these resonators used in the development of WPT possess remarkable impedance matching at the chosen frequency. On the other hand, the values of S_{21} demonstrate an excellent transmission capability at the operating frequency of 900 MHz. These outcomes can be used to calculate PTE of developed WPTs using (3.6). The respective simulated efficiencies obtained from the EM simulation results for ζ of 6 mm and 12 mm are 78% and 72%. The corresponding experimental values for ζ of 6 mm and 12 mm are 73% and 62%, accordingly. It is clear from both simulation and experimental results that PTE for WPTs with smaller ζ is higher when compared to PTE for WPTs having bigger ζ. Furthermore, there was a 6% decline in PTE during the simulation whereas the reduction in the experimental value was 11% for the two example cases. This outcome again highlights *the extreme importance of Q in the practical realization of high-performance WPT systems*. Just to reiterate, the larger slots (signified by greater ζ) lead to lower Q. On a side note, PTEs degrade more during the experiments, as compared to the simulations, owing to the non-idealities associated with all the utilized components and, thus, incur extra losses which ultimately lead to reduced PTEs.

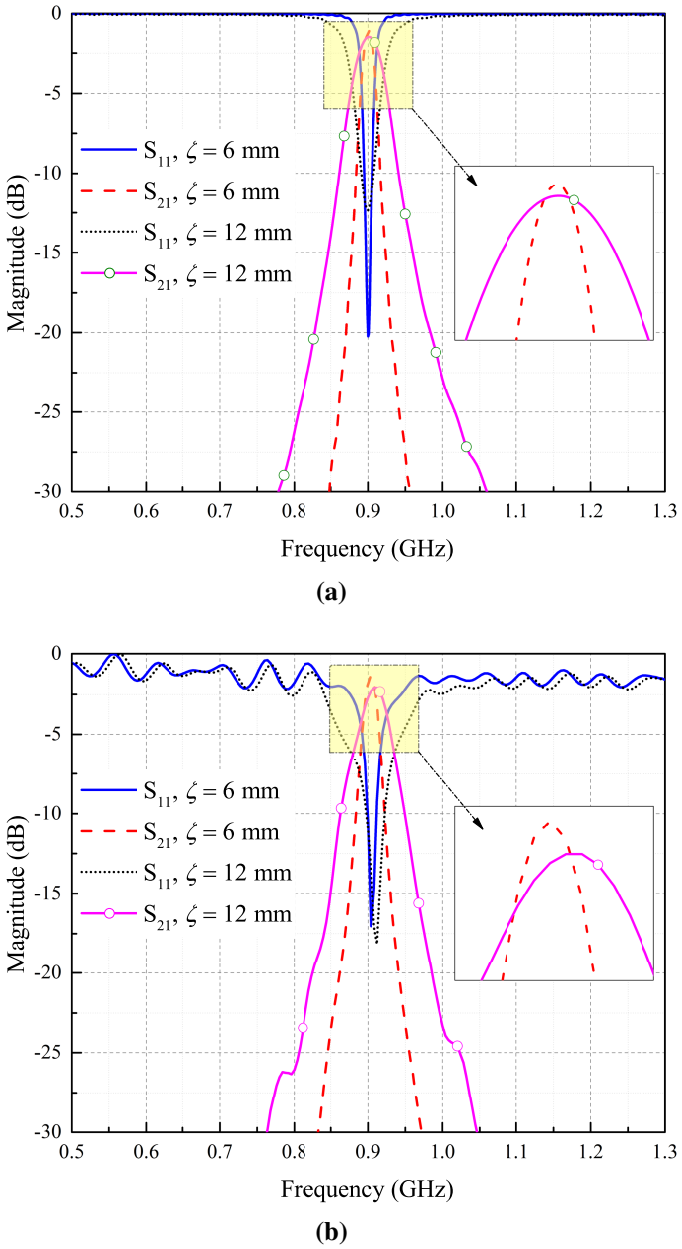

Figure 6.10. The obtained results of two developed WPTs, S-parameters vs frequency: (a) EM simulated; (b) experimental.

Chapter Summary

Systematic analysis to understand the behavior of single-loop polygonal slot-based resonators has been reported in this chapter. The emphasis has been on achievable Q, SWF, and RL using various slots as these are the key parameters of resonators. It has been demonstrated that the area of the proposed slot plays a major role in the resonator performance when compared to different shape types. The new findings, from the carried-out investigations and analysis, can facilitate the realization of high-performance yet robust SGP-based WPT systems.

Chapter 7

Conclusions and Future Works

Over the recent years, both FF and NF WPT systems have emerged as an advancing technology that covers a broad range of applications. Within the realm of NF WPTs, MRC-based WPT systems are of significant interest due to their superiority, namely, greater PTD, higher PTE, and operation at the MHz region. In this context, it is imperative to mention that the use of the SGP concept in the design and realization of miniature, robust, and high-performance MRC-based NF WPTs has gained prominence. In addition, SGP allows developing the MB WPT systems that can support the simultaneous wireless power and data transmission regime.

The SGP technique has been utilized in the development of the practical performance-enhanced SB, DB, and TB WPT systems. In particular, distinct geometrical slots such as the plus, Archimedean coil, square, and double-ellipse were considered in the design of SGP-based NF WPTs. It is imperative to note that all realized WPTs demonstrated high FoMs. Furthermore, the data exchange aspects of SWIPT were investigated during the design process for the first time, specifically, the achievable bandwidth at the communication bands was examined. Subsequently, the parameters of the developed SWIPT system were optimized to achieve 3 MHz at the frequencies dedicated for data transfer. In turn, this property allows realized SWIPT to support various low-power applications necessitating low and high data rates. In addition, two-bit coded MS with beam focusing and multi-beam creation capabilities has been realized that facilitates the SWIPT technology in WBAN. It is also worth noting that all designed SGP-type WPTs were validated by the appropriately carried-out experimental measurements and, consequently, this makes the realized WPT systems practically viable. Finally, it is presumed that implemented WPTs with superior characteristics have a potential to lift this domain to a new height.

A thorough assessment of resonators using single-loop polygonal slots has been provided in terms of three key parameters such as Q, SWF, and RL. Subsequently, it was explored that the slot area is more important than different slot geometries. It can be expected that the explorations of this work may serve as a catalyst for maturing the general SGP-based WPT systems. Furthermore, it has been reported that WPTs utilizing such resonators can be designed in a first-pass manner with an excellent agreement between

the simulation and experimental results. In particular, it has been shown that the increase of 11% in PTE was achieved experimentally by WPT having a smaller slot area when two WPTs with different slot areas were compared.

It is important to note that, recently, the SGP-based WPTs have gone through considerable progress. However, still, there is a need to advance this technique so as to make it practically realizable and appealing for real-time applications. Three examples of potentially useful directions are elaborated below:

- It is well-known that high Q leads to a smaller bandwidth. In scenarios, where WPTs are also used for the data transfer the achievable data rate becomes important which is directly related to the bandwidth. Hence, huge trade-offs are needed in the system design process where the applications require both power and data transfers. Furthermore, the other parameters of planarized circuits can affect both power and information in different manners. This aspect can be addressed by the use of machine learning algorithms to achieve optimal design solutions. This will bring a paradigm shift in this field.

- In general, the SGP-based WPT systems are extremely sensitive, and this fact is often reflected in the mismatch between the simulation and experimental performance. This necessitates a robust measurement and characterization strategy in addition to a robust design scheme to mitigate measurement-related issues.

- It is apparent that the performance of MRC-type NF WPTs degrades considerably when Tx and Rx are not aligned perfectly. In this regard, the artificially designed MTM slabs can be remarkably beneficial. For example, the slabs can be placed between the Tx and Rx resonators, which can help manipulate generated `H` in the direction of the Rx location. Thus, there is a MTMs and SGP-type WPTs that aids in designing the misalignment-insensitive WPT systems.

Bibliography

[1] "The top 10 emerging technologies for 2012. forum w e.." https://www.weforum.org/agenda/2012/02/the-2012-top-10-emerging-technologies/.

[2] "The top 10 emerging technologies for 2013. forum w e.." https://www.weforum.org/agenda/2013/02/top-10-emerging-technologies-for-2013/.

[3] "10 breakthrough technologies 2016. review m t.." https://www.technologyreview.com/lists/technologies/2016/set/id/600869/.

[4] "Wireless power: mobile devices, consumer electronics, wireless power infrastructure, and wireless charging of electric vehicles: global market analysis and forecasts. research n.." https://www.navigantresearch.com/research/wireless-power.

[5] J. Garnica, R. A. Chinga, and J. Lin, "Wireless power transmission: From far field to near field," *Proceedings of the IEEE*, vol. 101, pp. 1321–1331, Jun. 2013.

[6] K. Dautov, M. S. Hashmi, N. Nasimuddin, M. A. Chaudhary, and G. Nauryzbayev, "Quantifying the impact of slow wave factor on closed-loop defect-based wpt systems," *IEEE Transactions on Instrumentation and Measurement*, vol. 71, pp. 1–10, Jun. 2022.

[7] Y.-C. Hsieh, Z.-R. Lin, M.-C. Chen, H.-C. Hsieh, Y.-C. Liu, and H.-J. Chiu, "High-efficiency wireless power transfer system for electric vehicle applications," *IEEE Transactions on Circuits and Systems II: Express Briefs*, vol. 64, pp. 942–946, Aug. 2017.

[8] I. Ghotbi, M. Najjarzadegan, H. Sarfaraz, S. Jafarabadi Ashtiani, and O. Shoaei, "Enhanced power-delivered-to-load through planar multiple-harmonic wireless power transmission," *IEEE Transactions on Circuits and Systems II: Express Briefs*, vol. 65, pp. 1219–1223, Sep. 2018.

[9] J. Xu, Y. Zeng, and R. Zhang, "Uav-enabled wireless power transfer: Trajectory design and energy optimization," *IEEE Transactions on Wireless Communications*, vol. 17, pp. 5092–5106, Aug. 2018.

[10] J. McSpadden and J. Mankins, "Space solar power programs and microwave wireless power transmission technology," *IEEE Microwave Magazine*, vol. 3, pp. 46–57, Dec. 2002.

[11] C.-J. Chen, T.-H. Chu, C.-L. Lin, and Z.-C. Jou, "A study of loosely coupled coils for wireless power transfer," *IEEE Transactions on Circuits and Systems II: Express Briefs*, vol. 57, pp. 536–540, Jul. 2010.

[12] B. L. Cannon, J. F. Hoburg, D. D. Stancil, and S. C. Goldstein, "Magnetic resonant coupling as a potential means for wireless power transfer to multiple small receivers," *IEEE Transactions on Power Electronics*, vol. 24, pp. 1819–1825, Jul. 2009.

[13] F. Jolani, Y. Yu, and Z. Chen, "A planar magnetically coupled resonant wireless power transfer system using printed spiral coils," *IEEE Antennas and Wireless Propagation Letters*, vol. 13, pp. 1648–1651, Aug. 2014.

[14] H. Mei, K. A. Thackston, R. A. Bercich, J. G. Jefferys, and P. P. Irazoqui, "Cavity resonator wireless power transfer system for freely moving animal experiments," *IEEE Transactions on Biomedical Engineering*, vol. 64, pp. 775–785, Apr. 2017.

[15] S. Arzykulov, G. Nauryzbayev, T. A. Tsiftsis, and M. Abdallah, "On the performance of wireless powered cognitive relay network with interference alignment," *IEEE Transactions on Communications*, vol. 66, pp. 3825–3836, May 2018.

[16] M. Kiani and M. Ghovanloo, "An rfid-based closed-loop wireless power transmission system for biomedical applications," *IEEE Transactions on Circuits and Systems II: Express Briefs*, vol. 57, pp. 260–264, Apr. 2010.

[17] G. Wang, P. Wang, Y. Tang, and W. Liu, "Analysis of dual band power and data telemetry for biomedical implants," *IEEE Transactions on Biomedical Circuits and Systems*, vol. 6, pp. 208–215, Jun. 2012.

[18] M. Mohamed, M. Cheffena, A. Moldsvor, and F. P. Fontan, "Physical-statistical channel model for off-body area network," *IEEE Antennas and Wireless Propagation Letters*, vol. 16, pp. 1516–1519, Jan. 2017.

[19] M. Treffers, "History, current status and future of the wireless power consortium and the qi interface specification," *IEEE Circuits and Systems Magazine*, vol. 15, pp. 28–31, May 2015.

[20] H. Hertz, "Dictionary of scientific biography," *Scribner*, vol. 6, pp. 340–349, 1981.

[21] W. Brown, "The history of power transmission by radio waves," *IEEE Transactions on Microwave Theory and Techniques*, vol. 32, pp. 1230–1242, Sep. 1984.

[22] N. Tesla, "Apparatus for transmitting electrical energy," *U.S. Patent 1 119 732 A*, Dec. 1914.

[23] N. Tesla, "The true wireless," *Electrical Experimenter*, vol. 4, pp. 28–34, May. 1919.

[24] S. Y. R. Hui, W. Zhong, and C. K. Lee, "A critical review of recent progress in mid-range wireless power transfer," *IEEE Transactions on Power Electronics*, vol. 29, pp. 4500–4511, Sep. 2014.

[25] S. D. Barman, A. W. Reza, N. Kumar, M. E. Karim, and A. B. Munir, "Wireless powering by magnetic resonant coupling: Recent trends in wireless power transfer system and its applications," *Renewable and Sustainable Energy Reviews*, vol. 51, pp. 1525–1552, Nov. 2015.

[26] P. E. Glaser, "Power from the sun: Its future," *Science*, vol. 162, pp. 857–861, Nov. 1968.

[27] G. A. Covic and J. T. Boys, "Modern trends in inductive power transfer for transportation applications," *IEEE Journal of Emerging and Selected Topics in Power Electronics*, vol. 1, pp. 28–41, May 2013.

[28] J. T. Boys and G. A. Covic, "The inductive power transfer story at the university of auckland," *IEEE Circuits and Systems Magazine*, vol. 15, pp. 6–27, May 2015.

[29] A. Kurs, A. Karalis, R. Moffatt, J. D. Joannopoulos, P. Fisher, and M. Soljačić, "Wireless power transfer via strongly coupled magnetic resonances," *Science*, vol. 317, pp. 83–86, Jul. 2007.

[30] S. Aldhaher, P. C.-K. Luk, K. E. K. Drissi, and J. F. Whidborne, "High-input-voltage high-frequency class e rectifiers for resonant inductive links," *IEEE Transactions on Power Electronics*, vol. 30, pp. 1328–1335, Apr. 2015.

[31] Z.-H. Wang, Y.-P. Li, Y. Sun, C.-S. Tang, and X. Lv, "Load detection model of voltage-fed inductive power transfer system," *IEEE Transactions on Power Electronics*, vol. 28, pp. 5233–5243, Feb. 2013.

[32] R. Bosshard and J. W. Kolar, "All-sic 9.5 kw/dm3 on-board power electronics for 50 kw/85 khz automotive ipt system," *IEEE Journal of Emerging and Selected Topics in Power Electronics*, vol. 5, pp. 419–431, Nov. 2017.

[33] H. L. Li, A. P. Hu, and G. A. Covic, "A direct ac–ac converter for inductive power-transfer systems," *IEEE Transactions on Power Electronics*, vol. 27, pp. 661–668, Jun. 2012.

[34] N. Xuan Bac, D. M. Vilathgamuwa, and U. K. Madawala, "A sic-based matrix converter topology for inductive power transfer system," *IEEE Transactions on Power Electronics*, vol. 29, pp. 4029–4038, Nov. 2014.

[35] C.-Y. Liou, C.-J. Kuo, and S.-G. Mao, "Wireless-power-transfer system using near-field capacitively coupled resonators," *IEEE Transactions on Circuits and Systems II: Express Briefs*, vol. 63, pp. 898–902, Sep. 2016.

[36] P. S. Riehl, A. Satyamoorthy, H. Akram, Y.-C. Yen, J.-C. Yang, B. Juan, C.-M. Lee, F.-C. Lin, V. Muratov, W. Plumb, and P. F. Tustin, "Wireless power systems for mobile devices supporting inductive and resonant operating modes," *IEEE Transactions on Microwave Theory and Techniques*, vol. 63, pp. 780–790, Mar. 2015.

[37] X. Lu, P. Wang, D. Niyato, D. I. Kim, and Z. Han, "Wireless charging technologies: Fundamentals, standards, and network applications," *IEEE Communications Surveys Tutorials*, vol. 18, pp. 1413–1452, Nov. 2016.

[38] H.-J. Kim, H. Hirayama, S. Kim, K. J. Han, R. Zhang, and J.-W. Choi, "Review of near-field wireless power and communication for biomedical applications," *IEEE Access*, vol. 5, pp. 21264–21285, Sep. 2017.

[39] J. Wang, J. Li, S. L. Ho, W. Y. Chau, W. K. Lee, W. N. Fu, Y. Li, H. Yu, and M. Sun, "Study and experimental verification of a rectangular printed-circuit-board wireless transfer system for low power devices," *IEEE Transactions on Magnetics*, vol. 48, pp. 3013–3016, Nov. 2012.

[40] M. Mohammadi Falavarjani, M. Shahabadi, and J. Rashed-Mohassel, "Design and implementation of compact wpt system using printed spiral resonators," *Electronics Letters*, vol. 50, pp. 110–111, Jan. 2014.

[41] N. Shinohara, "Power without wires," *IEEE Microwave Magazine*, vol. 12, pp. S64–S73, Dec. 2011.

[42] S. Hekal, A. B. Abdel-Rahman, H. Jia, A. Allam, A. Barakat, T. Kaho, and R. K. Pokharel, "Compact wireless power transfer system using defected ground band-stop filters," *IEEE Microwave and Wireless Components Letters*, vol. 26, pp. 849–851, Oct. 2016.

[43] F. Tahar, A. Barakat, R. Saad, K. Yoshitomi, and R. K. Pokharel, "Dual-band defected ground structures wireless power transfer system with independent external and inter-resonator coupling," *IEEE Transactions on Circuits and Systems II: Express Briefs*, vol. 64, pp. 1372–1376, Aug. 2017.

[44] A. Barakat, K. Yoshitomi, and R. K. Pokharel, "Design approach for efficient wireless power transfer systems during lateral misalignment," *IEEE Transactions on Microwave Theory and Techniques*, vol. 66, pp. 4170–4177, Sep. 2018.

[45] A. Barakat, S. Alshhawy, K. Yoshitomi, and R. K. Pokharel, "Triple-band near-field wireless power transfer system using coupled defected ground structure band stop filters," in *2019 IEEE MTT-S International Microwave Symposium (IMS)*, pp. 1411–1414, Jun. 2019.

[46] S. Hekal, A. B. Abdel-Rahman, H. Jia, A. Allam, A. Barakat, and R. K. Pokharel, "A novel technique for compact size wireless power transfer applications using defected ground structures," *IEEE Transactions on Microwave Theory and Techniques*, vol. 65, pp. 591–599, Feb. 2017.

[47] N. Karmakar, S. Roy, and I. Balbin, "Quasi-static modeling of defected ground structure," *IEEE Transactions on Microwave Theory and Techniques*, vol. 54, pp. 2160–2168, May 2006.

[48] Y. Zhang, Z. Zhao, and K. Chen, "Frequency-splitting analysis of four-coil resonant wireless power transfer," *IEEE Transactions on Industry Applications*, vol. 50, pp. 2436–2445, Jul. 2014.

[49] S. Verma, D. Rano, and M. Hashmi, "A novel dual band defected ground structure for short range wireless power transfer applications," in *2019 IEEE Wireless Power Transfer Conference (WPTC)*, pp. 188–191, Jun. 2019.

[50] F. Tahar, R. Saad, A. Barakat, and R. K. Pokharel, "1.06 fom and compact wireless power transfer system using rectangular defected ground structure resonators," *IEEE Microwave and Wireless Components Letters*, vol. 27, pp. 1025–1027, Nov. 2017.

[51] R. Sharaf, A. B. Abdel-Rahman, A. S. Abd El-Hameed, A. Barakat, S. Hekal, and A. Allam, "A new compact dual-band wireless power transfer system using interlaced resonators," *IEEE Microwave and Wireless Components Letters*, vol. 29, pp. 498–500, Jul. 2019.

[52] S. Verma, D. Rano, M. Hashmi, and V. Bohara, "A high q dual e-shaped defected ground structure for wireless power transfer applications," in *2018 Asia-Pacific Microwave Conference (APMC)*, pp. 1435–1437, Nov. 2018.

[53] D. Liu, H. Hu, and S. V. Georgakopoulos, "Misalignment sensitivity of strongly coupled wireless power transfer systems," *IEEE Transactions on Power Electronics*, vol. 32, pp. 5509–5519, Jul. 2017.

[54] J. Lee, Y.-S. Lim, W.-J. Yang, and S.-O. Lim, "Wireless power transfer system adaptive to change in coil separation," *IEEE Transactions on Antennas and Propagation*, vol. 62, pp. 889–897, Feb. 2014.

[55] S. Raju, R. Wu, M. Chan, and C. P. Yue, "Modeling of mutual coupling between planar inductors in wireless power applications," *IEEE Transactions on Power Electronics*, vol. 29, pp. 481–490, Jan. 2014.

[56] F. Mastri, A. Costanzo, and M. Mongiardo, "Coupling-independent wireless power transfer," *IEEE Microwave and Wireless Components Letters*, vol. 26, pp. 222–224, Mar. 2016.

[57] D. Ahn and P. P. Mercier, "Wireless power transfer with concurrent 200-khz and 6.78-mhz operation in a single-transmitter device," *IEEE Transactions on Power Electronics*, vol. 31, pp. 5018–5029, Jul. 2016.

[58] M. Ghovanloo and S. Atluri, "A wide-band power-efficient inductive wireless link for implantable microelectronic devices using multiple carriers," *IEEE Transactions on Circuits and Systems I: Regular Papers*, vol. 54, pp. 2211–2221, Oct. 2007.

[59] L. Li, K. Ma, and S. Mou, "Modeling of new spiral inductor based on substrate integrated suspended line technology," *IEEE Transactions on Microwave Theory and Techniques*, vol. 65, pp. 2672–2680, May 2017.

[60] J. Lim, B. Lee, and M. Ghovanloo, "Optimal design of a resonance-based voltage boosting rectifier for wireless power transmission," *IEEE Transactions on Industrial Electronics*, vol. 65, pp. 1645–1654, Feb. 2018.

[61] A. K. RamRakhyani and G. Lazzi, "On the design of efficient multi-coil telemetry system for biomedical implants," *IEEE Transactions on Biomedical Circuits and Systems*, vol. 7, pp. 11–23, Feb. 2013.

[62] D. Ahn and M. Ghovanloo, "Optimal design of wireless power transmission links for millimeter-sized biomedical implants," *IEEE Transactions on Biomedical Circuits and Systems*, vol. 10, pp. 125–137, Feb. 2016.

[63] T. Imura and Y. Hori, "Maximizing air gap and efficiency of magnetic resonant coupling for wireless power transfer using equivalent circuit and neumann formula," *IEEE Transactions on Industrial Electronics*, vol. 58, pp. 4746–4752, Oct. 2011.

[64] R. Das, A. Basir, and H. Yoo, "A metamaterial-coupled wireless power transfer system based on cubic high-dielectric resonators," *IEEE Transactions on Industrial Electronics*, vol. 66, pp. 7397–7406, Nov. 2019.

[65] R. Chai and A. Mortazawi, "A position-insensitive wireless power transfer system employing coupled nonlinear resonators," *IEEE Transactions on Microwave Theory and Techniques*, vol. 69, pp. 1752–1759, Mar. 2021.

[66] X. Lou and G.-M. Yang, "A dual linearly polarized rectenna using defected ground structure for wireless power transmission," *IEEE Microwave and Wireless Components Letters*, vol. 28, pp. 828–830, Sep. 2018.

[67] K. Dautov, M. Hashmi, and G. Nauryzbayev, "Novel approach improving quality factor of miniature slotted resonators in near-field wpts," in *2022 IEEE International Symposium on Antennas and Propagation and USNC-URSI Radio Science Meeting (AP-S/URSI)*, pp. 1742–1743, Jul. 2022.

[68] Z. Kudaibergenova, K. Dautov, G. Nauryzbayev, M. Hashmi, and M. A. Chaudhary, "Slot-dependent wireless power transfer system for mban applications," in *2020 IEEE 10th International Conference on Consumer Electronics (ICCE-Berlin)*, pp. 1–4, Nov. 2020.

[69] Z. Kudaibergenova, K. Dautov, M. Hashmi, and M. A. Chaudhary, "Utilization of meander line slots for enhancing the wpt efficiency and transmission range," in *2021 IEEE Asia-Pacific Microwave Conference (APMC)*, pp. 452–454, Dec. 2021.

[70] S. Alshhawy, A. Barakat, K. Yoshitomi, and R. K. Pokharel, "Compact and efficient wpt system to embedded receiver in biological tissues using cooperative dgs resonators," *IEEE Transactions on Circuits and Systems II: Express Briefs*, vol. 69, pp. 869–873, Mar. 2022.

[71] S. Verma, D. Rano, and M. Hashmi, "Enhancing the performance of defected ground structure type near-field radiofrequency wpt system by coupled-line impedance matching," *IET Microwaves, Antennas & Propagation*, vol. 14, pp. 1431–1439, Jul. 2020.

[72] K. Dautov, G. Nauryzbayev, and M. Hashmi, "Wireless information and power transfer systems in biomedicine: A new perspective on high-speed applications,"

in *2022 IEEE International Symposium on Antennas and Propagation and USNC-URSI Radio Science Meeting (AP-S/URSI)*, pp. 1334–1335, Jul. 2022.

[73] D. Kupreyev, K. Dautov, M. Hashmi, and S. Verma, "Design of a compact dgs based dual-band rf wpt system for low-power applications," in *2019 8th Asia-Pacific Conference on Antennas and Propagation (APCAP)*, pp. 48–49, Aug. 2019.

[74] A. Barakat, K. Yoshitomi, and R. K. Pokharel, "Design and implementation of dual-mode inductors for dual-band wireless power transfer systems," *IEEE Transactions on Circuits and Systems II: Express Briefs*, vol. 66, pp. 1287–1291, Nov. 2019.

[75] X. Jiang, F. Tahar, T. Miyamoto, A. Barakat, K. Yoshitomi, and R. K. Pokharel, "Efficient and compact dual-band wireless power transfer system through biological tissues using dual-reference dgs resonators," in *2021 IEEE MTT-S International Microwave Symposium (IMS)*, pp. 54–57, Jun. 2021.

[76] F. Ferreira, G. Bulla, and I. Müller, "Compact dual-band system for near-field wireless power transfer using defected ground structures for practical ism bands," in *2021 5th International Symposium on Instrumentation Systems, Circuits and Transducers (INSCIT)*, pp. 1–6, Aug. 2021.

[77] F. Goodarzy, E. S. Skafidas, and S. Gambini, "Feasibility of energy-autonomous wireless microsensors for biomedical applications: Powering and communication," *IEEE Reviews in Biomedical Engineering*, vol. 8, pp. 17–29, Aug. 2015.

[78] "Ieee standard for safety levels with respect to human exposure to radio frequency electromagnetic fields, 3 khz to 300 ghz amendment 1: Specifies ceiling limits for induced and contact current, clarifies distinctions between localized exposure and spatial peak power density," *IEEE Std C95.1a-2010 (Amendment to IEEE Std C95.1-2005)*, pp. 1–9, Mar. 2010.

[79] Q. Wang, W. Che, M. Mongiardo, and G. Monti, "Wireless power transfer system with high misalignment tolerance for bio-medical implants," *IEEE Transactions on Circuits and Systems II: Express Briefs*, vol. 67, pp. 3023–3027, Dec. 2020.

[80] A. Basir and H. Yoo, "Efficient wireless power transfer system with a miniaturized quad-band implantable antenna for deep-body multitasking implants," *IEEE Transactions on Microwave Theory and Techniques*, vol. 68, pp. 1943–1953, May 2020.

[81] K. Zhang, C. Liu, Z. H. Jiang, Y. Zhang, X. Liu, H. Guo, and X. Yang, "Near-field wireless power transfer to deep-tissue implants for biomedical applications," *IEEE Transactions on Antennas and Propagation*, vol. 68, pp. 1098–1106, Feb. 2020.

[82] O. Jonah and S. V. Georgakopoulos, "Wireless power transfer in concrete via strongly coupled magnetic resonance," *IEEE Transactions on Antennas and Propagation*, vol. 61, pp. 1378–1384, Mar. 2013.

[83] O. Abdelatty, X. Wang, and A. Mortazawi, "Position-insensitive wireless power transfer based on nonlinear resonant circuits," *IEEE Transactions on Microwave Theory and Techniques*, vol. 67, pp. 3844–3855, Mar. 2019.

[84] F. Lu, H. Zhang, H. Hofmann, and C. C. Mi, "An inductive and capacitive combined wireless power transfer system with lc-compensated topology," *IEEE Transactions on Power Electronics*, vol. 31, pp. 8471–8482, Jan. 2016.

[85] A. Costanzo, M. Dionigi, F. Mastri, M. Mongiardo, G. Monti, J. A. Russer, P. Russer, and L. Tarricone, "Conditions for a load-independent operating regime in resonant inductive wpt," *IEEE Transactions on Microwave Theory and Techniques*, vol. 65, pp. 1066–1076, Mar. 2017.

[86] A. L. F. Stein, P. A. Kyaw, and C. R. Sullivan, "Wireless power transfer utilizing a high-q self-resonant structure," *IEEE Transactions on Power Electronics*, vol. 34, pp. 6722–6735, Jul. 2019.

[87] K. Lee, C. Jeong, and S. H. Chae, "Analysis of factors effecting on optimal configuration of two receivers for a three-coil wireless power transfer system," *IEEE Systems Journal*, vol. 13, pp. 1328–1331, Aug. 2019.

[88] J.-S. Lim, Y.-T. Lee, C.-S. Kim, D. Ahn, and S. Nam, "A vertically periodic defected ground structure and its application in reducing the size of microwave circuits," *IEEE Microwave and Wireless Components Letters*, vol. 12, pp. 479–481, Dec. 2002.

[89] S. Y. Huang and Y. H. Lee, "A compact e-shaped patterned ground structure and its applications to tunable bandstop resonator," *IEEE Transactions on Microwave Theory and Techniques*, vol. 57, pp. 657–666, Mar. 2009.

[90] C.-S. Kim, J.-S. Park, D. Ahn, and J.-B. Lim, "A novel 1-d periodic defected ground structure for planar circuits," *IEEE Microwave and Guided Wave Letters*, vol. 10, pp. 131–133, Apr. 2000.

[91] D. Ahn, J.-S. Park, C.-S. Kim, J. Kim, Y. Qian, and T. Itoh, "A design of the low-pass filter using the novel microstrip defected ground structure," *IEEE Transactions on Microwave Theory and Techniques*, vol. 49, pp. 86–93, Jan. 2001.

[92] M. Mandal and S. Sanyal, "A novel defected ground structure for planar circuits," *IEEE Microwave and Wireless Components Letters*, vol. 16, pp. 93–95, Feb. 2006.

[93] A. Abdel-Rahman, A. Verma, A. Boutejdar, and A. Omar, "Compact stub type microstrip bandpass filter using defected ground plane," *IEEE Microwave and Wireless Components Letters*, vol. 14, pp. 136–138, Apr. 2004.

[94] H.-W. Liu, Z.-F. Li, X.-W. Sun, and J.-F. Mao, "An improved 1d periodic defected ground structure for microstrip line," *IEEE Microwave and Wireless Components Letters*, vol. 14, pp. 180–182, Apr. 2004.

[95] D.-J. Woo, T.-K. Lee, J.-W. Lee, C.-S. Pyo, and W.-K. Choi, "Novel u-slot and v-slot dgss for bandstop filter with improved q factor," *IEEE Transactions on Microwave Theory and Techniques*, vol. 54, pp. 2840–2847, Jun. 2006.

[96] Z. L. H. Liu and X. Sun, "Compact defected ground structure in microstrip technology," *Electronics Letters*, vol. 41, pp. 132–134, Feb. 2005.

[97] X.-H. Wang, B.-Z. Wang, H. Zhang, and K. J. Chen, "A tunable bandstop resonator based on a compact slotted ground structure," *IEEE Transactions on Microwave Theory and Techniques*, vol. 55, pp. 1912–1918, Sep. 2007.

[98] C. Kumar and D. Guha, "Asymmetric geometry of defected ground structure for rectangular microstrip: A new approach to reduce its cross-polarized fields," *IEEE Transactions on Antennas and Propagation*, vol. 64, pp. 2503–2506, Jun. 2016.

[99] F.-R. Yang, K.-P. Ma, Y. Qian, and T. Itoh, "A uniplanar compact photonic-bandgap (uc-pbg) structure and its applications for microwave circuit," *IEEE Transactions on Microwave Theory and Techniques*, vol. 47, pp. 1509–1514, Aug. 1999.

[100] Y. Han, Z. Liu, C. Zhang, C. Mei, Q. Chen, K. Hu, and S. Yuan, "A flexible microstrip low-pass filter design using asymmetric pi-shaped dgs," *IEEE Access*, vol. 7, pp. 49999–50006, Apr. 2019.

[101] N. Ha-Van and C. Seo, "Modeling and experimental validation of a butterfly-shaped wireless power transfer in biomedical implants," *IEEE Access*, vol. 7, pp. 107225–107233, Aug. 2019.

[102] C.-L. Yang, C.-K. Chang, S.-Y. Lee, S.-J. Chang, and L.-Y. Chiou, "Efficient four-coil wireless power transfer for deep brain stimulation," *IEEE Transactions on Microwave Theory and Techniques*, vol. 65, pp. 2496–2507, Apr. 2017.

[103] M. R. Yuce, H. C. Keong, and M. S. Chae, "Wideband communication for implantable and wearable systems," *IEEE Transactions on Microwave Theory and Techniques*, vol. 57, pp. 2597–2604, Sep. 2009.

[104] G.-P. Gao, C. Yang, B. Hu, R.-F. Zhang, and S.-F. Wang, "A wearable pifa with an all-textile metasurface for 5 ghz wban applications," *IEEE Antennas and Wireless Propagation Letters*, vol. 18, pp. 288–292, Dec. 2019.

[105] K. Zhang, G. A. E. Vandenbosch, and S. Yan, "A novel design approach for compact wearable antennas based on metasurfaces," *IEEE Transactions on Biomedical Circuits and Systems*, vol. 14, pp. 918–927, Jul. 2020.

[106] L. Wang, F. Hu, Z. Ling, and B. Wang, "Wireless information and power transfer to maximize information throughput in wban," *IEEE Internet of Things Journal*, vol. 4, pp. 1663–1670, Aug. 2017.

[107] T. Cui, M. Qi, and X. Wan, "Coding metamaterials, digital metamaterials and programmable metamaterials," *Light Sci Appl*, vol. 3, pp. 1–9, Oct. 2014.

[108] Y.-L. Sun, X.-G. Zhang, Q. Yu, W.-X. Jiang, and T.-J. Cui, "Infrared-controlled programmable metasurface," *Science Bulletin*, vol. 65, pp. 883–888, Jun. 2020.

[109] A. Khaleghi, A. Hasanvand, and I. Balasingham, "Radio frequency backscatter communication for high data rate deep implants," *IEEE Transactions on Microwave Theory and Techniques*, vol. 67, pp. 1093–1106, Dec. 2019.

[110] A. Sabban, "Compact wearable meta materials antennas for energy harvesting systems, medical and iot systems," *Electronics*, vol. 8, Oct. 2019.

[111] A. Arteaga, S. Céspedes, and C. Azurdia-Meza, "Vehicular communications over tv white spaces in the presence of secondary users," *IEEE Access*, vol. 7, pp. 53496–53508, Apr. 2019.

[112] W. J., "Carrier aggregation explained.." https://www.3gpp.org/technologies/keywordsacronyms carrier-aggregation-explained.

[113] J. Shi, X. Fang, E. T. F. Rogers, E. Plum, K. F. MacDonald, and N. I. Zheludev, "Coherent control of snell's law at metasurfaces," *Opt. Express*, vol. 22, pp. 21051–21060, Aug. 2014.

[114] G. Nauryzbayev, K. M. Rabie, M. Abdallah, and B. Adebisi, "On the performance analysis of wpt-based dual-hop af relaying networks in α - μ fading," *IEEE Access*, vol. 6, pp. 37138–37149, Jun. 2018.

[115] G. Nauryzbayev, M. Abdallah, and N. Al-Dhahir, "Outage analysis of cognitive electric vehicular networks over mixed rf/vlc channels," *IEEE Transactions on Cognitive Communications and Networking*, vol. 6, pp. 1096–1107, Apr. 2020.

[116] S. Jayalath and A. Khan, "Design, challenges, and trends of inductive power transfer couplers for electric vehicles: A review," *IEEE Journal of Emerging and Selected Topics in Power Electronics*, vol. 9, pp. 6196–6218, Dec. 2021.

[117] K. Rabie, B. Adebisi, G. Nauryzbayev, O. S. Badarneh, X. Li, and M.-S. Alouini, "Full-duplex energy-harvesting enabled relay networks in generalized fading channels," *IEEE Wireless Communications Letters*, vol. 8, pp. 384–387, Sep. 2019.

[118] M. J. Karimi, A. Schmid, and C. Dehollain, "Wireless power and data transmission for implanted devices via inductive links: A systematic review," *IEEE Sensors Journal*, vol. 21, pp. 7145–7161, Jan. 2021.

[119] G. Monti, F. Mastri, M. Mongiardo, L. Corchia, and L. Tarricone, "Load-independent operative regime for an inductive resonant wpt link in parallel configuration," *IEEE Transactions on Microwave Theory and Techniques*, vol. 68, pp. 1809–1818, Jan. 2020.

[120] S. Verma, D. Rano, S. Malhotra, and M. S. Hashmi, "Measurements and characterization of a newly developed novel miniature wipt system," *IEEE Transactions on Instrumentation and Measurement*, vol. 70, pp. 1–11, May. 2021.

[121] M. Added, N. Boulejfen, M. Svanda, F. M. Ghannouchi, and T.-P. Vuong, "High-performance chipless radio-frequency identification tags: Using a slow-wave approach for miniaturized structure," *IEEE Antennas and Propagation Magazine*, vol. 61, pp. 46–54, Jun. 2019.

[122] C.-C. Wang, H.-C. Chiu, and T.-G. Ma, "A slow-wave multilayer synthesized coplanar waveguide and its applications to rat-race coupler and dual-mode filter," *IEEE Transactions on Microwave Theory and Techniques*, vol. 59, pp. 1719–1729, May 2011.

[123] Y. Zhang, J.-Y. Deng, D. Sun, J.-Y. Yin, L.-X. Guo, X.-H. Ma, and Y. Hao, "Slow wave substrate-integrated waveguide with miniaturized dimensions and broadened bandwidth," *IEEE Transactions on Microwave Theory and Techniques*, vol. 69, pp. 3675–3683, Apr. 2021.

[124] D. Tang, C. Han, Z. Deng, H. J. Qian, and X. Luo, "Substrate-integrated defected ground structure for single- and dual-band bandpass filters with wide stopband and low radiation loss," *IEEE Transactions on Microwave Theory and Techniques*, vol. 69, pp. 659–670, Jan. 2021.

[125] Y. Rao, H. J. Qian, B. Yang, R. Gómez-García, and X. Luo, "Dual-band bandpass filter and filtering power divider with ultra-wide upper stopband using hybrid microstrip/dgs dual-resonance cells," *IEEE Access*, vol. 8, pp. 23624–23637, Jan. 2020.

[126] K. Wei, J. Y. Li, L. Wang, R. Xu, and Z. J. Xing, "A new technique to design circularly polarized microstrip antenna by fractal defected ground structure," *IEEE Transactions on Antennas and Propagation*, vol. 65, pp. 3721–3725, May 2017.

[127] T. Sarkar, A. Ghosh, L. L. K. Singh, S. Chattopadhyay, and C.-Y.-D. Sim, "Dgs-integrated air-loaded wideband microstrip antenna for x- and ku-band," *IEEE Antennas and Wireless Propagation Letters*, vol. 19, pp. 114–118, Nov. 2020.

[128] C. Caloz, H. Okabe, T. Iwai, and T. Itoh, "A simple and accurate model for microstrip structures with slotted ground plane," *IEEE Microwave and Wireless Components Letters*, vol. 14, pp. 133–135, Mar. 2004.

[129] S. U. Rehman and M. A. Alkanhal, "System-based modelling and synthesis of defected ground structure resonators and filters," *IET Microwaves, Antennas & Propagation*, vol. 13, pp. 774–781, Mar. 2019.

[130] J.-S. Lim, S.-W. Lee, C.-S. Kim, J.-S. Park, D. Ahn, and S. Nam, "A 4.1 unequal wilkinson power divider," *IEEE Microwave and Wireless Components Letters*, vol. 11, pp. 124–126, Mar. 2001.

[131] D.-J. Woo, T.-K. Lee, and J. W. Lee, "Equivalent circuit model for a simple slot-shaped dgs microstrip line," *IEEE Microwave and Wireless Components Letters*, vol. 23, pp. 447–449, Aug. 2013.

[132] V. Daniele, G. Lombardi, and R. S. Zich, "Radiation and scattering of an arbitrarily flanged dielectric-loaded waveguide," *IEEE Transactions on Antennas and Propagation*, vol. 67, pp. 7569–7584, Oct. 2019.

[133] C. Han, D. Tang, Z. Deng, H. J. Qian, and X. Luo, "Filtering power divider with ultrawide stopband and wideband low radiation loss using substrate integrated defected ground structure," *IEEE Microwave and Wireless Components Letters*, vol. 31, pp. 113–116, Nov. 2021.

[134] W.-S. Chang and C.-Y. Chang, "A high slow-wave factor microstrip structure with simple design formulas and its application to microwave circuit design," *IEEE Transactions on Microwave Theory and Techniques*, vol. 60, pp. 3376–3383, Sep. 2012.

[135] H.-Y. Cho, T.-J. Yeh, S. Liu, and C.-Y. Wu, "High-performance slow-wave transmission lines with optimized slot-type floating shields," *IEEE Transactions on Electron Devices*, vol. 56, pp. 1705–1711, Jul. 2009.

[136] Y. Sung, C. Ahn, and Y.-S. Kim, "Size reduction and harmonic suppression of rat-race hybrid coupler using defected ground structure," *IEEE Microwave and Wireless Components Letters*, vol. 14, pp. 7–9, Jan. 2004.

[137] I.-S. Jeong, B.-I. Jung, D.-S. You, and H.-S. Choi, "Analysis of s-parameters in magnetic resonance wpt using superconducting coils," *IEEE Transactions on Applied Superconductivity*, vol. 26, pp. 1–4, Mar. 2016.

[138] J. Barreto, A.-S. Kaddour, and S. V. Georgakopoulos, "Conformal strongly coupled magnetic resonance systems with extended range," *IEEE Open Journal of Antennas and Propagation*, vol. 1, pp. 264–271, Jun. 2020.

[139] W. Zhou, S. Sandeep, P. Wu, P. Yang, W. Yu, and S. Y. Huang, "A wideband strongly coupled magnetic resonance wireless power transfer system and its circuit analysis," *IEEE Microwave and Wireless Components Letters*, vol. 28, pp. 1152–1154, Nov. 2018.

[140] T.-H. Kim, G.-H. Yun, W. Lee, and J.-G. Yook, "Highly efficient wpt system with negative impedance converter for q-factor improvement," *IEEE Access*, vol. 7, pp. 108750–108760, Aug. 2019.